

CHEMICAL VAPOR DEPOSITION OF THIN FILM
MATERIALS FOR ELECTRONIC AND
MAGNETIC APPLICATIONS

by

NING LI

TONYA M. KLEIN, COMMITTEE CHAIR
ARUNAVA GUPTA
ALAN M. LANE
SUBHADRA GUPTA
MARK L. WEAVER

A DISSERTATION

Submitted in partial fulfillment of the requirements for the
degree of Doctor of Philosophy in the Department
of Chemical and Biological Engineering
in the Graduate School of
The University of Alabama

TUSCALOOSA, ALABAMA

2011

Copyright Ning Li 2011

ALL RIGHTS RESERVED

ABSTRACT

Chemical vapor deposition (CVD) has been employed to pursue high quality thin film growth for four different materials with excellent electronic or magnetic properties for certain device applications. The relationship between CVD processing conditions and various thin film properties has been systematically studied.

Plasma enhanced atomic layer deposition (PEALD) is a special type of CVD technique and can be used for the deposition of very thin (few nanometers) and highly conformal thin films. PEALD of hafnium nitride (HfN) thin film is studied by using tetrakis (dimethylamido) hafnium (IV) (TDMAH) and hydrogen plasma. Prior to thin film deposition, TDMAH adsorption and reaction on hydrogenated Si(100) surface has been investigated by in-situ ATR-FTIR. It has been found that between 100°C and 150°C surface adsorbed TDMAH molecules start to decompose based on the β -hydride elimination mechanism. The decomposition species on the surface has been found hard to desorb at 150°C, which can contaminate the thin film if the purging/pumping time is insufficient. Uniform and moderately conductive HfN_xC_y films are deposited on hydrogen terminated Si(100) and thermally grown SiO_2 (on Si) substrates by PEALD process. The dependence of thin film resistivity on plasma power is found to be related to the change of surface chemical composition. In vacuo XPS depth profile analysis showed the existence of hafnium carbide phase, which to a certain degree can improve the film conductivity.

Direct liquid injection chemical vapor deposition (DLI-CVD) has been utilized for epitaxial growth of nickel ferrite (NiFe_2O_4), lithium ferrite (LiFe_5O_8) and barium titanate

(BaTiO₃) films on various lattice match substrates. For the deposition of nickel ferrite, anhydrous Ni(acac)₂ and Fe(acac)₃ (acac = acetylacetonate) are used as precursor sources dissolved in *N,N*-dimethyl formamide (DMF) for the DLI vaporizer system. Epitaxial nickel ferrite films of stoichiometric composition are obtained in the temperature range of 500-800 °C on both MgO(100) and MgAl₂O₄(100). Film morphology is found to be dependent on the deposition temperature with atomically smooth films being obtained for deposition temperature of 600 and 700 °C. Magnetic measurements reveal an increase in the saturation magnetization for the films with increasing growth temperature, which correlates well with the trend for improved epitaxial growth. Nickel ferrite films deposited on MgAl₂O₄ (100) at 800°C exhibit saturation magnetization very close to the bulk value of 300 emu/cm³. Out-of-plane FMR measurement shows the narrowest FMR line width of ~160 Oe for films deposited at 600°C. For lithium ferrite deposition, anhydrous Li(acac) and Fe(acac)₃ are dissolved in DMF in a molar ratio of 1:5. Epitaxial growth of lithium ferrite films on MgO(100) are observed in the temperature range of 500°C to 800°C. The as grown films show increasing saturation magnetization with increasing deposition temperature due to the improved degree of crystal texture. For barium titanate thin film deposition, Ba(hfa)₂•tetraglyme and Ti(thd)₂(OPr^{*i*})₂ are dissolved in toluene in a molar ratio of 1:1. Epitaxial growth of barium titanate on MgO(100) has been found at the temperature of 750°C. Film with a thickness of ~500 nm has a relatively large roughness of ~20 nm. Small amount of F elements, which exists in Ba-F bonds, has been detected in the thin film by XPS.

DEDICATION

This dissertation is dedicated to everyone who helped me and guided me through the trials and tribulations of creating this manuscript. In particular, my family and close friends who stood by me throughout the time taken to complete this masterpiece.

LIST OF ABBREVIATIONS AND SYMBOLS

$a, b, c,$	Lattice parameters
AFM	Atomic force microscopy
AGM	Alternating gradient magnetometer
ALD	Atomic layer deposition
at%	Atomic percentage
a.u.	Arbitrary units
B	Magnetic induction
BDE	Bond dissociation energy
BTO	Barium titanate (BaTiO_3)
C	Light speed or capacitance
CVD	Chemical vapor deposition
d	Lattice plane spacing
D	Diffusivity
δ	Conductivity or boundary layer
DI	Deionized water
DOE	Design of experiments
DRAM	Dynamic random access memory
E	Energy or electric field
EDX	Energy dispersive X-ray spectroscopy
E_F	Fermi energy

φ	In-plane tilt angle of X-ray diffraction measurement
FET	Field effect transistor
FMR	Ferromagnetic resonance
g	Effective g factor
GPC	Growth per cycle
γ	Geromagnetic ratio
GMR	Giant magnetoresistance
H_C	Coercivity field
h	Planck constant
$[h\ k\ l]$	Miller indices for a direction indexed by h along x axis, k along y axis, and l along z axis
$(h\ k\ l)$	Miller indices for a plane normal to the $[h\ k\ l]$ direction
IC	Integrated circuit
λ	Light wavelength
LFO	Lithium ferrite (LiFe_5O_8)
LPCVD	Low pressure CVD
M	Magnetization
M_S	Saturation magnetization
MBE	Molecular beam epitaxy
MOCVD	Metal organic chemical vapor deposition
MR	Magnetoresistance
MRAM	Magnetic random access memory
μ_B	Bohr magneton

NFO	Nickel ferrite (NiFe_2O_4)
ω	Angular frequency or angle in transverse X-ray diffraction measurement
P	Polarization
PECVD/ALD	Plasma enhanced chemical vapor deposition/atomic layer deposition
PLD	Pulsed laser deposition
ψ	Longitudinal tilting angle in X-ray diffraction measurement
RF	Radio frequency
RMS	Root mean square
σ	Photoelectric cross section
θ	Angle
s, p, d, f	electron subshells
SEM	Scanning electron microscopy
T	Temperature
T_c	Curie temperature
TDMAH	Tetrakis (dimethylamido) hafnium
TEM	Transmission electron microscopy
TMR	Tunneling magnetoresistance
VSM	Vibrating sample magnetometer
UV	Ultraviolet light
XPS	X-ray photoelectron spectroscopy
XRD	X-ray diffraction
XRR	X-ray reflectivity
x, y, z	Cartesian coordination

ACKNOWLEDGMENTS

It is my pleasure to have this opportunity to express my sincere appreciation to everyone who gave me help to my research and life during my Ph. D. period. The most important person is my advisor Dr. Tonya M. Klein, who guided me into the field of chemical vapor deposition of solid thin film materials. From the basic knowledge of vacuum system design and maintenance to theoretical understanding of thin film growth behavior, I have been greatly benefited from her professional guidance and advising. I would like to express deep respects and great thanks for her patient teaching, invaluable support, and kind trust and encouragement in the past 5 years. I would like to thank my co-advisor Dr. Arunava Gupta, who directed me into the world of magnetic/microwave thin film growth and characterization, which greatly improved my understanding of the relationship between thin film processing conditions and thin film physical properties. Under his support, I have the opportunity to access various cutting-edge thin film characterization techniques/equipments. From him, I have learned a lot on the correct research attitude and the efficient way of analyzing and solving problems.

I would like to thank my committee members: Dr. Alan Lane, Dr. Subhadra Gupta and Dr. Mark Weaver, who have greatly helped me on certain sample characterization, experimental equipments and results interpretation. By taking their courses and discussing with them, I have got a lot of inspirations and learnt how to keep a correct track on my research. Their professional experience in both materials science and chemical engineering always help me to figure out the best solutions in my research.

I would also like to express my sincere thanks to Dr. Heath Turner, Dr. Gary Mankey, Dr. Tim Mewes and Dr. Shane Street. Their kind teaching and help on modeling software, vacuum equipment and certain film characterization techniques are essential for my research to run smoothly and efficiently.

I would like to thank all of my lab mates and group members from both Dr. Klein and Dr. Gupta's group: Dr. Jinwen Wang, Dr. Gihan Kwon, Dr. Kejing Li, Shilpa Dubey, Dr. Yu-Hsiang A. Wang, Dr. Dipanjan Mazumdar, Dr. Jianxing Ma, Dr. Ningzhong Bao, Dr. Liming Shen, Dr. Majit Pathak, Xing zhong, Xueyu Zhang, Ziyou Zhou, Cihat Boyraz, Xiaoyan Zhang, and Mehmet Yurtisigi. It's always my pleasure to work with them and share experimental experiences with them. The discussion with them greatly broadened my understanding in materials related knowledge in physics and chemistry.

I would like to thank Mr. John Hawkins from MINT center, Mr. Rich Martens, Mr. Johnny Goodwin and Mr. Robert Holler from the center of Central Analytical Facility. They have helped me on learning film characterization techniques and troubleshooting hardware problems.

Finally, I would like to thank all of my family members, especially my wife, for their continuous love and support.

CONTENTS

ABSTRACT	ii
DEDICATION	iv
LIST OF ABBREVIATIONS AND SYMBOLS	v
ACKNOWLEDGMENTS	viii
LIST OF TABLES	xiv
LIST OF FIGURES	xv
CHAPTER 1. INTRODUCTION	1
1.1 Chemical Vapor Deposition (CVD)	2
1.1.1 Introduction	2
1.1.2 Atomic Layer Deposition (ALD)	6
1.1.3 Direct Liquid Injection Chemical Vapor Deposition (DLICVD)	8
1.2 Thin Film Growth and Characterization	10
1.2.1 Gas Kinetics	10
1.2.2 Thin film growth in a CVD process	12
1.2.3 Thin Film Characterization	17
1.2.3.1 Attenuated Total Reflectance Fourier Transform Infrared Spectroscopy (ATR-FTIR)	18
1.2.3.2 X-ray Photoelectron Spectroscopy (XPS)	21

1.2.3.3 X-ray Diffraction (XRD)	24
1.2.3.4 Atomic Force Microscopy (AFM)	26
1.2.3.5 Ferromagnetic Resonance (FMR)	28
1.3 Thin Film Application in Electronic and Magnetic Devices.....	30
1.3.1 Metal Oxide Field Effect Transistor (MOSFET)	30
1.3.2 Ferrite-Ferroelectric Layered Heterostructures	33
CHAPTER 2. LITERATURE REVIEW	35
2.1 Hafnium Nitride (HfN).....	35
2.1.1 Physical Properties and Potential Applications	35
2.1.2 Review of HfN Thin Film Growth	36
2.2 Spinel ferrite: Nickel Ferrite and Lithium Ferrite	39
2.2.1 Physical Properties and Potential Applications	39
2.2.2 Review of thin film growth methods	41
2.3 Barium Titanate (BaTiO ₃).....	44
2.3.1 Physical Properties and Potential Applications	44
2.3.2 Review of thin film growth methods	45
CHAPTER 3. PLASMA ENHANCED ATOMIC LAYER DEPOSITION OF HAFNIUM NITRIDE FILMS	48
3.1 Introduction	48
3.2 Tetrakis (Dimethylamido) Hafnium (IV) (TDMAH) Adsorption and Reaction on Hydrogenated Si(100) Surface	49

3.2.1 Introduction	49
3.2.2 Experimental Details	50
3.2.3 Results and Discussion	53
3.3 Plasma Enhanced Atomic Layer Deposition of HfN Films	60
3.3.1 Introduction	60
3.3.2 Experimental Details	60
3.3.3 Results and Discussion	64
3.4 Conclusion.....	71
CHAPTER 4. DIRECT LIQUID INJECTION CHEMICAL VAPOR DEPOSITION OF FERRIMAGNETIC NICKEL FERRITE AND LITHIUM FERRITE FILMS.....	72
4.1 Introduction	72
4.2 DLI-CVD Growth of NiFe ₂ O ₄ Films	73
4.2.1 Experimental Details	75
4.2.2 Results and Discussion	78
4.2.2.1 Thin Film Growth on MgAl ₂ O ₄ (100) and MgO (100)	78
4.2.2.1.1 Oxygen Effect on Film Morphology	78
4.2.2.1.2 Thin Film Growth Mode	80
4.2.2.1.3 Physical properties	84
4.2.2.2 Thin Film Growth on MgO(111), STO(100), PMN-PT(100) and PZN-PT(100) .	96
4.3 DLI-CVD Growth of LiFe ₅ O ₈ Films.....	100
4.4 Conclusion.....	104

CHAPTER 5. DIRECT LIQUID INJECTION CHEMICAL VAPOR DEPOSITION OF FERROELECTRIC BARIUM TITANATE FILMS	106
5.1 Introduction	106
5.2 Experimental Details	107
5.3 Results and Discussion	109
5.4 Conclusion.....	113
CHAPTER 6. CONCLUSION AND FUTURE WORK	114
6.1 Conclusion.....	114
6.1.1 PEALD of HfN thin films	114
6.1.2 DLI-CVD of nickel ferrite and lithium ferrite films.....	115
6.1.3 DLI-CVD of barium titanate films	117
6.2 Future work	117
REFERENCES	119
APPENDIX A: LabVIEW PROGRAM FOR PEALD AUTOMATIC PROCESS	128
APPENDIX B: TDMAH MOLECULAR STRUCTUR OPTIMIZATION AND IR FREQUENCY CALCULATION	130

LIST OF TABLES

Table 1. Hafnium amide precursors and their properties.....	38
Table 2. In vacuo XPS results of thin film surface chemical composition at different experimental conditions.....	67
Table 3. Chemical composition change with depth of analysis.....	69
Table 4. Typical processing conditions for DLI CVD of epitaxial NiFe_2O_4 films.....	79
Table 5. Characteristics of nickel ferrite films deposited at different substrate temperatures.....	84
Table 6. Structural and magnetic properties of nickel ferrite films deposited at different temperatures.....	98
Table 7. Typical vaporization and processing conditions for DLI CVD of epitaxial LiFe_5O_8 films.....	106

LIST OF FIGURES

Fig. 1. Schematic of a typical CVD system with a horizontal tube reactor.....	3
Fig. 2. A typical ALD cycle with oxidation reaction.....	7
Fig. 3. Schematic of a typical direct liquid injection vaporization system.....	10
Fig. 4. Schematic of multiple reflection ART-FTIR spectroscopy.....	20
Fig. 5. Schematic of photoelectron generation process.....	21
Fig. 6. Geometric derivation of Bragg's law.....	24
Fig. 7. Schematic of X-ray diffractometer for thin film crystal structure analysis.....	25
Fig. 8. Main components of atomic force microscopy system.....	27
Fig. 9. Magnetic dipole moment precessing about a static magnetic field.....	28
Fig. 10. Schematic of a n-channel MOSFET.....	31
Fig. 11. ME coupling in a ferrite-ferroelectric layered structure.....	34
Fig. 12. Unit cell of HfN crystal with cubic structure.....	35
Fig. 13. (a) I_d - V_g and (b) I_d - V_d characteristics of an n-MOSFET using HfN-HfO ₂ gate stack with EOT 1.18 nm.....	36
Fig. 14. A cross sectional scanning electron micrograph of uniform Hf ₃ N ₄ thin film coating by ALD on a high aspect ratio trench structure (0.17 μ m \times 0.3 μ m \times 7.3 μ m).....	38
Fig. 15. Representation of a spinel structure.....	39
Fig. 16. Temperature dependence of FMR line width of bulk lithium ferrite single crystal in ordered phase (FMR measurement at two frequencies: 12.3 and 19.41 GHz).....	41
Fig. 17. FMR measurement (9.07 GHz, perpendicular) of lithium ferrite film grown by LPE method on Mg(In,Ga) ₂ O ₄ (111) substrate. Presence of inhomogeneity in the film is	

indicated by the complex FMR curve.....	42
Fig. 18. Schematic of a previously reported DLI-CVD system for nickel ferrite growth.....	43
Fig. 19. Unit cell of perovskite BaTiO ₃ crystal.....	45
Fig. 20. Schematic of a β-diketonate precursor. R' and R'' represent the same or different alkyl groups.....	46
Fig. 21. Molecular structure of TDMAH.....	49
Fig. 22. Experimental setup of the in-situ ATR-FTIR.....	50
Fig. 23. Experimental and theoretical modeled IR spectrum of TDMAH.....	54
Fig. 24. IR spectra of TDMAH adsorption on hydrogenated Si(100) at different Ts.....	54
Fig. 25. Integrated C-H stretching area change with TDMAH (a) adsorption and (b) desorption time at different substrate temperatures.....	56
Fig. 26. Change of ratio of peak 2770 cm ⁻¹ to the whole C-H stretching area in the period of adsorption and desorption at different substrate temperatures.....	58
Fig. 27. Surface Si-H bonds change with TDMAH adsorption and desorption at different crystal temperatures.....	59
Fig. 28. Surface OH group showing up in the desorption/pumping process (150°C).....	59
Fig. 29. Schematic of the plasma enhanced atomic layer deposition system.....	61
Fig. 30. ALD/CVD thin film deposition cluster coupled with in vacuo XPS.....	61
Fig. 31. LabVIEW program for the control of PEALD process.....	63
Fig. 32. Synchronized reactants and plasma pulsing sequence in PEALD experiments.....	63
Fig. 33. The effect of purging time on oxygen incorporation.....	65
Fig. 34. XPS depth profile analysis of (a) Hf4f (b) N1s and (c) C1s in an as deposited HfN _x C _y thin film. Sample prepared at 250°C, 0.15 torr, 100W.....	66
Fig. 35. (a)Cross sectional view of HfN _x C _y on SiO ₂ /Si (b)HRTEM images of HfN _x C _y -SiO ₂ and SiO ₂ -Si interfaces (c) surface topography by AFM, RMS roughness is 0.8nm.....	69
Fig. 36. X-ray reflectivity measurement of the as-deposited HfN _x C _y films at different plasma powers. The number of cycles are 200, 200, and 300 for 50, 100, and 150W, respectively..	69

Fig. 37. (a) Plasma power effect on thin film growth rate and resistivity (b) Plasma power effect on chemical states of surface Hf.....	70
Fig. 38. Experimental set-up of DLI-CVD system for the growth of nickel ferrite films.....	75
Fig. 39. The effect of oxygen flow rate on thin film surface morphology observed using field emission scanning electron microscopy. (a) Without oxygen flow, film of porous structure is formed; (b) particulates formation under high oxygen flow rate.....	78
Fig. 40. Cross-sectional view by field emission scanning electron microscopy; (a) nickel ferrite on MgAl ₂ O ₄ (100) deposited at 500~800°C; (b) nickel ferrite on MgO(100) deposited at 500~800°C; (c) Magnified view of nickel ferrite on MgAl ₂ O ₄ deposited at 600°C, the 5 × 5 μm ² AFM image shows the film surface RMS roughness of ~0.3 nm; (d) Magnified and tilted (10°) view of nickel ferrite on MgO(100) deposited at 500°C with RMS roughness of ~30 nm.....	84
Fig. 41. XRD patterns for NiFe ₂ O ₄ films deposited on MgAl ₂ O ₄ (100) at 500, 600, 700 and 800°C. Peaks with (*) symbol are from MgAl ₂ O ₄ (h00).....	86
Fig. 42. (a) Rocking curves of NiFe ₂ O ₄ (400) diffraction from films deposited at different temperatures. The FWHM are 0.47, 0.46, 0.36 and 0.23 for the 500, 600, 700 and 800°C deposited samples, respectively. (b) φ scan for the {220} diffractions of both NiFe ₂ O ₄ film and MgAl ₂ O ₄ (100) substrate (deposited at 600°C).....	86
Fig. 43. Polarized Raman spectra of NiFe ₂ O ₄ single crystal and NiFe ₂ O ₄ films on MgAl ₂ O ₄ substrate obtained at room temperature with 633 nm excitation with various exact scattering configurations.....	87
Fig. 44. Electron diffraction pattern of nickel ferrite film grown on MgAl ₂ O ₄ substrate at 600°C. (a) diffraction pattern from the nickel ferrite film only; (b) diffraction pattern from both the film and the substrate.....	88
Fig. 45. Bright field TEM image of nickel ferrite on MgAl ₂ O ₄ deposited under 600°C. The image is taken under two beam conditions with $g = \langle -1-10 \rangle$	89
Fig. 46. (a) HRTEM image of the interface between nickel ferrite film and MgAl ₂ O ₄ substrate; (b) Fourier transform of the area in the red box of the HRTEM image, the as left lattice fringes are from {040} planes.....	89
Fig. 47. AGM hysteresis loops for nickel ferrite films deposited at 500°C and 800°C. The upper-left inset shows the dependence of the saturation magnetization on deposition temperature; the lower-right inset shows the dependence of the coercivity on deposition temperature.....	91
Fig. 48. FMR resonance field under different microwave frequencies and crystal orientations as measured for the nickel ferrite sample deposited at 600°C. (5 mm × 5 mm, ~780 nm).....	92

Fig. 49. Ferromagnetic resonance curve of nickel ferrite films deposited on MgAl ₂ O ₄ substrate at different growth temperatures. (Sample size 5 × 5 mm, thickness 650~780 nm) The inset shows the profile of FMR line width with thin film growth temperature.....	94
Fig. 50. In plane FMR curves measured at different angles of the sample to the static magnetic field. The inset shows the line width value vs. in plane angle.....	95
Fig. 51. In-plane and out-of-plane FMR of nickel ferrite film deposited on MgAl ₂ O ₄ at 600° ..	96
Fig. 52. XRD θ -2 θ scan of nickel ferrite films grown on MgO(111) at different Ts.....	97
Fig. 53. ϕ -scan of nickel ferrite film grown on MgO(111) at 700°C. {400} and {200} planes from the film and substrate were scanned respectively.....	98
Fig. 54. Atomic force microscopy images of nickel ferrite films grown on MgO(111) substrate at different temperatures. All the images were scanned in a range of 5 μ m by 5 μ m. The RMS roughness for films deposited at 500°C, 600°C, 700°C and 800°C are 27 nm, 89 nm, 2.7 nm and 3.5 nm respectively.....	98
Fig. 55. Epitaxial growth of nickel ferrite films on SrTiO ₃ (100), PMN-PT (100) and PZN-PT(100) substrates at 600°C measured by XRD θ -2 θ scan. Peaks with * are from (<i>h</i> 00) reflections of the underlying substrates.....	99
Fig. 56. X-ray diffraction θ -2 θ characterization of lithium ferrite films deposited on (a) MgO (100) and (b) MgAl ₂ O ₄ (100) substrate at different temperatures.....	102
Fig. 57. In plane FMR measurement of lithium ferrite film grown on MgO(100) substrate at 600°C. (The microwave frequency is 9.5 GHz, the sample size is 5 mm by 5mm and film thickness is ~550 nm).....	103
Fig. 58. X-ray diffraction characterization of as deposited nickel ferrite film under 750 °C. (a) θ -2 θ scan of as deposited BTO film on MgO(100) (b) ω -scan of BTO(200) (c) ϕ -scan of {101} and {202} planes of film and substrate respectively.....	110
Fig. 59. (a) Cross sectional and (b) Surface view of BaTiO ₃ film on MgO; inlet shows the 10 by 10 μ m AFM image with RMS ~20 nm.....	111
Fig. 60. Fluorine peak is present in the XPS spectrum of as deposited barium titanate film	112
Fig. 61. LabVIEW block diagram for PC control of automatic PEALD process.....	129
Fig. 62. 3D view of TDMAH molecular structure optimized by DFT method.....	131

CHAPTER 1. INTRODUCTION

Thin films of electronic and magnetic materials have been applied in various high technology devices and are continuing to be developed for use in next generation technologies. Microelectronics, data storage, photovoltaics, and microwave devices are few examples where electronic and magnetic thin films can play a key role. By using these thin film materials, not only can the volume of devices be minimized but also some desirable properties can manifest, which are unobtainable in bulk materials. For most practical applications, electronic and/or magnetic thin films are coupled into multilayer structures, whose interfaces can generate unprecedented phenomena and behave as completely new and engineered materials. Metal oxide semiconductor field effect transistor (MOSFET),[1] giant magneto-resistance (GMR),[2] tunneling magneto-resistance (TMR) [3] and magneto electric effect (ME),[4] all of which exist in multilayer thin film structures, have been widely investigated and are still attracting lots of research attention. To realize the as-expected physical characteristics in devices mentioned above, the thin film deposition process is apparently a very important step. Different techniques have been developed in the past, including vapor phase methods such as RF/DC magnetron sputtering, pulsed laser deposition, thermal/E-beam evaporation, molecular beam epitaxy, and chemical vapor deposition as well as liquid phase methods such as painting, spin-spray plating, chemical bath deposition, and liquid phase epitaxy. Compared to the latter methods, vapor phase methods have much wider processing window for substrate material type and deposition temperature and can generate thin films with better quality. Among the vapor phase methods, Chemical vapor deposition has several advantages over others, such as large area deposition, relatively high

growth rate, good step coverage and better control of stoichiometry. In this dissertation work, chemical vapor deposition of thin films of hafnium nitride (HfN), Nickel ferrite (NiFe_2O_4), Lithium ferrite (LiFe_5O_8) and Barium titanate (BaTiO_3) are investigated.

As a chapter of introduction, the chemical vapor deposition technique itself will be demonstrated first from the basic concepts to various applications. Next, thin film growth mechanism with regard to chemical vapor deposition and different thin film characterization methods will be reviewed. At last, the physical principles of electronic/magnetic thin film applications in two specific devices, MOSFET and ME layered heterostructure, will be introduced.

1.1 Chemical Vapor Deposition (CVD)

1.1.1 Introduction

Chemical vapor deposition (CVD), as indicated by the name, is a thin film deposition technique which employs one or more vapor phase chemical reactants to react with and nucleate on the thermal heated solid substrate surface and thus achieving continuous growth of solid film materials. A typical CVD process includes chemical precursor source (gas, liquid or solid), gas transport line, thin film growth chamber with a shower head for uniform dispersion of gas phase chemicals and a thermal heated susceptor where the substrate (wafer) is placed, and the exhaust system usually composed of various vacuum pumps and chemical trapping equipment. A schematic diagram of a simple thermal CVD system as described above is showed in Fig.1 below.

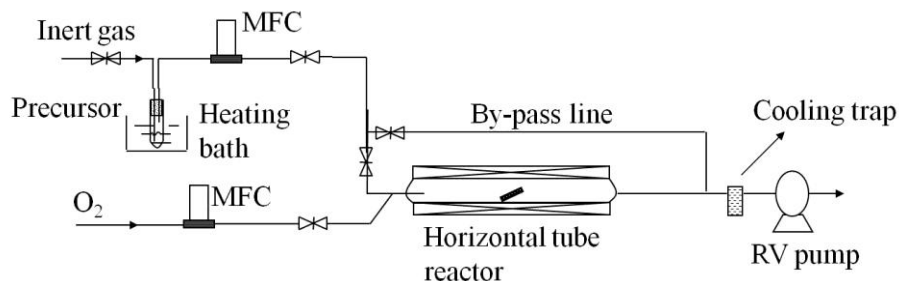


Fig. 1. Schematic of a typical CVD system with a horizontal tube reactor.

The precursor selection is an important factor which can greatly affect the CVD processing conditions and the grown thin film qualities. Generally, few properties have to be considered before selecting an appropriate precursor, such as, volatility, thermal stability and potential impurity formation in the grown films. The chemicals often used as CVD precursors include metal halides, metal alkyls, metal cyclopentadienyls, metal alkoxides and metal β -diketonates, etc.. Metal halides as the simplest inorganic precursors are highly reactive and thermally stable, but their vaporization require high temperatures and they produce corrosive gaseous by-products that etch the film constituents or the reactor walls and pump parts. Metal alkyls have reactive metal carbon bonds and therefore low thermal energy is needed for deposition of like metal oxides. The small alkyl ligands can minimize steric hindrance and generate volatile and relatively inert by-products, which can ameliorate readsorption and corrosion effects. However, the selection of metal alkyls is always limited by the number of available metal elements that exist in this format. The low thermal stability of these precursors is another problem needs to be considered. Metal cyclopentadienyls are usually available for alkaline earth metals. They also have active metal carbon bonds and produce hydrocarbon by products. The potential issue with this kind of precursor is film contamination by carbon and/or hydrogen elements from the precursor decomposition.[5] Metal alkoxides are used only for the

growth of thin film oxides due to the highly strong metal oxygen bond. Generally, low temperature decomposition can generate the desired oxide. Metal β -diketonates also have a strong metal oxygen bond. The oxidant used is usually ozone instead of oxygen or water vapor. A marked issue with these precursors is the effect of steric hindrance, which might leave unoccupied surface sites and decrease the grown film density. Metal alkylamides have relatively high volatility and active metal nitrogen bonds for reaction with oxidants. It has been found in certain chemical vapor deposition research that this kind of precursors would show some 'readsorption' behavior and little information is known about the reaction by-products.[5] All the precursors mentioned above have their own advantages and disadvantages. To make the best selection, all the precursor properties have to be considered comprehensively. As mentioned earlier, the selection of precursor is also dependent on the specific type of CVD technique. The following few paragraphs will introduce the basic classifications.

The CVD technique can be classified into different types due to different standards of classification. For example, based on the operation pressure, it can be divided into low pressure CVD (LPCVD), ultrahigh vacuum CVD (UHVCVD) and atmospheric CVD (APCVD). It's apparent CVD technique can be operated in an environment with a much wider pressure window than PVD methods, which are often operated under ultrahigh vacuum conditions, for example, thermal/e-beam evaporation and molecular beam epitaxy. Usually, the lower the system pressure, the less contamination issues plague thin film growth. However, the decreased pressure is accompanied with a lower film grow rate. Another way of classification of the CVD technique is based on different energy types applied to overcome the activation energy barriers of breaking bonds, such as, thermal CVD, electron beam CVD,[6] laser CVD and plasma enhanced CVD (PECVD). Among these, PECVD has been extensively studied in the past, especially for thin

film growth on thermally sensitive substrates. The reason is that energetic species (electrons, ions and free radicals) generated in a plasma can activate certain decomposition or surface reaction processes at a fairly low substrate temperature. Apart from the classical types of CVD techniques mentioned above, two special types of CVD techniques which are directly related to the research work of this dissertation is introduced below.

A special type of CVD technique is named atomic layer deposition (ALD). The difference of ALD from classic CVD is that the exposure of the substrate surface to different reactive precursors is in a sequential mode and separated from each other by inert gas purging or vacuum pumping. An essential feature for ALD process is the self saturation behavior of surface adsorbing species. In this way, the thin film growth can be controlled with atomic accuracy in terms of thin film thickness and chemical stoichiometry. More details about this technique will be introduced in 1.1.2.

An important historical concern with CVD is the availability of both volatile and thermally stable chemical precursors. The development of novel CVD related precursors itself is always an active area of research for chemists. Another way to conquer this limitation is to develop high efficiency vaporization system, which can generate high quality vapor phase by employing the simple chemicals. Classical CVD technique coupled with a vaporization system is so called direct liquid injection CVD (DLICVD). More information about this technique will be illustrated in 1.1.3.

As a chemical reaction process, CVD can be carried out in different reactor geometries, which might affect the pattern of gas fluid flow and thus induce different effects in thin film growth. The three generic reactor designs are axisymmetric, tube and batch. The axisymmetric

one can uniformly deliver precursor species onto the substrate surface. The tube reactor (Fig.1) has higher processing capacity than the axisymmetric one, but the precursor concentration decreasing (due to decomposition or deposition) as the gas fluid flows downstream might result in different thin film growth rates at different tube lengths. The batch reactor has the highest processing capacity. Since there is usually no bulk convection through the space between wafers, the mass transfer behavior is always in the form of diffusion. For this reactor, the thin film growth has to be reaction rate controlled to get uniform deposition, which means the diffusion rate of gas precursors has to be much faster than the surface reaction rate.[7] It's also noteworthy that temperature uniformity is essential to get uniform thin films in this mode because the reaction rate is exponentially dependent on substrate temperature.

Different types of materials including metals, ceramics and semiconductors and materials with different crystallographic features, such as, polycrystalline, single crystalline and amorphous can be deposited by CVD technique. Apart from the planar thin film growth, CVD has also been extensively studied for the growth of 3D nanostructures (nanowires, nanotubes, etc). CVD has been seen as a standard film growth technique in the semiconductor industry for manufacturing integrated circuits (IC) components for a long time. Due to the mature engineering design of CVD equipment, this technique is also now a prevalent tool in other applications, such as, high speed cutting tools, flat panel displays and photovoltaics.

1.1.2 Atomic Layer Deposition (ALD)

Atomic layer deposition (ALD) as mentioned previously is a chemical vapor deposition technique based on self-terminating gas solid reactions. A typical ALD process consists of repeating deposition cycles and each cycle includes four basic steps. These steps are, in sequence, substrate exposure to gas phase chemical precursor, deposition chamber purging with inert gas or

simply evacuating with vacuum pump, substrate exposure to the gas phase oxidant or reductant chemicals, and the last step of purging the deposition chamber with inert gas. A schematic diagram of steps for a typical ALD cycle is showed in Fig.2.

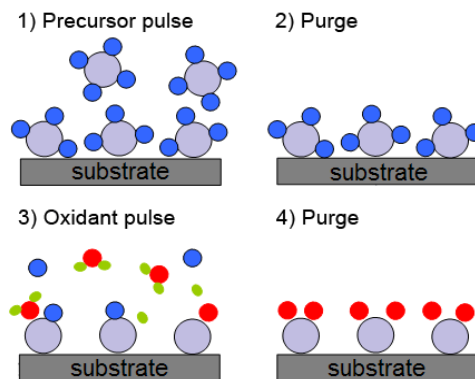


Fig. 2. A typical ALD cycle with oxidation reaction.

As shown in Fig.2, the first step in an ALD repeating cycle is adsorption of a gas phase metal containing precursors onto a substrate surface. To satisfy the criteria of self-terminating adsorption, chemisorption, which has much higher bonding energy to the substrate surface than physisorption, is necessary. For a chemisorption process, usually new chemical bonds between the precursor molecule and substrate surface will form and simultaneously certain volatile reaction products will be generated which will be purged and pumped out of the deposition chamber in the following step. In addition, the thermal stability of the adsorbed species has to be high enough to eliminate surface decomposition or intra reaction of the precursor itself, which will also induce non self-terminating behavior. The next step is purging/evacuating the deposition chamber, which should sweep out most of the residual gas phase and surface physisorbed reactive species generated by the previous step. After purging/evacuating, the risk of gas phase reaction/nucleation by introducing the oxidant/reducer chemicals into the chamber is minimized. Also, the substrate surface is covered uniformly with chemisorbed reactive species

for the next reaction step as shown in Fig.2. It has been found that the surface coverage after this step is usually a fraction of a monolayer, which is due to the effect of steric hindrance of the ligands and thus certain surface reactive sites will not be covered. The third step is to introduce oxidant/reducer chemicals into the deposition chamber to react with the active sites of the previously covered surface. This step is mainly to oxidize or reduce the previously adsorbed surface by substituting the surface organic ligands with new reactive bonds for the reaction with precursor molecules of the next cycle. Usually this new formed surface has the same chemical bonds as the bare substrate surface. The last step is to purge/evacuate the chamber to get rid of the reactive oxidants/reducers and after this step the substrate is ready to start a new cycle of deposition.

ALD has few advantages such as digital thickness control at the atomic level, perfect 3D conformality, large area thickness uniformity, low defect density, possibility of low temperature deposition (RT~400°C), and atomically smooth topography. The main disadvantage of the ALD method is its low growth rate, which is usually less than one atomic layer per cycle. This low growth rate has limited ALD method mainly to very thin layers deposition, such as the gate dielectric layer in the MOSFET structure, which is only 2 or 3 nanometers thickness.[8]

1.1.3 Direct Liquid Injection Chemical Vapor Deposition (DLICVD)

CVD technique coupled with various liquid injection/vaporization equipment is usually defined as direct liquid injection CVD (DLICVD), in which the precursor source is in the state of liquid solution and injected into the vaporization equipment to generate vapor for the CVD reaction. By using DLICVD, all the precursors can be prepared as a single source, i.e. dissolving them (liquid or solid) into an appropriate solvent. After injection into the vaporizer, these precursors can be vaporized simultaneously and therefore the molar ratio between different

precursors would be the same as the corresponding mixing ratio in the solution.[9] Except for this easy control of element composition, the liquid flow rate can be also controlled simply and accurately by employing certain liquid mass flow controllers. Compared to the traditional vaporization techniques, such as bubbler or crucible (for liquid or solid precursors), the mass flux of precursors entering the CVD chamber is much more reproducible. Another advantage is that keeping the liquid source at room temperature can minimize the problem of precursor degradation, which usually happens at elevated temperatures. This method opens up the CVD process to a larger possibility of precursor chemicals and allows for the deposition of materials that are very difficult to deposit by conventional vapor transportation. DLICVD has been successfully applied to the deposition of oxides such as $\text{Ba}(\text{Sr},\text{Ti})\text{O}_3$, $\text{Pb}(\text{ZrTi})\text{O}_3$, ZrO_2 and La_2O_3 . [10]

The main goal of vaporizer design is to realize fast, smooth and gentle vaporization. Usually the liquid precursor is broken into very small droplets (few microns size) first and then thermally heated by certain hot medium. Either an ultrasonic nozzle or pressurized spraying technology can be used to break/atomize the injected liquid, which can greatly increase the liquid surface area and make the vaporization process easier and faster. The thermal heating of the as generated droplets can be from a hot surface or carrier gas. Generally, the carrier gas, as a heating medium, can minimize the thermal decomposition effect. A schematic diagram of a DLI vaporizer using carrier gas as a heating medium is showed in Fig.3 below.

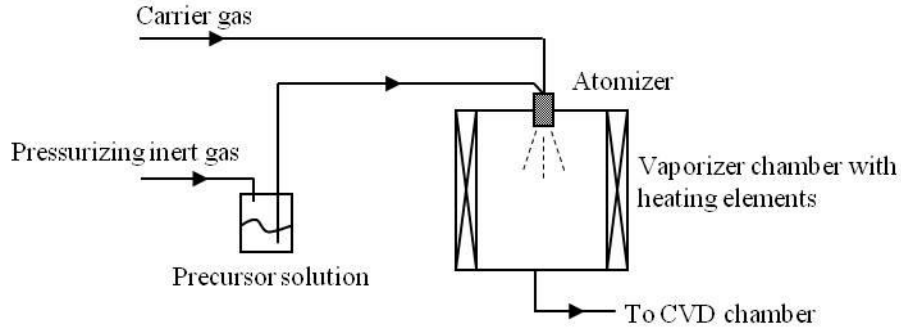


Fig. 3. Schematic of a typical direct liquid injection vaporization system.

1.2 Thin Film Growth and Characterization

Thin film growth by chemical vapor deposition is a very complex process including bulk transportation of gaseous fluid flow, gas phase and surface diffusion, homogeneous and heterogeneous chemical reaction and film material nucleation. The variation of each of these processes can to a certain degree result in the change of thin film growth behavior and properties of the as-grown thin films. The introduction of CVD thin film growth mechanism here will include most of these physical and chemical processes from the gas phase precursor entering the reaction chamber to the solid thin film growth on the substrates.

1.2.1 Gas Kinetics

To understand the gas phase kinetic behavior of the precursor molecules in the CVD chamber, basic concepts of gas kinetics based on statistical mechanics are briefly introduced first. The statistical distribution of velocities of gas phase molecules at thermal equilibrium has been well described by the Maxwell-Boltzmann equation:[11]

$$\frac{dN/dc}{N} = 4\pi c^2 \left(\frac{m}{2\pi k_B T} \right)^{3/2} \exp\left(-\frac{1}{2} \frac{mc^2}{k_B T} \right) \quad (1.1)$$

In this equation, N , c (m/s), m (kg), k_B (J/K), T (K) represent the number of molecules, molecular speed, molecular mass, Boltzmann constant and absolute temperature respectively. By using this equation, we assume that the gas phase temperature is in the range of an ordinary thermal CVD process and thus the main mode of molecular excitation is translational instead of the other three, i.e., rotational, vibrational and electronic. This equilibrium distribution is from the continuous energy exchange due to random collisions between molecules or molecules with the surfaces. An important parameter, mean molecular speed \bar{c} under a fixed temperature, can be derived from this equation, which is essential for the calculation of molecular impingement flux and thus understanding of the thin film deposition rate. The well know Knudsen equation, which employs this mean speed and the ideal gas law (true for all of the CVD processes where T is at or above room temperature and P is at or below atmospheric pressure) for molecular impingement flux calculation is listed below.

$$J_i = 2.63 \times 10^{20} \frac{p}{\sqrt{MT}} \quad (1.2)$$

The molecular impingement flux is in the unit of mc/cm^2s (molecules per square centimeter per second) and p , M , and T are in the units of Pa, g, and K respectively. It's noteworthy that this molecular flux is quite different from the practical thin film deposition flux, which can be calculated from the thin film growth rate and a thin film density. As will be mentioned later, this is because a great fraction of the impingement flux would experience reflection from the substrate surface or even desorption from an adsorbed state of low energy.

An important dimensionless value determining the gas phase flow is the so called Knudsen number (K_n), which is defined as the ratio of the molecular mean free path to the characteristic dimension of the process.[11] Basically, the value of the molecular mean free path

is predominantly dependent on system pressure unless the temperature is extremely high. The characteristic dimension, for example, in a CVD process, can be the tube diameter for a tube reactor. When $K_n > 1$, the process is in high vacuum or molecular flow regime, where the interactions between molecules are greatly minimized/eliminated. Most physical vapor deposition methods are operated in this regime to minimize contamination effects. However, the line-of-sight deposition characteristic makes it difficult to get conformal thin film growth on high aspect ratio 3D structures. When $K_n < 0.01$, the process is in the viscous fluid flow regime and this is also the regime of typical CVD processes.

1.2.2 Thin film growth in a CVD process

In a CVD process, convection is the primary way by which bulk gas flow transfer from the entering shower head to the vicinity of substrate surface. The driving force for this convection, also known as forced convection, is a pressure gradient. A local convection behavior due to the buoyancy of gases close to a hot surface is known as free convection, which can often induce circulating flow patterns and affect the uniformity of as grown thin films. This phenomenon is mainly related to the reactor shape and gas flow pattern and can thus be minimized by adjusting certain geometry or gas flow parameters. Generally, the flow pattern resulting from forced convection can change from laminar flow to turbulent flow and this can be well determined by the dimensionless Reynolds number (Re). Nevertheless, for CVD processes, due to the normal operation conditions, the flow pattern is nearly always in laminar flow mode.[11] For such a flow pattern (laminar) in a horizontal tube CVD reactor, the gas velocity decreases from the tube center to the walls by the force of viscous friction and give rise to a parabolic velocity distribution. However, more complicated velocity profiles can be induced by abrupt changes in flow path or by a steep T gradient. When the bulk gas flow across the

susceptor, the flow pattern can be distorted to a certain degree at the beginning, but shortly it will restore to a balanced laminar flow between the susceptor/substrate and the tube wall. This effect should not affect the thin film growth considering the small influence on the diffusion behavior in the stationary boundary layer right above the substrate surface. In an axisymmetric CVD reactor, the flow pattern is more complicated due to the velocity change in both axial and radial directions when flowing onto the substrate surface. The velocity boundary layer thicknesses are never going to be much smaller than the susceptor radius under any reasonable flow conditions.[7]

After the bulk convection delivers the gaseous precursors to the vicinity of the substrate surface, the convective transport will change to diffusive behavior in a stagnant boundary layer due to a no-slip boundary condition (velocity at the wall is zero) and viscous friction. The mass transfer through this layer is driven by the concentration gradient from the bulk gas phase to the substrate surface where the thin film forming reaction consumes incoming species. The diffusion kinetics is illustrated by Fick's law, which relates the mass diffusion flux to the concentration gradient and a diffusivity constant. This diffusivity constant is dependent on certain gas kinetic parameters introduced earlier, i.e., the mean molecular speed (\bar{c}) and mean free path. Considering the relative kinetics of this diffusion step and the following surface reaction, either of them can be a rate control step for the thin film growth. A simple model for the understanding of the control mode is introduced here. Assuming steady-state CVD thin film growth and negligible desorption/reevaporation, the diffusing species A moving from the bulk gas phase (n_b) to the growing surface (n_0) possesses a diffusivity constant of D and encounters a boundary layer thickness of δ . According to Fick's law, we can obtain

$$J_r = J_A = -D \frac{n_b - n_0}{\delta_n} \quad (1.3)$$

or for the fraction depletion of reactant at the surface,

$$f_0 = \frac{n_b - n_0}{n_b} = \left| \frac{J_r}{D n_b / \delta_n} \right| \quad (1.4)$$

There are two limiting cases, diffusion control and reaction control, which can be derived from Eq.(1.4). That is when f_0 is very small and there is almost no difference of concentration of species A from the bulk gas phase to the substrate surface, the thin film growth is in reaction control mode and the thin film growth rate is dependent on the surface reaction rate only. The other case is when f_0 is approaching 1. In this case, the surface concentration of species A is very low due to the much faster surface reaction rate than the diffusion rate and the thin film growth is in diffusion control mode. The intermediate case is more difficult to analyze and control practically, so it should be avoided in CVD process. Appropriate film growth mode can be selected/controlled to achieve the best film uniformity in different CVD reactors. For example, in the axisymmetric reactor, where the substrate temperature uniformity is difficult to achieve, the thin film growth in diffusion control mode can help get uniform films.[12]

In the processes of both convection and diffusion, a unique phenomenon of CVD is homogeneous reaction. Depending on the thermal stability/reactivity of the precursors and the temperature profile in the reactor, gas phase homogeneous reaction can start from certain points. Excessive gas phase reaction can generate particles on the grown thin film and affect its physical properties. To minimize gas phase interaction, an effective way is to reduce the system pressure and thus increase the molecular mean free path. Elimination of gas phase reaction can be achieved by ALD thin film growth, which separates the injection of different reactants by

purging the reactor with inert gas. In ALD process, the film forming reactions happens only on the substrate surface.[13]

The interaction of impinging gas phase molecules with the substrate surface in thin film deposition is similar to those have been well studied in heterogeneous catalysis. As the impinging molecules get close to the surface (atomic distance), attractive force due to dipole interaction between the molecules and the surface bonds can pull the precursor molecules further onto the surface until a potential well is reached. The as-trapped molecules is in the state of physisorption and has a relatively weak interaction (Van der Waals force) with the surface. The fraction of physisorbed molecules in the impinging flux is defined by the trapping probability, δ . These physisorbed species can either desorb from the surface or move through the surface sites by surface diffusion. Both of these processes need to surpass certain activation barriers and the latter process is usually more favorable. The surface diffusion behavior can help the precursors find each other, find the most active sites, or find epitaxial sites. The physisorbed precursors, after surface diffusion, can go further to react with the active surface sites by forming new bonds and/or release certain volatile by-products. These newly formed bonds constitute the basis for thin film growth. The as-formed surface species is in the state of chemisorption, which has much stronger bonds than the previous physisorption state. The fraction of chemisorbed molecules in the impinging flux is defined as chemisorption reaction probability, ζ . The chemisorbed species can also go back to the physisorption state by surface reversal reaction. Due to the desorption behavior of both physisorption and chemisorption, a more practical parameter called a sticking coefficient is used to denote the fraction of the arriving vapor that remains adsorbed for the duration of the experiment. The degree of these surface processes can vary dramatically due to different surface bonding environments and/or substrate temperatures.[11,14] For example, the

surface passivation with certain inert bonds can greatly increase the activation barrier for chemisorption reaction and thus make thin film deposition difficult.

Nucleation of thin film materials on the substrate surface is driven towards the minimization of total surface energy, i.e., the sum of the surface energy terms from the as formed film surface (γ_f), the interface (γ_i) and the substrate surface (γ_s) should be minimized. When the interfacial bonding is so strong that the resulting small interfacial energy satisfy Eq. (1.5), the as

$$\gamma_f + \gamma_i < \gamma_s \quad (1.5)$$

grown film material will wet the substrate surface to minimize total surface energy and exhibit 2D layer by layer growth, which is also known as Frank-van der Merwe growth. If the interfacial bonding is insufficient to hold Eq. (1.5), the film material will not wet the substrate but instead form 3D islands, which is known as the Volmer-Weber growth mode. The third growth mode is Stranski-Krastanov, for which the growth changes from layer to island after a monolayer or two due to the change in the energy situation with successive monolayer.[11] It's noteworthy that all of the growth modes above are based on the assumption of sufficient surface diffusion. That is to say there has to be reasonable surface diffusion rate to get the thermal equilibrium state. Therefore, it's possible to achieve preferred surface topography by tuning the surface diffusion kinetics, which is dependent on the substrate temperature. For example, by lowering the substrate temperature, the island mode growth can be suppressed because of insufficient surface diffusion to reach the thermodynamic equilibrium and the surface topography can become smoother. When the substrate temperature is too low to have any surface diffusion behavior, the film growth is in 'quenched mode', that is the adsorbing species will stay at where they land. For this case, usually a columnar film structure can be formed and the surface roughness results from

statistical roughening. For epitaxy, one more parameter, lattice mismatch is also important for determining the film growth mode.[15] The lattice mismatch (f) is defined as below,

$$f = (a_f - a_s) / a_s \quad (1.6)$$

where a_f and a_s represent the atomic spacings along some direction in the film and substrate crystal, respectively. When the thermal expansion coefficients of the two materials are different, f becomes a function of T and this will also contribute to the temperature dependence of thin film growth mode or surface topography development.[16,17] For example, at certain high growth temperatures, due to the difference of thermal expansion, the lattice mismatch becomes large enough to induce much larger interfacial energy (γ_i) and thus inequality Eq. (1.5) will fail and the thin film growth will change to 3D island mode.

1.2.3 Thin Film Characterization

Thin film characterization includes in situ monitoring of thin film growth behavior and post deposition measurement of various film properties. The in situ monitoring of thin film growth can provide continuous updated information such as chemical composition, crystal structure, surface topography, film thickness, and optical properties, etc.. For instance, reflection high energy electron diffraction (RHEED) can be used to detect surface crystallographic information in epitaxy. The RHEED pattern is an instantaneous reflection of the arrangement of atoms on a thin film surface.[18] Other in situ monitoring tools, such as attenuated total reflectance Fourier transform infrared spectroscopy (ATR-FTIR), ellipsometry, quartz crystal microbalance (QCM) are also widely used. Post deposition measurement has a much wider window of option of analysis techniques. For example, for the chemical composition analysis, X-ray photoelectron spectroscopy (XPS), Auger electron spectroscopy (AES), Energy dispersive X-

ray spectroscopy (EDS), Wavelength dispersive X-ray spectroscopy (WDS), Rutherford backscattering spectrometry (RBS) can all serve for this purpose. All of these techniques are nondestructive and can provide both qualitative and quantitative chemical information. For these techniques, irradiation of the sample with X-ray, electron beam or ion beams are needed to generate the characteristic signals of each element in the thin film for detection. To differentiate these techniques, XPS and AES are much more surface sensitive than the others and can give better quantitative results for small elements such as C, N and O. EDS, WDS, and RBS have much larger detection depth and usually used for thick films or bulk material analysis. A common limitation of these techniques is that they cannot detect the smallest elements such as H, He and/or Li, which might be an important information for certain practical applications. Secondary ion mass spectrometry (SIMS), another chemical composition analysis technique, instead can detect all the elements from H to U and it possesses the highest detection limit compared to other techniques. However, these advantages is compromised by the character of destructive analysis. Other thin film properties, such as crystal structures can be characterized by diffraction techniques employing X-ray, electron or neutron beam, surface morphology can be characterized by Atomic force microscopy (AFM) or Scanning tunneling microscopy (STM) and magnetic properties can be characterized by Vibrating sample magnetometer (VSM), Alternating gradient magnetometer (AGM) and Ferromagnetic resonance (FMR). Few representative techniques, including both in situ monitoring and post deposition characterization, which are directly related to this dissertation research will be briefly introduced below.

1.2.3.1 Attenuated Total Reflectance Fourier Transform Infrared Spectroscopy (ATR-FTIR)

Infrared (IR) spectroscopy has been long known as an important tool for analytical chemistry due to its ability to detect chemical bonds and groups in both organic and inorganic

samples. The IR absorption behavior is related to the various mechanical vibrational modes in molecules. A classical vibrational frequency formula for a diatomic molecule containing two atoms with mass m_1 and m_2 is illustrated as Eq.(1.7). In this equation, ν and F represent the vibrational frequency and the force constant respectively. The number of vibration modes in a

$$\nu = \frac{1}{2\pi} \sqrt{F \left(\frac{1}{m_1} + \frac{1}{m_2} \right)} \quad (1.7)$$

molecular system with N atoms is determined by the number of internal degree of freedom, which means for linear molecules the number of vibration modes is $3N-5$ and for nonlinear molecules the number is $3N-6$. [19] Among these vibration modes, usually some of them might be not IR active and this is determined by the IR selection rule. This rule is that the electric dipole moment of the molecule must change during vibration in order for a particular vibration mode to be detected by IR absorption. For example, the 1388 cm^{-1} symmetric stretch mode for carbon dioxide gas cannot be detected by IR spectroscopy, while the 2349 cm^{-1} asymmetric stretch mode is IR active. A special phenomenon for IR spectroscopy worth to be remembered is that if a vibration mode of frequency ν is detected then its overtones 2ν , 3ν might also be detected by IR absorption. [20]

ATR-FTIR is the conjunction of ATR sampling technique into the traditional FTIR instrument. By doing so, certain samples can be measured more conveniently without complex sample preparation and moreover it enables the in situ monitoring of certain thin film growth behavior. For example, the precursor adsorption, reaction with substrate surface and the initial thin film nucleation can be detected instantaneously without affecting the processing conditions. ATR technique is based on the principle of total reflection, which happens when the light wave transmitted from a high refractive index medium into a low refractive index medium and the

incidence angle is larger than certain critical angle. For ATR-FTIR, the high refractive index medium is the optical crystal and the low refractive index medium is the sample, which is in close proximity to the crystal surface. When the IR light is totally reflected at the internal crystal surface, a part of this IR wave called the evanescent wave can penetrate through the surface and interact with the sample at the external surface of the crystal. The penetration depth can be as deep as a few microns, and is dependent on the frequency of the IR light, the optical properties of the ATR crystal and the properties of the sample.[21] A schematic of the multiple reflection ART-FTIR spectroscopy is showed in Fig.4 below.

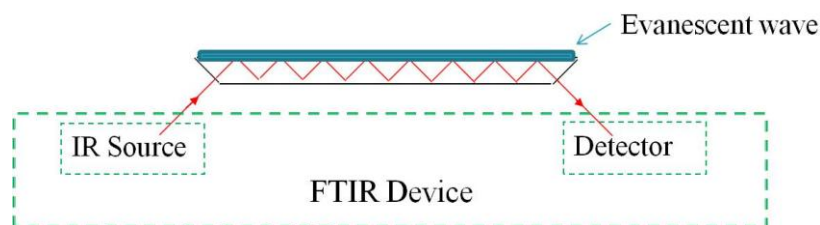


Fig. 4. Schematic of multiple reflection ART-FTIR spectroscopy.

Different materials can be used as the ATR crystal, such as silicon, germanium, zinc selenide (ZnSe) and zinc sulfide (ZnS). Among these materials, ZnSe has the broadest IR transmittance window ($20000\sim 700\text{ cm}^{-1}$), but the hardness and IR useful temperature is low compared to the others. Silicon is usually the substrate material for microelectronic thin films deposition. Although the IR transmittance range is narrower ($9500\sim 1500\text{ cm}^{-1}$), most useful vibration modes are included in this range, such as C-H, Si-H, O-H, etc.. Therefore, it's a very useful tool for the surface adsorption and reaction analysis of certain metal organic precursors on a silicon surface.

1.2.3.2 X-ray Photoelectron Spectroscopy (XPS)

XPS is a technique for surface chemical composition analysis. The basic principle is irradiating the sample surface in vacuum by soft X-rays, such as Mg K α (1253.6 eV), Al K α (1486.6 eV) and monochromatic Al K α (1486.7 eV), and analyzing the kinetic energies of generated photoelectrons by a spectrometer. A schematic of the photoelectron generation process is shown in Fig. 5.

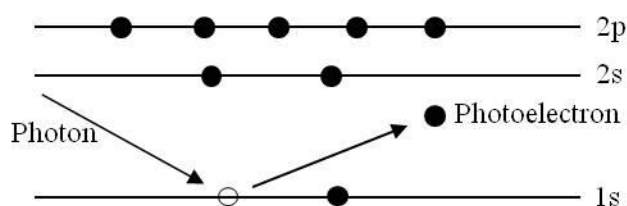


Fig. 5. Schematic of photoelectron generation process.

Based on the energy level of the X-rays used, core level electrons instead of valence electrons are knocked out of the atomic orbital as shown in Fig.5. The kinetic energy of the as detected electrons can be an indication of the identity of the element from which the electrons originate. This is based on the equation of energy conservation during the photoelectric effect, which is given by:

$$KE = h\nu - BE - \phi_s \quad (1.8)$$

where $h\nu$ is the energy of the photon, BE is the binding energy of the atomic orbital from which the electron originates, and ϕ_s is the spectrometer work function. Because of the difference in binding energies for electrons at different atomic orbitals, for each element, there is a unique XPS energy spectrum. An XPS spectrum is usually plotted in the form of number of electrons versus the kinetic or binding energy of the as-detected electrons. Besides the sharp peaks

representing those characteristic photoelectrons, a continuous background of electrons is also present in the spectrum. These background signals are mainly from the energy loss electrons due to inelastic scattering effect when they escape from the sample. Although the as used X-rays can penetrate as deep as few microns into the sample, the as generated photoelectrons can just travel through tens of angstroms distance in the material without losing energy. Therefore, the XPS is very surface sensitive and only chemical information of tens of angstroms beneath the sample surface can be characterized. Depth profile XPS analysis can be done by using ion gun etching, but the energetic bombarding ions can also induce chemical changes to the sample surface. Angle resolved XPS is another way to get information of chemical composition distribution with depth. Depending on the take-off angle, more signal could be collected either from the surface or the sublayer.[22] However, the range of probing depth is still limited to the range of tens of angstroms. Auger lines are often present in the XPS spectra too, which is from the process of Auger electron ejection that releases the excessive energy in the excited ion left after photoelectron emission. These lines can also be important for the interpretation of XPS spectra. The p, d, f levels become split upon ionization, leading to vacancies in the $p_{1/2}$, $p_{3/2}$, $d_{3/2}$, $d_{5/2}$, $f_{5/2}$, and $f_{7/2}$. The spin-orbit splitting ratio is 1:2 for p levels, 2:3 for d levels and 3:4 for f levels. [23]

Either qualitative or quantitative results could be achieved by XPS analysis. A main issue for chemical state identification is the charging effect for insulating samples. Surface deficiency of electrons could make the surface a little positive charged and thus lower the kinetic energy of the as detected electrons. Usually this charging effect is in a balanced steady state during measurement and all the peaks in the XPS spectra shift a few electron volts to a higher binding energy position. Neutralizer (electron flooding) can be used to minimize this charging effect, but since it's always hard to determine the degree of charging, more flooding electrons could make

the surface negative charged. Another way is to shift the peaks based on the adventitious C (284.8 eV), which is always present on the sample surface after air exposure. For a homogeneous sample, the number of photoelectrons per second in a specific spectra peak is given by:[22]

$$I = n f \sigma \theta y \lambda A T \quad (1.9)$$

where n is the number of element per cm^3 of the sample, f is the x-ray flux in photons/ cm^2 -sec, σ is the photoelectric cross-section for the atomic orbital of interest in cm^2 , θ is an angular efficiency factor for the instrumental arrangement based on the angle between the photon path and detected electrons, y is the efficiency in the photoelectric process for formation of photoelectrons of the normal photoelectron energy, λ is the mean free path of the photoelectrons in the sample, A is the area of the sample from which photoelectrons are detected, and T is the detection efficiency for electrons emitted from the sample. If we define $f \sigma \theta y \lambda A T$ as the atomic sensitivity factor, S . The ratio of surface concentration between two elements can be express as below.

$$\frac{n_1}{n_2} = \frac{I_1/S_1}{I_2/S_2} \quad (1.10)$$

For any spectrometer, it's possible to develop a set of relative values of S for all of the elements. Multiple sets of values may be necessary for instruments with multiple x-ray sources at different angles relative to the analyzer. A general expression for determining the atom fraction of any constituent in a sample, C_x , can be written as:

$$C_x = \frac{n_x}{\sum n_i} = \frac{I_x/S_x}{\sum I_i/S_i} \quad (1.11)$$

1.2.3.3 X-ray Diffraction (XRD)

X-ray diffraction is a classic technique for crystal structure characterization. X-rays that can be used to probe the material structures in atomic scale (few angstroms) have wavelengths in the same order. They usually possess much larger energies than those used for XPS analysis and are thus called hard X-rays. Generation of these X-rays starts from the bombardment of anode source materials, such as Cu, Co, Ag, Cr, or Fe etc., with a focused high energy (tens to hundreds of keV) electron beam. When electrons strike these materials, they are decelerated and a continuous spectrum of X-ray is emitted known as Bremsstrahlung radiation. High energy electrons can also knock inner shell electrons out of the atoms and leave vacancies in those shells. When an outer shell electron falls into the inner shell to fill the vacancy, the excessive energies left will be relieved by emission of characteristic X-ray photons. The as emitted X-ray possess the energy (wavelength) characteristic of the shell energy gap of atoms of the source material. For example, Cu $K\alpha$ X-ray frequently used in XRD measurement has a wavelength of $\sim 1.5418\text{\AA}$ ($\sim 8.04\text{ keV}$) and $K\alpha$ here represents the X-ray originating from the action of filling up a vacancy in K shell by a L shell electron.

$$n\lambda = 2d \sin \theta \quad (1.12)$$

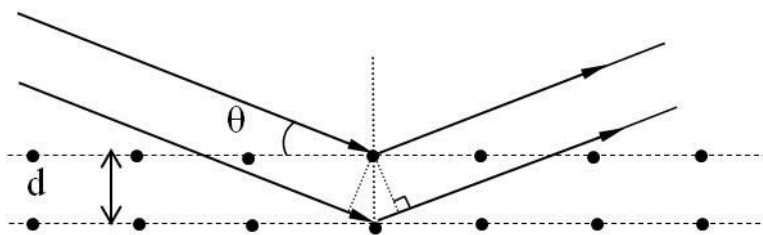


Fig. 6. Geometric derivation of Bragg's law.

X-ray diffraction behavior on crystalline materials is vividly described by Bragg's law (1.12), which clearly illustrates the relationship between X-ray wavelength (λ), lattice parameter (d) and the diffraction angle (θ). The geometric derivation of Bragg's law is showed in Fig.6. The difference of path length between the two diffracted X-ray beams determines the interference situation, e.g., a constructive interference will happen when this difference is an integral number multiple of the X-ray wavelength. By using this equation, accurate lattice parameters can be determined by measuring the diffraction angle with a fixed X-ray wavelength. Typical XRD instruments for thin film analysis have a configuration as showed Fig.7. Usually the incident beam from the X-ray tube is fixed and the goniometer and detector move in $\theta(\omega)$ and 2θ angles and keep in a reflection geometry. The in-plane (ϕ) and out-of-plane tilting angles (ψ) enable the instrument to do texture and pole figure analysis which can greatly improve understanding of the crystalline quality, especially for epitaxial thin films.[24]

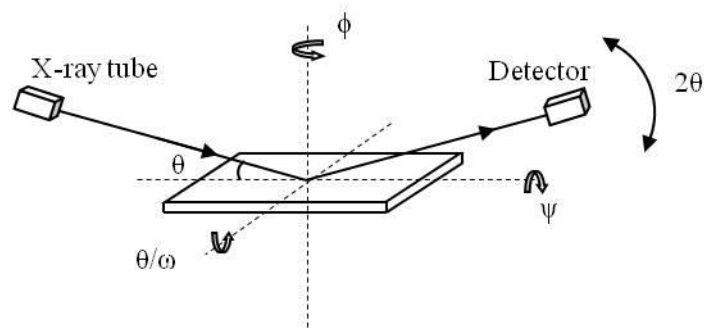


Fig. 7. Schematic of X-ray diffractometer for thin film crystal structure analysis.

The rocking curve, which is obtained from scanning the angle of ω at a fixed diffraction angle (2θ), provides valuable information about the out-plane texture of epitaxial films. For non epitaxial films, more than one lattice plane could be parallel with the thin film surface and

exhibit diffraction peaks in the normal θ - 2θ scan. The ratio of peaks height is a way to indicate the degree of growth at preferential orientation. ϕ -scan is a way to characterize the in-plane texture of epitaxial films, in which a diffraction plane not parallel with the film surface is tilted to the diffraction position. For example, for films with cubic structure and (001) plane parallel to the film surface, planes of (101), (011), ($\bar{1}01$), ($0\bar{1}1$) can be characterized by ϕ -scan to indicate the in-plane texture. The as-scanned peak, either from ω -scan or ϕ -scan, provide the texture information by the peak width, full width at half maximum (FWHM). Generally the narrower the peak, the better the film epitaxial quality.

Epitaxial films are usually strained as a result of lattice mismatch and/or difference in thermal expansion coefficient between the film and substrate. For films with cubic structure, the strain effect could make the structure slightly tetragonal. The calculation of both in-plane (a) and out-of-plane (c) lattice parameters is thus important to understand this behavior.

$$\sin^2\theta=A(h^2+k^2)+Bl^2+C\left\{10\sin^22\theta\left(\frac{1}{\sin\theta}+\frac{1}{\theta}\right)\right\} \quad (1.13)$$

For cubic/tetragonal structure, Cohen's method,[25,26] Eqa.(1.13), has been proved to be accurate and reliable, where θ is the diffraction angle, λ is the X-ray wavelength, and A, B and C are $\lambda^2/4a^2$, $\lambda^2/4c^2$ and a constant, respectively. By measurements of Bragg angles for various (hkl) planes, one can determine coefficients A, B and C by least square fitting.

1.2.3.4 Atomic Force Microscopy (AFM)

AFM is tool for nanoscale surface imaging, measuring and manipulating, which was invented in the early 1980s by scientists from IBM.[27] Different from its precursor, scanning tunneling microscopy (STM), which requires certain degree of surface conductivity of the sample, AFM can measure both conductive and insulating materials. AFM has been widely used

in thin film surface characterization. The basic working principle of AFM is based on the distance dependency of interatomic forces. As shown in Fig.8, when a sharp tip is brought into proximity of the sample surface, the interatomic forces (attractive or repulsive) deflect the tip attached cantilever up or down. This deflection is detected by a reflected laser beam system and with the tip raster scanning the surface the instantaneous deflection signal is used by a feedback loop to tune the vertical position of the cantilever or the sample stage to keep a constant force (deflection) between the tip and the sample surface. The as generated AFM image illustrates the surface height profile (topography) for a scanned area of the sample surface.

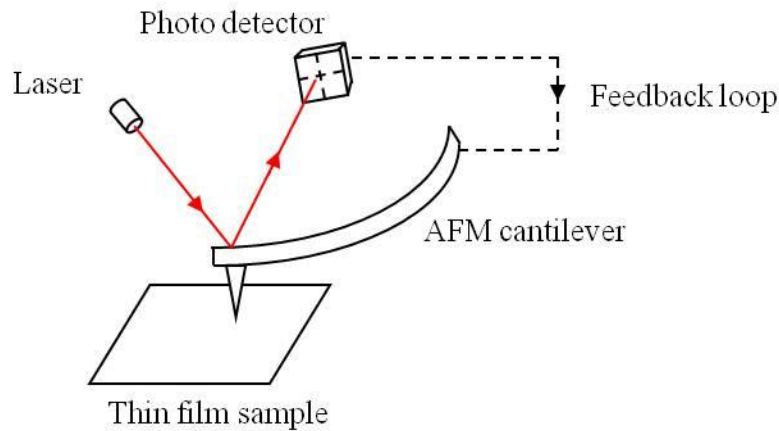


Fig. 8. Main components of atomic force microscopy system.

AFM can operate in different modes, such as contact mode and tapping mode, to meet the specific requirements of the sample being measured. Contact mode is also called static mode, in which the tip is brought so close to the surface and only repelling interatomic forces exist. In this mode, the potential issue of surface or tip degradation with continuous scanning limits its application to certain soft samples. Tapping mode, however, can avoid this issue by oscillating the cantilever in its resonant frequency. The resonance amplitude dependent on the surface height is usually kept constant for AFM scanning. Based on the tip radius of curvature

(nanometers to tens of nanometers), AFM can generate images with resolution of sub nanometer, which is higher than scanning electron microscopy (SEM) and comparable to transmission electron microscopy (TEM). Therefore, for very smooth thin film, which has surface RMS roughness below one nanometer, AFM is a preferred option due to its resolution capability and much easier sample preparation than TEM. Also, AFM can operate in air or even liquid environment, which makes it very versatile surface imaging technique. However, AFM has its own limitations such as the small imaging dimension (tens of microns) and slow imaging speed (few minutes to take one image).

1.2.3.5 Ferromagnetic Resonance (FMR)

FMR spectroscopy is a technique to probe the magnetization in ferromagnetic (or ferrimagnetic) materials. Different from nuclear magnetic resonance (NMR), the as-detected magnetic moments is from the exchange coupled unpaired electrons. Nowadays, it has been recognized as a standard tool for probing spin waves and spin dynamics.[28]

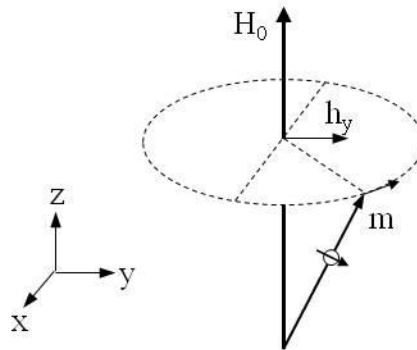


Fig. 9. Magnetic dipole moment precessing about a static magnetic field.

The FMR phenomenon arises from the precessional motion of magnetization (Fig.9) in a ferromagnetic/ferrimagnetic material which is in a static magnetic field. Usually the magnetic

field is strong enough to saturate the sample. To minimize the system potential energy, the magnetization will be aligned with the direction of the static magnetic field. When a microwave field is applied in the plane perpendicular to the static magnetic field. The magnetization will precess around the equilibrium direction. The classical equation of motion of magnetization (\vec{M}) is showed as eqa.(1.14). It's noteworthy that this equation is for an ideal case, where no damping effect of the precessional motion is considered and this is actually not true for practical ferromagnetic materials.

$$d\vec{M}/dt=\gamma(\vec{M}\times\vec{H}) \quad (1.14)$$

In this equation, γ is the gyromagnetic ratio (2.8 MHz/G), \vec{H} is the total magnetic field applied on the magnetization including both internal and external fields, such as the static magnetic field, microwave field and the demagnetizing field. Due to the time varying microwave field ($\vec{h}e^{j\omega t}$) with frequency ω , there exists a induced time varying magnetization ($\vec{m}e^{j\omega t}$) with the same frequency. If we neglect the effect of anisotropy, magnetostriction and exchange interaction, the internal static field is equal to the external applied static field (\vec{H}_0). When solving the equation of motion for \vec{m} , there is a singularity when $\omega=\gamma\vec{H}_0$ and this is the condition of ferromagnetic resonance based on the assumptions above.[29] For practical ferromagnetic/ferrimagnetic sample, especially thin film samples, the resonance condition will be different due to various contributions to the internal magnetic field.

In a typical FMR setup, a resonant cavity and electromagnets are used to exert the orthogonal static and microwave fields on the sample. The intensity of the microwave signal after the cavity is detected to determine the absorption behavior. When the precessional frequency of the sample being measured is equal to the fixed frequency of the resonant cavity the

strongest absorption of microwave signal is observed and that is the ferromagnetic resonance phenomenon. Either the frequency or static magnetic field could be swept to observe the resonance and get the FMR spectrum. The line width of the as achieved FMR curve is an indication of the resonance damping behavior, which represents the degree of microwave loss. Usually narrow line width is preferred for low microwave loss devices. The FMR damping behavior is sensitive and directly related to many factors of the thin film material such as crystal defects, chemical inhomogeneity, surface roughness and interface diffusion, etc..[30-32] Therefore, It's analysis is quite useful for certain thin film device applications.

1.3 Thin Film Application in Electronic and Magnetic Devices

1.3.1 Metal Oxide Field Effect Transistor (MOSFET)

MOSFET is a type of transistor mostly used in integrated circuits (IC) for amplifying or switching electronic signals. A n-type MOSFET structure is showed in Fig.10. By applying voltage on the gate electrode, which is separated from the semiconductor body by a thin insulating oxide layer, an electric field is generated through the oxide layer and affects the distribution of charged carriers in the interface between the oxide layer and the semiconductor body. For this n-type MOSFET, the semiconductor body is doped into p type and the source and drain regions are doped into n type. When a positive voltage is applied on the gate electrode, the as generated electric field will repel the positive holes away from the layer right below the oxide and a conducting n-type channel (inversion layer) will be formed between the source and drain. Therefore, by adjusting the gate voltage, the current through source and drain can be turned on or off. The onset of strong inversion is defined in terms of a threshold voltage V_{th} being applied to the gate electrode relative to the other terminals. In order to assure that the induced inversion channel extends all the way from source to drain, it is essential that the MOSFET gate structure

either overlaps slightly or aligns with the edges of these contacts (self-alignment process). Self-alignment is preferable since it minimizes the parasitic gate-source and gate-drain capacitances.[33]

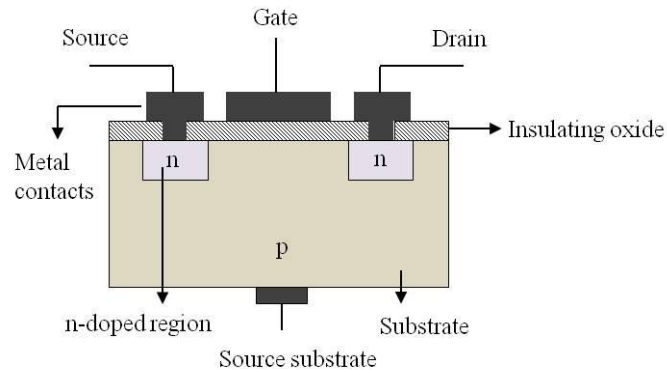


Fig. 10. Schematic of a n-channel MOSFET.

There are three operation modes for practical MOSFET devices. The first one is called subthreshold mode and it happens when the gate source voltage V_{GS} is lower than V_{th} . Under this situation, due to the Boltzmann distribution of electron energies, there are still some high energy electrons that can flow through the channel and results in a leakage current. This current has been found exponentially dependent on the value of V_{GS} . When $V_{GS} > V_{th}$ and the drain-source V_{DS} voltage is less than the value of $V_{GS} - V_{th}$, the MOSFET is in the linear mode. In this mode, the conducting channel is created for current flow from drain to source and the MOSFET operates like a resistor. The current is almost linearly dependent on V_{DS} under a fixed gate voltage. By changing the gate voltage, the resistivity of the conducting channel is changed too. The third mode is saturation mode when $V_{GS} > V_{th}$ and $V_{DS} > (V_{GS} - V_{th})$. In this mode, the transistor is in its constant current region and is switched fully on. The onset of this mode is also known as

pinch-off to indicate the lack of a channel region near the drain. The drain current is now weakly dependent upon the drain voltage and controlled primarily by the gate source voltage (V_{GS}).

In the past few decades, the continuous scaling down of the MOSFET in size has revolutionized the development of the microelectronic industry. The channel length of the MOSFET structure has been shrunked from microns to tens of nanometers. At this scale, a lot more functionalities can be realized in a same size wafer and meanwhile the cost of fabrication can be decreased. However, with this scaling down, few operational problems have been found. For example, the voltage applied to the gate has to be reduced to maintain reliability. To maintain performance, the threshold voltage needs to be reduced too. With the reduced V_{th} , the transistor cannot be switched from completely off to completely on with the limited voltage swing available. Subthreshold voltage can thus consume as much as half of the total power consumption. Another problem is with the gate oxide layer: as the thickness of this layer going down to few atomic layers, the electron tunneling effect occurs and makes the power consumption even higher. High-k materials (such as hafnium silicate or oxide) have been developed to replace the traditional oxide material since the layer can be made thicker while maintaining the same capacitance.[34-36] To work with these new high-k materials, the properties of the gate electrode materials have to be considered as well. The traditional gate electrode material polysilicon, for example, when coupled with a very thin (~1 nm) dielectric layer, a phenomenon observed is poly depletion, where a depletion layer is formed in the polysilicon layer next to the dielectric layer when the transistor is in the inversion. To avoid this problem, metal gate materials such as tantalum carbide, tantalum nitride and titanium nitride can be used with high-k dielectrics.[37-39]

1.3.2 Ferrite-Ferroelectric Layered Heterostructures

Ferrites (spinel, garnet or hexaferrite structure) have been long known as microwave materials due to their high permeability and resistivity. When used in tunable microwave devices, such as band-pass filters, phase shifters, or resonators, the microwave propagation behavior in these materials could be changed by variation of a bias dc magnetic field. This is because of the change of the permeability of the ferrites resulting from the changing bias magnetic field. This magnetic tuning is possible over a very wide frequency range, but it is slow and is associated with large power consumption. Another way of microwave tuning is using ferroelectric materials, in which electric field can be used to tune the dielectric constant of the materials and thus change their microwave properties. The tuning by electric field is fast and energy efficient, but usually the tunable frequency range is very narrow. A combination of ferrite and ferroelectric materials into composite or layered structures could provide the possibility of simultaneous magnetic and electric tuning.[40-43] This dual tuning allows the high efficiency of magnetic tuning and the high speed and low power requirements of electric tuning to be combined. For the work of this dissertation, only layered structure is introduced here.

Studies on layered ferrite-ferroelectric structures have showed great importance for both fundamental understanding of high frequency magnetoelectric (ME) effect and various microwave applications. Two types of layered structures have been investigated. The first one is ME coupling in bonded bilayers, in which the deformation (strain) of the ferroelectric layer due to applied electric field results in a magnetic property change of the ferrite layer. Basically, this strain effect could change the internal magnetic field and thus generate shift of the ferromagnetic resonance (FMR) field. The degree of coupling depends on both the piezoelectric and magnetoelastic constants of the ferrite and ferroelectric material being used. The other type of

coupling is from unbound ferrite-ferroelectric bilayers, in which hybrid spin-electromagnetic oscillations and waves are formed.[44,45] Strong ME coupling behavior has been found in both type of structures.

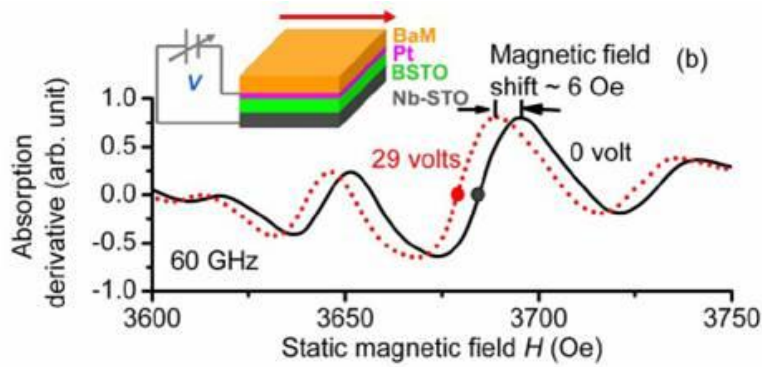


Fig. 11. ME coupling in a ferrite-ferroelectric layered structure. Reproduced with permission from ref. [46].

The degree of ME coupling effect is usually measured by the shift of FMR resonance curve. Fig.11 showed the ME effect in a unbound ferrite-ferroelectric bilayer structure.[46] The as used ferrite material is barium hexaferrite (BaM, $\text{BaFe}_{12}\text{O}_{19}$) and the ferroelectric materials is barium strontium titanate (BSTO, $(\text{Ba},\text{Sr})\text{TiO}_3$). At a fixed resonance frequency (60 GHz), a FMR shift of 6 Oe is observed by applying 29 V voltage to the BSTO layer.

To improve the ME coupling effect, high quality materials are essential for both ferrite and ferroelectric layers. Different thin film deposition methods have been investigated for the preparation of either the magnetic or the ferroelectric layer. However, to get both high quality and relatively thick (few microns to tens of microns) layers is still challenging.

CHAPTER 2. LITERATURE REVIEW

Chemical vapor deposition of several electronic/magnetic thin film materials, i.e., Hafnium nitride (HfN), Nickel ferrite(NiFe_2O_4), Lithium ferrite (LiFe_5O_8), and Barium titanate (BaTiO_3) has been investigated in this dissertation work. All these materials in thin film format exhibit certain attractive properties and can be promising material candidates for various high technology devices. In this chapter, a literature review of the physical properties, potential applications, and various previously reported thin film growth methods for each material is presented and especially the development of CVD related studies are emphasized.

2.1 Hafnium Nitride (HfN)

2.1.1 Physical Properties and Potential Applications

Hafnium nitride (HfN), a transition metal nitride, has a rock salt structure with lattice constant of $\sim 4.53\text{\AA}$ (Fig.12). It possesses various superior properties, such as, low bulk resistivity ($33\mu\Omega\cdot\text{cm}$), high melting point (3380°C), high hardness and density, low work function ($\sim 4.8\text{eV}$) and good chemical inertness [47-49]. Because of these excellent properties, HfN can be used as protective coatings on high speed cutting tools, field emission cathode, and gate electrode and

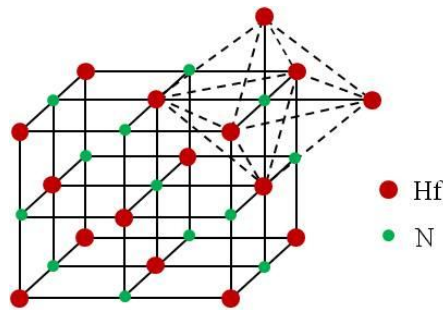


Fig. 12. Unit cell of HfN crystal with cubic structure.

diffusion barrier material in microelectronic devices[50-52], for instance, the potential application of HfN as a gate electrode material in the metal–oxide–semiconductor field-effect transistor (MOSFET). It has been well known that the substitution of traditional gate oxide SiO₂ with high-k material HfO₂ can dramatically accelerate the scaling down of size of MOSFETs. However, coupling HfO₂ with conventional gate electrode layer (poly silicon) will generate issues like boron penetration and the formation of a low-k interfacial layer, which will affect the performance of the whole device.[53] HfN can be a good candidate to replace poly silicon to work with HfO₂ as a gate stack due to its excellent properties mentioned above. It has been found that equivalent oxide thickness (EOT) of HfO₂-HfN gate stack can be scaled down to less than 1 nm with excellent leakage and long term reliability even after 1000°C post metal annealing. Fig.13 below shows the well behaved electrical characteristics (I_d - V_g , I_d - V_d) of the n-MOSFET with an excellent subthreshold slope of 78 mV/dec. The as-used HfN film was deposited by DC magnetron sputtering of a Hf target in mixed Ar+N₂ gas ambient. [52]

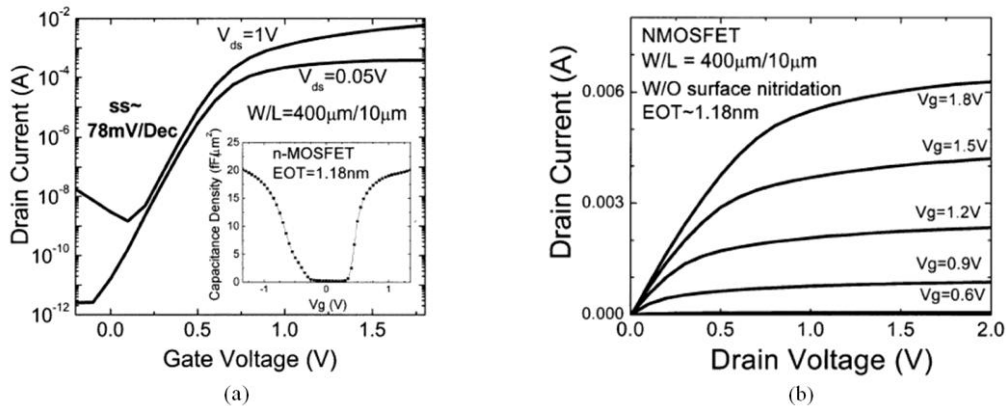


Fig. 13. (a) I_d - V_g and (b) I_d - V_d characteristics of an n-MOSFET using HfN-HfO₂ gate stack with EOT 1.18 nm. Reproduced with permission from ref. [52].

2.1.2 Review of HfN Thin Film Growth

Different methods of HfN thin film deposition have been investigated in the past few decades. Physical vapor deposition methods such as RF/DC magnetron sputtering [54-58],

pulsed laser deposition [59], nitrogen ion implantation [60] and nitrogen ion beam assisted evaporation [61] have been reported. However, the poor step coverage which comes intrinsically with PVD methods makes it not appropriate for certain microelectronic applications. Comparatively, CVD methods have the advantages of larger area deposition, better step coverage and better control of morphology and stoichiometry over PVD methods. In the development of CVD deposition of HfN thin films, the introduction of tetrakis (dialkylamido) hafnium (IV) complexes [62] as hafnium precursors is an important step. The representative precursors and their vapor pressures are showed in table 1.

Table 1. Hafnium amide precursors and their properties.[63]

Precursor	Chemical formula	Melting point (°C)	Temp (0.1 torr) (°C)	Temp (1 torr) (°C)
Tetrakis (dimethylamido) hafnium	$\text{Hf}(\text{N}(\text{CH}_3)_2)_4$	30	48	75
Tetrakis (ethylmethylamido) hafnium	$\text{Hf}(\text{N}(\text{CH}_3)(\text{C}_2\text{H}_5))_4$	liquid	83	113
Tetrakis (diethylamido) hafnium	$\text{Hf}(\text{N}(\text{C}_2\text{H}_5)_2)_4$	liquid	96	126

Most of the following studies are based on these metal organic precursors due to their higher chemical reactivity than hafnium chloride, which needs a very high temperature (>1000°C) to react with N_2/H_2 to form HfN [64]. The CVD reaction of tetrakis (dialkylamido) hafnium (IV) with ammonia was first studied but resulted in the formation of the insulating phase, Hf_3N_4 , instead of the conductive phase, HfN [62,65,66]. Highly conformal Hf_3N_4 films have been successfully deposited on high aspect ratio surface features, as shown in Fig.14, by ALD method using tetrakis (dialkylamido) hafnium and ammonia.

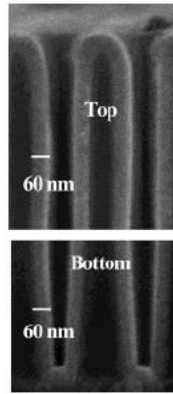


Fig. 14. A cross sectional scanning electron micrograph of uniform Hf_3N_4 thin film coating by ALD on a high aspect ratio trench structure ($0.17 \mu\text{m} \times 0.3 \mu\text{m} \times 7.3 \mu\text{m}$). Reproduced with permission from [67].

To improve conductivity of the as deposited thin films, the effect of post rapid thermal annealing [68] and Ar^+ ion milling [69] have been studied. Both of these methods work to a certain degree by improving the ratio of Hf to N. To satisfy the oxidation state change of hafnium element from the precursor (+IV) to the product (+III), utilization of a stronger reducing agent of N,N-dimethylhydrazine ($\text{H}_2\text{NN}(\text{CH}_3)_2$) has been proposed and studied [70]. In spite of the formation of relatively pure HfN thin films, the high reaction temperature ($600\sim 800^\circ\text{C}$) and the use of a toxic reactant severely limit its application. By employing hydrogen plasma as reducing agent, two groups have investigated the atomic layer deposition of HfN thin films with tetrakis (dimethylamido) hafnium (TDMAH) and tetrakis (ethylmethylamido) hafnium (TEMAH) respectively [71,72]. In these studies, the hafnium precursors played the role of both a Hf and a N source. It was found that the incorporation of carbon in the phase of hafnium carbide can improve the thin film conductivity to a certain degree. In our research, a systematic study on both CVD and ALD methods by using TDMAH and hydrogen plasma will be carried out. Potential issues and corresponding reaction mechanisms with these methods will be analyzed and proposed according to our experimental results.

2.2 Spinel ferrite: Nickel Ferrite and Lithium Ferrite

2.2.1 Physical Properties and Potential Applications

Nickel ferrite (NiFe_2O_4) and lithium ferrite (LiFe_5O_8) belong to the family of ferrimagnetic ferrites, which possess both high permeability and resistivity.[73] In terms of crystal structure, NiFe_2O_4 and LiFe_5O_8 are both spinel structure. In a spinel (AB_2O_4) structure, the unit cell consists of eight formula units and the 8 A^{2+} and 16 B^{3+} cations are distributed in the interstices of the 32 close packed oxygen anions (Fig.15). If all of the 8 A^{2+} occupy tetrahedral sites and all of the 16 B^{3+} occupy octahedral sites then the structure is called normal spinel; If all of the 8 A^{2+} and 8 B^{3+} occupy octahedral sites and 8 B^{3+} occupy tetrahedral sites, the structure is called inverse spinel.

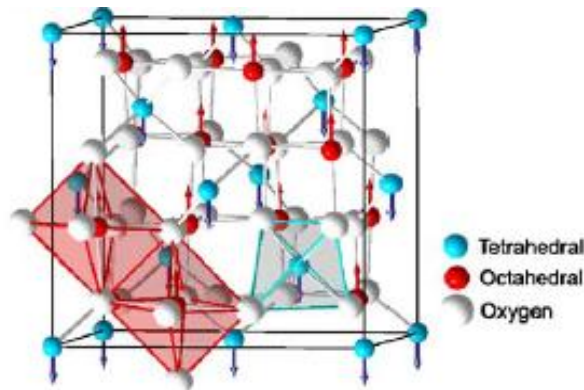


Fig. 15. Representation of a spinel structure. Adapted from ref. [73].

Usually, NiFe_2O_4 and LiFe_5O_8 both exist in inverse spinel structure at room temperature and their formulas can be written as $\text{Fe}^{3+}[\text{Ni}^{2+}\text{Fe}^{3+}]\text{O}_4$ and $\text{Fe}^{3+}[\text{Li}^{+}_{0.5}\text{Fe}^{3+}_{1.5}]\text{O}_4$ respectively. According to the Néel model, the ferrimagnetism of these ferrite materials comes from a mechanism of superexchange, in which different magnetic cation occupied sublattices are antialigned with each other in the presence of an external magnetic field and thus imbalance in the number of antialigned sublattices results in net magnetism.

In spite of the same spinel structure, nickel ferrite and lithium ferrite have their own crystal parameters and physical properties due to different elements present in the materials. Nickel ferrite has a lattice constant of 8.340 Å, saturation magnetization of ~3200 G (room temperature) and Néel temperature of 585 °C. The effect of cation distribution and addition of different divalent cations (Zn^{2+} , Cu^{2+} , Mn^{2+}) on its magnetic properties have been widely investigated in the past.[74,75] This material is microwave lossy due to the orbital state of Ni^{2+} , a relaxing ion. Lithium ferrite exists in two states: ordered and disordered state. In the ordered phase, the lithium and ferric ions are ordered in a 1:3 molar ratio in the octahedral sites of the cubic structure. The disordered phase of lithium ferrite has a disordered face centered cubic structure where the lithium and ferric ions are randomly located in the octahedral interstices. The disordered phase is produced with quenching from high temperatures as it is formed and prevalent in the temperature range of 750~1000 °C. This is due to the relative diffusion rates of the ions in the cubic lattice. Slow cooling allows redistribution and ordering of the ions in the cubic lattice and provides the condition for reversion to ordered phase. The lattice parameters for the ordered and disordered phase are 8.337 Å and 8.333 Å, respectively. Lithium ferrite has a saturation magnetization of 3750G (room temperature) and Néel temperature of ~620 °C, which are both higher than that of nickel ferrite. A unique feature of lithium ferrite among those spinel ferrites is its low microwave loss, which is indicated by its extremely narrow FMR line width of less than 10 G at room temperature, as showed in Fig.16. It's much lower than the value of nickel ferrite (40~80G) and comparable to that of yttrium iron garnet ($Y_3Fe_5O_8$). This is because only S state Fe^{3+} ions present in this material. Another advantage of lithium ferrite is its low cost compared to YIG. However, its practical application is still limited by the challenges of high quality material preparation, especially for thin films. Also, for microwave applications, both

nickel ferrite and lithium ferrite are usually used only in low frequency bands (C or X band) and external magnets are needed to magnetically bias the material due to their intrinsic small cubic anisotropy.

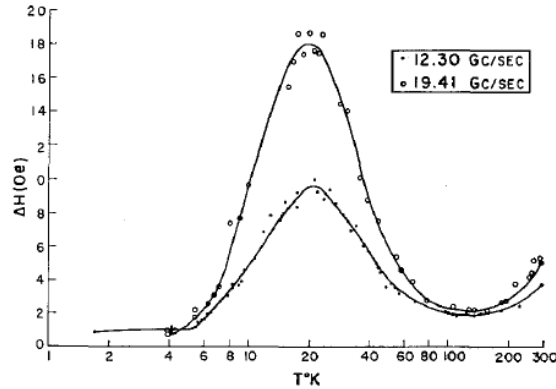


Fig. 16. Temperature dependence of FMR line width of bulk lithium ferrite single crystal in ordered phase (FMR measurement at two frequencies: 12.3 and 19.41 GHz). Reproduced with permission from ref. [76].

Nowadays, the potential application of thin films of these ferrite materials in next generation technologies, such as monolithic microwave integrated circuits (MMIC) and multiferroic heterostructures, has made them very attractive.[73,77,78] Considering the requirements of planar, smaller, weigh less and low loss for these microwave applications, much research attention has been attracted to the high quality thin film ferrites deposition.

2.2.2 Review of thin film growth methods

Different growth techniques for these ferrite films have been developed and investigated in the past few decades, such as chemical vapor transport,[79,80] chemical vapor deposition,[81-87] sputtering,[88-91] liquid phase epitaxy,[92-95] spin-spray plating,[96,97] and pulsed laser deposition.[98-104] However, the achievement of both high quality (structural, morphological, magnetic and microwave properties) and thick (1-10 micron range) epitaxial films for microwave device applications remains challenging.[105,106] For instance, pulsed laser deposition of spinel

ferrites has been investigated extensively due to the relative ease of stoichiometry control.[98-104] Nevertheless, potential issues such as small deposition area and poor thin film conformality have limited its use mostly to laboratory research. Low growth rate is another bottleneck for commercially viable device grade spinel ferrites for microwave applications. Liquid phase epitaxy, which can provide film growth rates as high as tens of microns per hour, is another promising method that has been widely studied. As a high temperature growth technique, challenges such as poor surface morphology (hillock growth) and chemical inhomogeneities due to interdiffusion between substrate and thin film, which can greatly influence thin film magnetic properties, are still unresolved (Fig.17). [107,93]

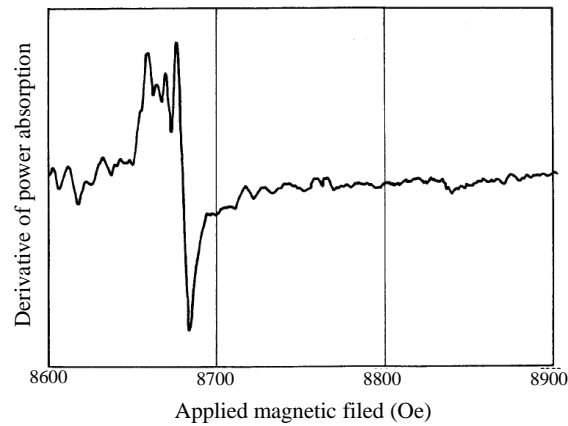


Fig. 17. FMR measurement (9.07 GHz, perpendicular) of lithium ferrite film grown by LPE method on $\text{Mg}(\text{In,Ga})_2\text{O}_4$ (111) substrate. Presence of inhomogeneity in the film is indicated by the complex FMR curve. Reproduced with permission from ref. [93].

The use of CVD for nickel ferrite film deposition has been limited by the availability of appropriate metal precursors having both high volatility and thermal stability. Early work (~1960s) investigated the use of solid metal halide precursors. But the high temperature ($>700^\circ\text{C}$) required to vaporize these precursors and the formation of corrosive hydrogen halides hampered further development.[81,82] More volatile metal acetylacetonate precursors for nickel ferrite deposition, $(\text{Ni}(\text{acac})_2$ and $\text{Fe}(\text{acac})_3$), have been utilized in subsequent studies.[108,109]

However, using traditional vaporization methods (bubbler or crucible), accurate control of vapor concentrations for the two components in order to obtain stoichiometric films is difficult, often resulting in unwanted impurity phases such as Fe_2O_3 or NiO . [108] Precursor oligomerization (e.g., $[\text{Ni}(\text{acac})_2]_3$) and weak thermal stability above 200°C are two additional drawbacks of this approach. [109] To the best of our knowledge, no research has been reported for lithium ferrite thin film deposition by using CVD technique with any metal organic precursors so far.

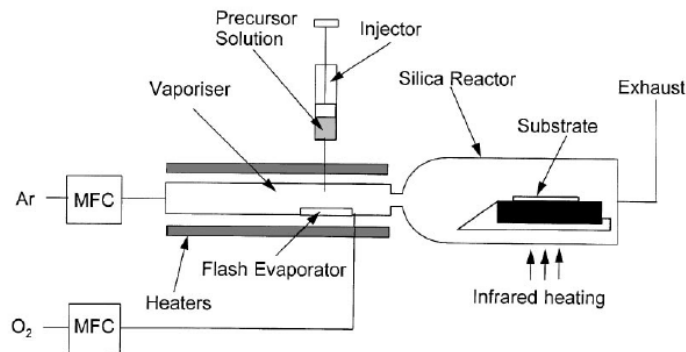


Fig. 18. Schematic diagram of a previous reported DLI-CVD system for nickel ferrite growth. Reproduced with permission from ref. [83].

The direct liquid injection (DLI) technique, which can generate vapor from a liquid solution source at relatively low temperatures ($< 200^\circ\text{C}$), has in recent years been successfully utilized for a number of metal-organic chemical vapor deposition processes. [110-112] DLI-CVD is a particularly useful method for multi-component systems as several precursors can be dissolved in the same solution and the relative delivery rates of precursors are defined by the solution composition. There are only a couple of reports in the literature on DLI-CVD of nickel ferrite, e.g., using metal thd (thd = 2,2,6,6-tetramethyl-3,5-heptanedionato) precursors. [83,85] In spite of reported polycrystalline/epitaxial growth of nickel ferrite on different substrates (Si(100) and MgO(100)), the as-deposited thin film characteristics (morphology and magnetic properties) are far from satisfactory as compared to bulk nickel ferrite. One of the DLI-CVD experimental

systems is showed in Fig.18.[83] As one can see, the simple syringe injection and hot plate flash vaporization has potential issues such as poor control of liquid injection rate and thermal decomposition of metal organic precursors by direct contact with the hot metallic surface. The properties of the films are greatly influenced by the specific vaporization procedure, the selection of metal organic precursors, solvent and substrate material, and especially processing conditions (temperature, pressure, etc.). In this dissertation, we report the epitaxial growth of both nickel ferrite and lithium ferrite films on various substrates by DLI-CVD using a commercial vaporization technique. Optimization of the DLI parameters, thin film growth mechanism, relationship between CVD processing conditions and thin film qualities will be investigated.

2.3 Barium Titanate (BaTiO_3)

2.3.1 Physical Properties and Potential Applications

Barium titanate (BaTiO_3) has a classical perovskite crystal structure with formula of ABO_3 , in which A and B represent cations of different size. In the structure of barium titanate, the larger Ba^{2+} cations and O^{2-} anions form a face-centered cubic (FCC) lattice and the smaller Ti^{4+} cation occupies the octahedral site (cubic center). Unit cell of perovskite barium titanate is shown in Fig.19. Barium titanate is a piezoelectric material. Above its curie temperature of 120°C , barium titanate exists in cubic phase and shows paraelectric effect. While below 120°C ($>5^\circ\text{C}$), it transits to tetragonal phase ($a=3.992\text{\AA}$, $c=4.032\text{\AA}$ at 20°C) resulting from a tiny distortion of the Ti^{4+} included octahedron. The coupling of these distorted octahedra in the crystal gives rise to large spontaneous polarization and thus barium titanate exhibits ferroelectric characteristic.[113]

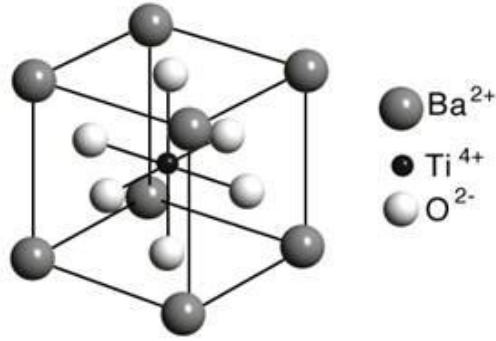


Fig. 19. Unit cell of perovskite BaTiO₃ crystal.

Due to its ferroelectric property and high dielectric constant, barium titanate has been recognized as a very useful material for certain cutting edge technologies, such as thin film capacitors, magnetoelectric heterostructures, and non-volatile ferroelectric random access memory (FeRAM) devices.[114] Besides, the desirable nonlinear optical properties of BaTiO₃ make it attractive for a variety of electro-optic and optical storage device applications.[115]

2.3.2 Review of thin film growth methods

Thin film deposition of BaTiO₃ has been investigated using different methods, such as RF sputtering,[116-119] evaporation,[120,121] pulsed laser deposition,[122-125] molecular beam epitaxy,[126] sol-gel[127] and chemical vapor deposition.[128-140] The achievement of single crystal, high quality, and good surface morphology has always been the goal for most deposition methods in order to fulfill the requirement of practical devices. Epitaxial growth of BaTiO₃ thin films has been found in both physical and chemical vapor deposition methods on different substrates, such as MgO,[117,122,130,135,136,138] TiO₂,[123] SrTiO₃,[116,136] LaAlO₃,[115,131,136] and NdGaO₃. [131] Chemical vapor deposition, as mentioned previously, has several advantages over physical vapor deposition. Studies on CVD of BaTiO₃ thin films have been reported since early 1990s. Its development has been based on the progress of

precursor vaporization process, e.g., better precursors or vaporization techniques. For conventional CVD processes using a heated bubbler or crucible to vaporize liquid or solid precursors (metalorganic, inorganic, alkoxide, etc.), it's difficult to realize controlled introduction of relatively involatile precursors and the repeatability of thin film growth is poor. The first step towards improvement is to search for or synthesize more volatile and thermal and chemical stable precursors. As for deposition of BaTiO₃, titanium tetraisopropoxide (Ti(OC₃H₇)₄, m.p. 20°C) is used as the Ti source in most CVD processes due to its high volatility, however, the use of the Ba precursor β-diketonate chelate such as Ba(tmhd)₂ (thd=2,2,6,6-tetramethyl-3,5-heptandionate) has been limited by its low volatility (m.p.>200°C) and run-to-run property changes (sintering effect).[115,131,135,138,139] Fluorination and introduction of neutral donor ligands have been found helpful to improve its volatility and reduce the tendency of oligomerization. For instance, Ba(hfa)₂(tetraglyme) (hfa=hexafluoroacetylacetonate) and Ba(hfa)₂(PEB) (PEB=pentaethyleneglycol ethyl butyl ether), which have melting points of 151°C and 71°C, have been synthesized and successfully applied to CVD of BaTiO₃ thin films.[115,138] A schematic of barium β-diketonate precursor is showed in Fig.20.

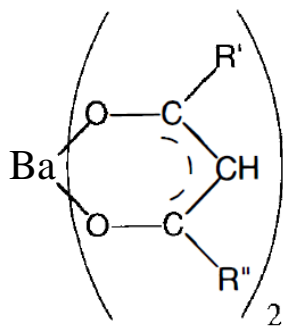


Fig. 20. Schematic of a β-diketonate precursor. R' and R'' represent the same or different alkyl groups.

Another way to break through the limitation of vaporization is the technique of direct liquid injection, in which the precursor containing the liquid source is injected into a vaporizer and is volatilized there before it's delivered into the CVD reactor by a carrier gas. In this way, the vaporization temperature can be dramatically decreased and the introduction of precursor can be accurately controlled by a sensitive liquid flow meter. A couple of studies have been reported based on this technique in CVD of BaTiO₃ or (Ba,Sr)TiO₃ thin films.[114,136,141] The reported results show that this can be a very promising technique for the deposition of high quality and thick BaTiO₃ films. Considering the desirability of thick (tens of microns) and high quality ferroelectric films in the study of magnetoelectric coupling effects in layered heterostructures,[142] our research on CVD of BaTiO₃ films will take advantage of the direct liquid injection technique.

CHAPTER 3. PLASMA ENHANCED ATOMIC LAYER DEPOSITION OF HAFNIUM NITRIDE FILMS

3.1 Introduction

Chemical vapor deposition of HfN can make films of high conformality and thus provide the possibility of fabricating high aspect ratio microelectronic structures. One of the challenges for this method is the selection of appropriate chemicals. Hafnium amide precursors have been successfully used in the deposition of HfO₂, Hf₃N₄ and HfN by reacting with oxygen (O₂), ammonia (NH₃) and dimethyl hydrazine (H₂NN(CH₃)₂) respectively.[63,67,70] For the deposition of HfN using dimethyl hydrazine, usually a high substrate temperature (600°C~800°C) is needed to initiate the reaction, which is not appropriate for certain thermal sensitive materials used in the microelectronic devices. Hydrogen plasma which has much higher reactivity than hydrazine can be used in low temperature plasma enhanced ALD process of HfN thin films.[71,72] In this chapter, the hafnium precursor tetrakis (dimethylamido) hafnium (IV) (TDMAH) used for thin film growth is studied first, i.e., in-situ monitoring of adsorption and reaction behavior of TDMAH on hydrogenated Si(100) by ATR-FTIR. It's important to understand the thermal decomposition and surface adsorption behavior of this precursor for ALD thin film growth, because it is directly related to the film contamination and interfacial bonding information.[143] PEALD of HfN thin film growth by using TDMAH and hydrogen plasma is studied. The as-deposited thin films were characterized by XPS, AFM, XRD, SEM and TEM to study the chemical composition, surface morphology and crystal structure information. Thin film

resistivity was measured by four point probe and its dependency on plasma power has been investigated.

3.2 Tetrakis (Dimethylamido) Hafnium (IV) (TDMAH) Adsorption and Reaction on Hydrogenated Si(100) Surface

3.2.1 Introduction

TDMAH is in the form of colorless to pale yellow crystal at room temperature, which has a melting point of around 30°C and a vapor pressure of around 0.1 torr at 48°C. This material is moisture sensitive and should be handled in low temperature and/or inert environment. Its molecular structure is showed in Fig.21.

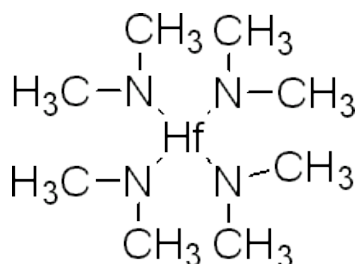


Fig. 21. Molecular structure of TDMAH.

One of the important concerns for ALD precursors is their thermal stability. If the precursors decompose in the process of transporting to the substrate surface or on the substrate surface, it's likely to induce continuous thin film growth and break the rule of self-terminating adsorption. It's noteworthy that the kinetics of thermal decomposition also has to be considered, if the degree of decomposition is negligible in the ALD cycle time range, it should not be a big issue to affect the thin film growth.[8] Another concern for the ALD precursors is the surface reactivity, i.e., the activation barrier for interfacial bond formation between the precursor and the surface dangling bonds has to be low enough to allow film growth. In-situ ATR-FTIR is one efficient way to achieve all of these information through monitoring the surface adsorption and reaction behavior of precursor molecules. TDMAH has been widely used in ALD of HfO₂, but

the initial surface chemistry for thin film growth is rarely investigated.[144] In this section, the temperature dependence of TDMAH adsorption, desorption and thermal decomposition on hydrogenated Si(100) surface is studied. Besides, Density Functional Theory (DFT) is used to calculate the IR spectrum of intact TDMAH molecule to help interpret the experimental IR results.

3.2.2 Experimental Details

The in-situ ATR-FTIR experimental setup is showed in Fig.22. The TDMAH (99%) precursor was bought from STREM Chemicals and used without any further purification. Before the in-situ ATR-FTIR experiment, the TDMAH in liquid phase was characterized by a 'liquid drop' experiment, in which the TDMAH precursor was directly loaded onto the crystal surface and measured by ATR-FTIR. For the TDMAH adsorption experiment TDMAH was loaded into a quartz tube bubbler. All the loading processes were in a nitrogen purged glove bag to minimize reaction/contamination with oxygen or water vapor.

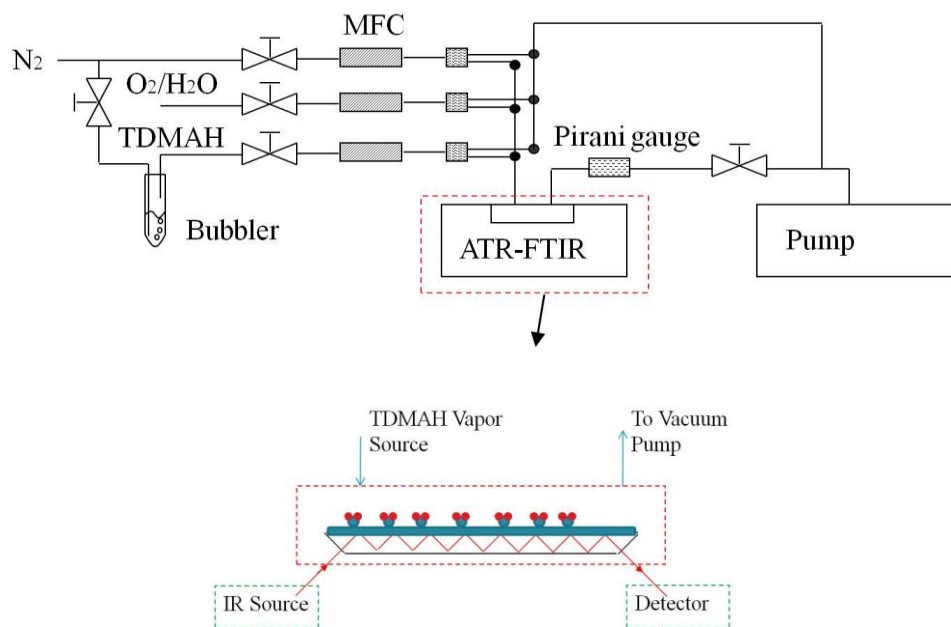


Fig. 22. Experimental setup of the in-situ ATR-FTIR.

In a typical in-situ ATR-FTIR experiment, the bubbler with loaded TDMAH was kept in an oil bath at 60°C. Around 20 min of stabilization is needed before introduction of the gas phase precursor into the ATR cell. No carrier gas was used in the experiments. The ATR cell, as shown in the bottom of Fig.22, uses a trapezoidal shaped crystal for enhanced surface sensitivity via multiple internal reflections of the IR beam along the long parallel faces of the crystal. The front face of the crystal is exposed to the precursor, while the IR beam enters and exits from the angled faces of the crystal from below. In the experiment, Si (100) crystals (Ge or ZnSe crystal for liquid drop experiment) with 45 degree bevels were mounted in a custom built flow through cell. With a crystal size of 50×10×2mm, the incident IR beam internally reflects 13 times off the TDMAH-adsorbed face before it reaches the DTGS (deuterated triglycine sulfate) detector (within Nicolet™ 4700 FTIR device). The sealing of the ATR cell uses a custom made Kalrez gasket between the cell frame and the crystal surface edges. The cell was roughly pumped (Rotary vane pump, Edwards RV3F) to a base pressure of about 5 mtorr. The crystal temperature could be controlled up to 250 °C, with the limitation from excited Si phonon modes resulting in reduced transparency of the crystal. Before each experiment, the gas delivering lines and the ATR cell were heated to around 100°C and purged with ultra high purity N₂ for 1 hour to minimize the water vapor concentration in the system. Once the valve between the bubbler and the ATR cell was opened, TDMAH started flowing into the ATR cell, the computer controlled IR spectra taking was simultaneously started. In this flowing mode, the surface adsorption and reaction behavior were instantaneously monitored. All the IR data were taken in the IR range of 400~4000 cm⁻¹ and averaged over 16 scans with a resolution of 4 cm⁻¹, which took 22 seconds for each spectrum. The IR spectra taking was preset into an automatic mode, in which the FTIR will take one spectrum by one spectrum until the preset number (30) of spectra was reached. A

delay time of 2 seconds between spectrum taking was also set. The TDMAH adsorption was monitored in the flowing mode (valve open) for the time range of 15 IR spectra (~6 min). After that, the bubbler valve was closed, when the ATR cell was still under pumping, the automatic IR spectra taking was still running one by one to monitor the surface desorption/reaction process until the preset number of spectra is reached. The first 15 spectra taken in the flowing mode are used to simulate the precursor pulse step in an practical ALD cycle, and the second 15 spectra in the pumping mode were used to simulate the purging step in an ALD cycle. These ATR-FTIR experiments were carried out under different crystal temperatures from room temperature to 250°C. In each experiment, a spectrum of the bare crystal was taken before the TDMAH vapor was introduced into the ATR cell and used for background subtraction.

The as used Si(100) ATR crystal was prepared to hydrogenated silicon surface by the procedures below:

1. Sequentially ultra sonication by organic solvents acetone and methanol (2 min each).
2. Rinse with DI water for 2 min.
3. Cleaning with a 1:1:5 solution of $\text{NH}_4\text{OH}+\text{H}_2\text{O}_2+\text{DI H}_2\text{O}$ at 80°C for 10 min to remove the organic contaminants.
4. Soaking in diluted BOE (buffered oxide etch, $\text{NH}_4\text{F}:\text{HF} = 10:1$, $\text{BOE}:\text{DI water} = 1:5$) for 20 s to remove the oxide layer.
5. Cleaning with a 1:1:6 solution of $\text{HCl}+\text{H}_2\text{O}_2+\text{DI H}_2\text{O}$ at 80°C for 10 min to remove metallic (ionic) contaminants.
6. Repeat step 4.
7. Rinse with DI water for 10 min.

8. Blowing dry with ultra high purity N₂.

TDMAH molecular modeling and bond dissociation energy (BDE) calculation were carried out by Density Functional Theory (DFT) coupled in Gaussian 03 software. The calculations were performed at the DFT level with the hybrid gradient-corrected B3LYP exchange-correlation functional. The geometry optimizations and frequency calculations were done with the 6-31+G(d,p) basis set for the first row atoms and the LanL2DZ relativistic effective core potential (RECP) basis set for the Hf atom, All energies were corrected with the zero point energies (ZPE). The software and computing resources are from Alabama Supercomputer Authority.

3.2.3 Results and Discussion

The TDMAH precursor was first characterized by ATR-FTIR in a 'liquid drop' experiment. Few drops of liquid TDMAH were loaded onto a Ge(100) ATR crystal in a nitrogen glove bag and the IR spectrum was taken under room temperature. The as taken IR spectrum is showed in Fig.23 (bottom). Since Ge (100) ATR crystal has a wider IR transmittance window than Si(100) at room temperature, vibrational modes as low as 700 cm⁻¹ can be observed. The top spectrum is from DFT molecular modeling of a TDMAH free molecule. The molecular structure of TDMAH is fully optimized before the frequency calculation. As one can see, the experimental and theoretical results match very well in spite of a small shift of the peak positions. One possible reason is that the experimental measurement is for the liquid phase TDMAH and the inter molecular interaction could thus influence the electronic structure of the molecules. All the peaks have been identified by considering the theoretical results and certain previous experimental IR studies on transition metal amides.[145,146] Bond dissociation energies of Hf-N and N-C bonds in the TDMAH molecule have been calculated to be 78.4 Kcal/mol and 69.7

Kcal/mol respectively. The stronger Hf-N bond makes it thermodynamically possible for the deposition of HfN without any extra N source.

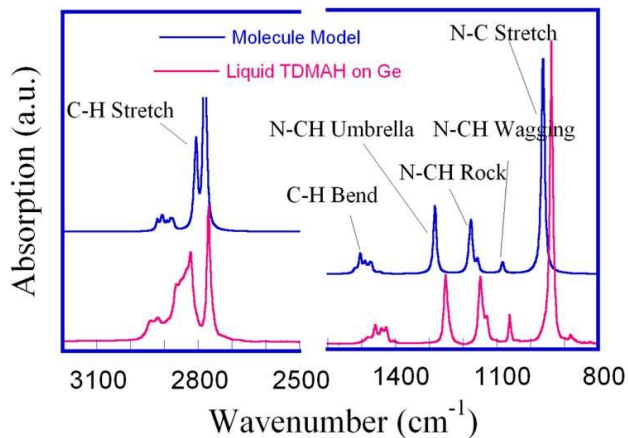


Fig. 23. Experimental and theoretical modeled IR spectrum of TDMAH.

In-situ monitoring of TDMAH adsorption on hydrogenated Si(100) surface is carried out at different substrate temperatures. Fig.24 shows the IR spectra after 2 min TDMAH adsorption at different crystal temperatures in the flowing mode.

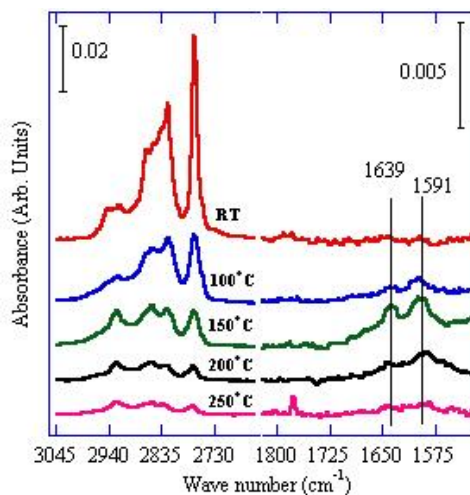
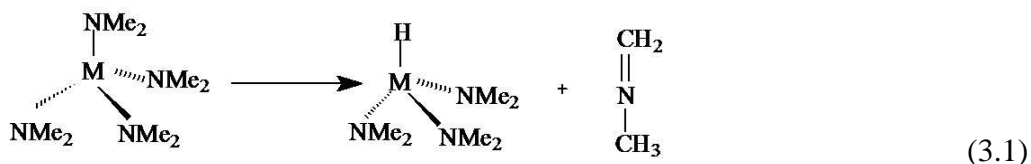


Fig. 24. IR spectra of TDMAH adsorption on hydrogenated Si(100) at different temperatures.

The spectrum taken at room temperature is the same as that observed in the liquid drop experiment, which indicates the physisorption and homogeneous condensation behavior of TDMAH at room temperature. With increasing substrate temperature, apparent changes happened both in the C-H stretching region and the $\sim 1600\text{ cm}^{-1}$ region. The decreasing peak intensity of 2770 cm^{-1} , which represents one of the C-H stretching modes that influenced by the lone pair electrons on N, indicates bond dissociation in the intact TDMAH molecules.[147] The peaks at 1591 cm^{-1} and 1639 cm^{-1} starts at 100°C and becomes much stronger at 150°C should be attributed to bonds in certain TDMAH decomposition products. Based on certain IR research on transition metal amides (Ti, Zr, V, Nb), we tentatively assign the peaks to Hf-H and N=C stretching modes, which come from the decomposition mechanism of β -hydride elimination(Eq.(3.1)).[148] It's obvious that the decomposition of surface adsorbed TDMAH on hydrogenated Si(100) starts at temperatures between 100 to 150°C in our measurement time range.



The adsorption and desorption behavior of TDMAH on hydrogenated Si(100) surface were also analyzed quantitatively. The change of integrated area of C-H stretching modes ($2700\sim 3000\text{ cm}^{-1}$) with time is showed in Fig.25. For both adsorption and desorption period, at different substrate temperatures, the change of C-H stretching intensity with time shows different profile. At 100°C , most TDMAH molecules are intact in the experimental time range (6 min) and the adsorption is in physisorption regime, where the molecules are trapped on the surface by weak Van der Waals force. This weak adsorption is indicated by the fast desorption (large

negative slope) behavior in the pumping mode Fig.25 (b). Noteworthy, in the adsorption mode, the curve doesn't saturate even after 6 min, which should be explained by the multilayer physisorption behavior. Adsorption at 150°C shows even sharper increase of C-H stretching signal. As seen in Fig.24, the strong decomposition signals observed at 150°C indicated presence of great amounts of decomposition products, which also include certain alkyl groups. Therefore, the sharp increasing behavior should be contributed to the accumulation of both intact TDMAH and thermal decomposition products. As one can see for the desorption profile of 150°C experiment, its desorption rate is much slower than that at 100°C. This might be because of the

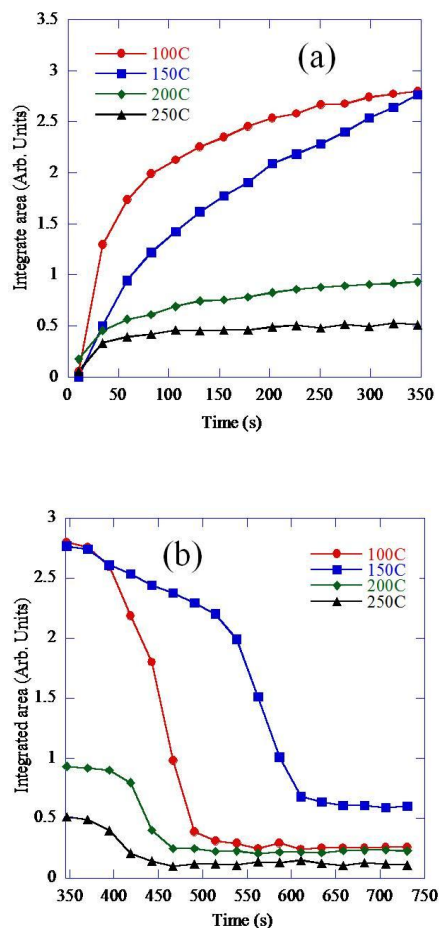


Fig. 25. Integrated C-H stretching area change with TDMAH (a) adsorption and (b) desorption time at different substrate temperatures.

slow kinetics of the desorption of the decomposition products from the surface. For practical ALD experiments at this temperature, long purging/pumping time is necessary to remove these species to minimize thin film contamination. At high temperatures (200°C and 250°C), the increased desorption rate of certain decomposition products with increasing temperature makes the adsorption behavior close to self-termination with a slight increasing trend. However, the self-terminating C-H containing adsorbates might result from a balance of TDMAH adsorption and decomposition products desorption rates and cannot represent a self-terminating thin film growth.

As mentioned earlier, the peak of 2770 cm^{-1} has been recognized as an indication of the existence of intact TDMAH molecules on the surface. This C-H stretching mode has a frequency much lower than the normal C-H stretching modes found in alkyl groups and is usually observed in transition metal alkyl amides. The ratio of this peak to the whole C-H stretching region is monitored in the adsorption/desorption period and showed in Fig.26. As one can see in this figure, in the adsorption mode, left region of the vertical blue line, the ratio of peak 2770 cm^{-1} is decreasing with increasing adsorption temperature, which indicates more TDMAH decomposition at higher deposition temperatures. In the desorption region, right of the vertical blue line, the as adsorbed species can keep in the same chemical format for certain time range and this time range is decreasing with increasing temperature, which can be explained by increased decomposition kinetics at higher temperatures. The long tail of the 150 °C desorption behavior might be attributed to the existence of large amounts of adsorbed TDMAH decomposition products. Interesting phenomenon has been observed for the 100 °C desorption, as showed in Fig.26, the desorption was composed of two steps (flat regions), which indicates

the existence of both physisorbed and small amount of chemisorbed TDMAH molecules on the surface.

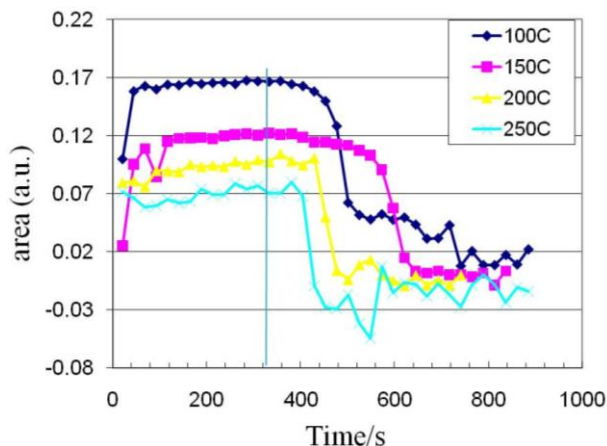


Fig. 26. Change of ratio of peak 2770 cm^{-1} to the whole C-H stretching area in the period of adsorption and desorption at different substrate temperatures.

The profile of Si-H bonds changing on the ATR silicon crystal surface in the period of TDMAH adsorption and desorption at different crystal temperatures is showed in Fig.27. As one can see, at 100°C , there is almost no change of surface Si-H bonds in the adsorption and desorption process. Starting from 150°C , the introduction of TDMAH induced apparent subtraction of surface Si-H bonds and after stopping TDMAH flow the surface Si-H bonds kept in a stable level. Sufficient thermal energy is achieved above 150°C for the reaction between TDMAH and Si-H bonds to happen. The stable Si-H bonds after TDMAH introduction indicates that the thermal energy itself can not break these bonds. The reaction of surface Si-H bonds with the thermally activated (or decomposed) TDMAH molecules is the main way for surface bonds subtraction.[149]

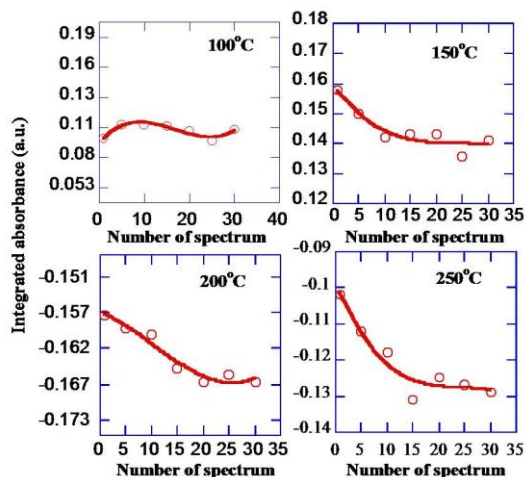


Fig. 27. Surface Si-H bonds change with TDMAH adsorption and desorption at different crystal temperatures.

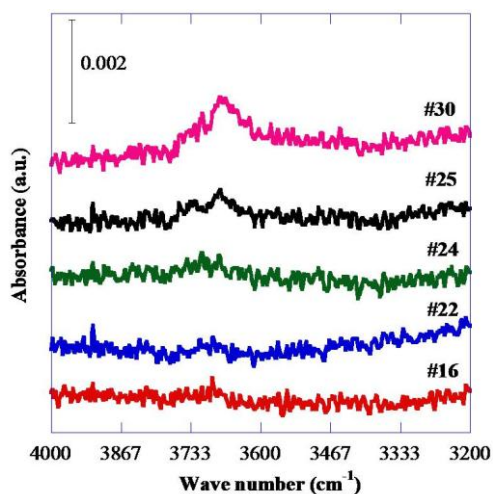


Fig. 28. Surface OH group showing up in the desorption/pumping process (150°C).

In the desorption processes for all temperatures, a peak located at $\sim 3700\text{ cm}^{-1}$ showed up after 3 to 4 min pumping. The results for the 150°C process is showed in Fig.28. This peak has been attributed to OH stretching modes from Hf-OH group, which is different from that of H₂O (broad peak at $\sim 3400\text{ cm}^{-1}$). It has been found that the reaction of TDMAH with H₂O is much thermodynamically favorable by both experimental and theoretical studies. The residual water vapor in the ATR cell (or leaks) could thus easily attack the surface adsorbed TDMAH or its

decomposition products (Hf-H) and generate Hf-OH groups on the surface. This might not be a big effect in the deposition of HfO₂, but it will be disastrous and definitely contaminate the deposition of Hf₃N₄ or HfN films.

3.3 Plasma Enhanced Atomic Layer Deposition of HfN Films

3.3.1 Introduction

HfN thin film has showed excellent properties for being used as the gate electrode material to work with HfO₂ (gate dielectric layer) in the MOSFET structure. PEALD of high quality HfN thin film at low substrate temperatures would be a greatly preferred process for practical fabrication. Previous studies on PEALD of HfN by using hafnium amides and hydrogen plasma has reported the incorporation of C elements in the as deposited thin films. However, the related thin film growth chemistry is rarely investigated. In this dissertation research, aside from the surface chemistry study of TDMAH precursor by ATR-FTIR, in-vacuo XPS is also used to study the as grown thin film surface. These work can provide a clear picture of the HfN thin film growth chemistry and its relation to thin film physical properties.

3.3.2 Experimental Details

Hafnium nitride (HfN) thin film deposition on hydrogen terminated Si(100) and thermally grown SiO₂ (on Si) substrates was carried out in a home built plasma enhanced atomic layer deposition (PEALD) system (Fig.29). This PEALD chamber is a part of a ALD/CVD thin film deposition cluster and connected to a in vacuo XPS system by vacuum gate valves, as showed in Fig.30.

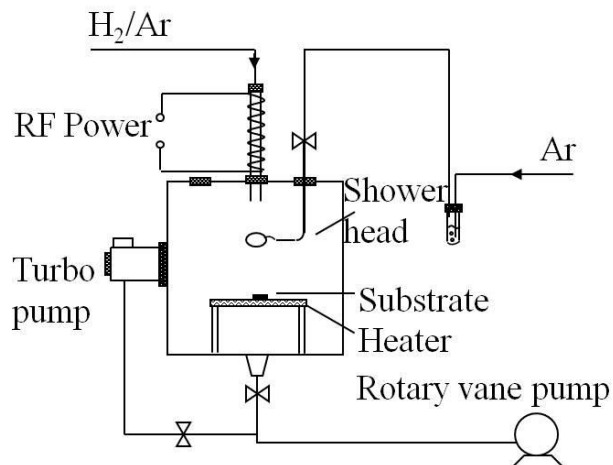


Fig. 29. Schematic of the plasma enhanced atomic layer deposition system.

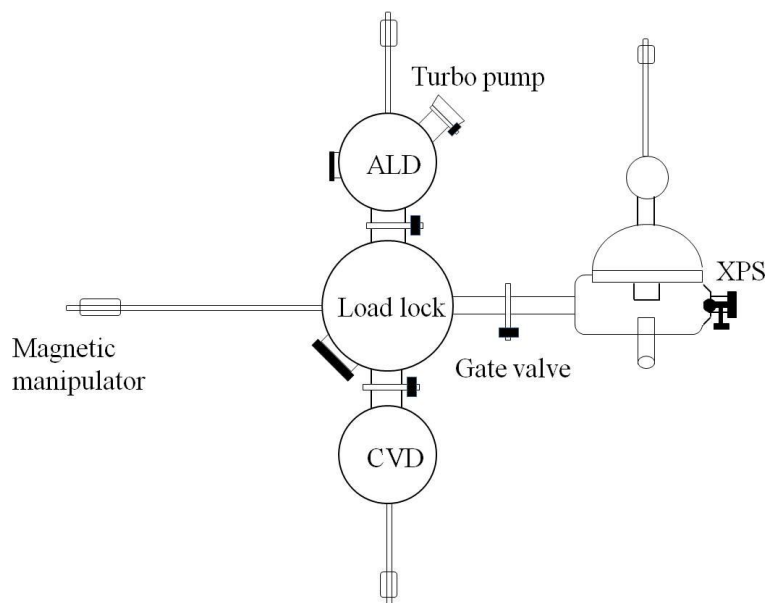


Fig. 30. ALD/CVD thin film deposition cluster coupled with in vacuo X-ray photoelectron spectroscopy.

Tetrakis (dimethylamido) hafnium ($\text{Hf}(\text{N}(\text{CH}_3)_2)_4$, 99%) purchased from STREM Chemicals Inc. was used as the metal organic precursor without any further purification. The n-type Si(100) wafer with native oxide was cleaned by standard RCA procedure and then dipped into a diluted BOE ($\text{NH}_4\text{F}:\text{HF}=10:1$) solution for 20 s to remove the surface oxide and passivate the surface with Si-H bonds. Then the Si wafer was rinsed by DI water for 10 min and blowing

dried by ultra high purity N₂ gas. The as prepared hydrogen terminated Si(100) wafer was loaded into the reaction chamber for thin film deposition or underwent further thermal oxidation in a tube furnace (Lindberg) to form a SiO₂ layer with thickness of 100 nm to 120 nm. In a typical PEALD reaction, the bubbler filled with TDMAH was heated to 60°C by an oil bath heater and the TDMAH delivery line from the bubbler to the reaction chamber was heated to around 75°C to minimize precursor vapor condensation on the tubing walls. Hydrogen gas is introduced into the reaction chamber by passing through a quartz tube where it is ionized into hydrogen plasma. As shown in Fig.29, the quartz tube is wrapped by a copper solenoid, which is connected to the RF power generator (coupled with matching network). In our case, 13.56 MHz RF power is used to generate inductively coupled plasma (ICP) in the quartz tube. Since the generation of plasma is out of the reaction zone, the effect of substrate surface bombardment by powerful ions can be minimized. The introduction of TDMAH and hydrogen plasma was separated by flowing inert gas (Ar) between them. A typical ALD cycle is composed of the following four sequential steps: 5s TDMAH vapor, 35s Ar purging, 25s hydrogen plasma, 5s Ar purging. The pulsing of the reactants and inert gas and the pulsing of the plasma are synchronized in a self written LabVIEW program (Fig.31). Through serial communication (RS232/RS485) with a PC, the RF power generator and a programmable relay controlling all the pneumatically controlled valves can be controlled simultaneously by this LabVIEW program. In this way, the plasma was turned on exactly at the time range of hydrogen pulse through the quartz tube, as shown in Fig.32.

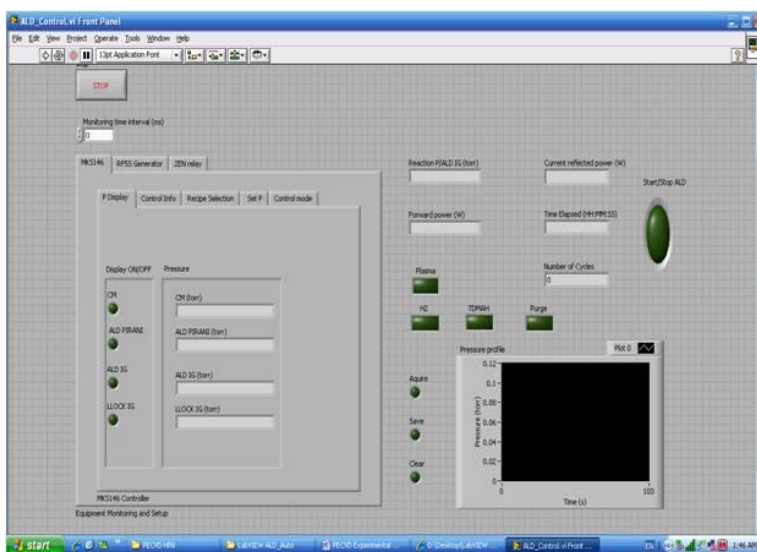


Fig. 31. LabVIEW program for the control of PEALD process.

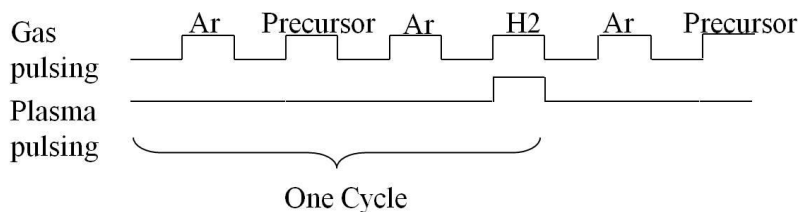


Fig. 32. Synchronized reactants and plasma pulsing sequence in PEALD experiments.

The reaction chamber is coated with Si_3N_4 (PECVD using He diluted SiH_4 and N_2 plasma) to minimize the effect of out gassing. The base pressure of the reaction chamber is pumped to around 5×10^{-8} torr by a turbo molecular pump (Pfeiffer). In the deposition process, the chamber is pumped by a rotary vane vacuum pump (Leybold) and the system pressure is automatically controlled by a MKS throttle valve.

The as deposited thin films were characterized by an in vacuo XPS system (APEX, Physical Electronics Inc.), which was connected to the deposition chamber through a gate valve, as showed in Fig.30. The vacuum pressure of sample transfer path is below 10^{-7} torr. The

pressure for XPS analysis is around 5×10^{-9} torr. The as used X-ray is Mg K_{α} (1253.6 eV) with a power of 100W (15kV). The sample analysis area is 6×6 mm². The pass energy of the electron spectrometer is set to 100 eV for survey spectra and 25 eV for high resolution spectra. Depth profile analysis was also carried out in this XPS system by using a 5kV Ar⁺ ion gun and the etching area was set to the same as the analysis area. A nominal etching rate of 1 nm/min is achieved under our experimental conditions. The thin film cross section were characterized by field emission scanning electron microscopy (JEOL 7000) and transmission electron microscopy (TECNAI F20). The FESEM was operated at accelerating voltage of 20 kV with a spot size of 8 and working distance of 10 mm. High resolution TEM picture of the thin film interface was taken under field emission gun voltage of 200 kV. Zone axis of [100] was taken for the single crystal Si substrate. Thin film surface topography was studied by atomic force microscopy (Nanoscope IV, Digital Instruments). The AFM was operated in tapping mode using AFM tips of NSC15/AIBS (MikroMasch) with tip radius of curvature of around ~ 10 nm, force constant of ~ 40 N/m and resonance frequency of ~ 325 kHz. Crystallographic information was studied by X-ray diffractometer (X'pert, Philips) and thin film thickness by X-ray reflectivity. The thin film sheet resistance was measured by a four point probe.

3.3.3 Results and Discussion

Incorporation of oxygen has been found in the PEALD deposited thin films in spite of the low system base pressure ($\sim 10^{-8}$ torr), chamber wall coating with Si₃N₄ and the pre-sputtering of substrate with hydrogen plasma. Considering the small air contamination effect for an in-vacuo XPS analysis, the oxygen has been attributed to the residual oxidants (H₂O/O₂) in the deposition ambient which can react with TDMAH and be buried into the film. One factor has been found to affect the degree of oxygen incorporation is the inert gas purging time after TDMAH pulse. By

fixing the other conditions as follows: plasma power 100W, substrate T 250°C, pressure 0.1 torr, TDMAH pulse 5 s, hydrogen plasma 25s, and the purge time after hydrogen plasma is 5s, the purging time after TDMAH pulse is adjusted. As one can see in Fig.33, with increasing purging time from 15 to 35 s the oxygen concentration in the thin film has been reduced to around 6 at%. Longer purging time than 35s doesn't have much effect and make the thin film growth even slower.

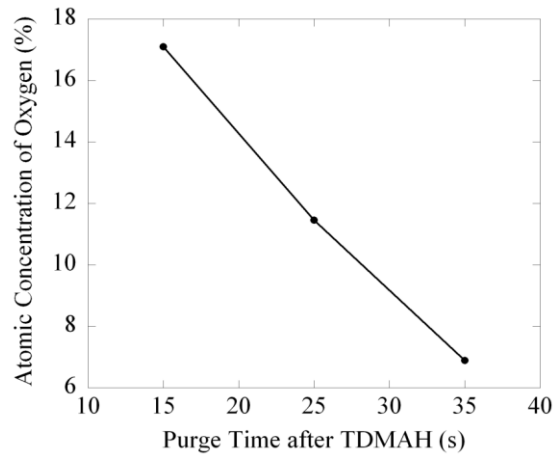


Fig. 33. The effect of purging time on oxygen incorporation.

By using this purging time, other PEALD processing conditions are studied to see their effects on thin film surface chemistry. Surface chemical compositions of thin films deposited at different temperatures, pressures and plasma powers are listed in table 2. Apart from the desired

Table 2. In vacuo XPS results of thin film surface chemical composition at different experimental conditions.

Plasma Power (W)	Substrate Temperature (°C)	Reaction Pressure (torr)	Chemical composition (atom %)			
			Hf	N	C	O
100	150	0.1	33.6 (±2.4)	36.1 (±2.7)	18.1 (±1.3)	12.1 (±1.5)
100	250	0.1	38.6 (±2.6)	39.4 (±2.3)	18.7 (±1.2)	3.3 (±1.0)
100	350	0.1	35.9 (±2.2)	37.6 (±2.4)	19.8 (±1.2)	6.6 (±0.9)
50	250	0.15	35.3 (±1.9)	39.9 (± 3.0)	20.8 (±2.0)	4.0 (±1.0)
100	250	0.15	30.7 (±2.2)	34.3 (±2.8)	27.5 (±1.4)	7.5 (±0.8)
150	250	0.15	34.6 (±2.7)	38.7 (±3.1)	17.6 (±1.8)	9.1 (±1.4)

Hf and N elements, incorporation of C and O on the thin film surface is also found. Similar results have been reported by other groups, which were attributed to contamination from sample air exposure.[71,72] This explanation is apparently unconvincing considering that the same phenomena happened in our in-vacuo XPS analysis. To better understand the chemistry happening in the ALD process, an XPS depth profile analysis was carried out using a 5kV Ar⁺ ion gun. The XPS spectra and quantitative chemical composition changing with etching depth are shown in Fig.34 and table 3, respectively.

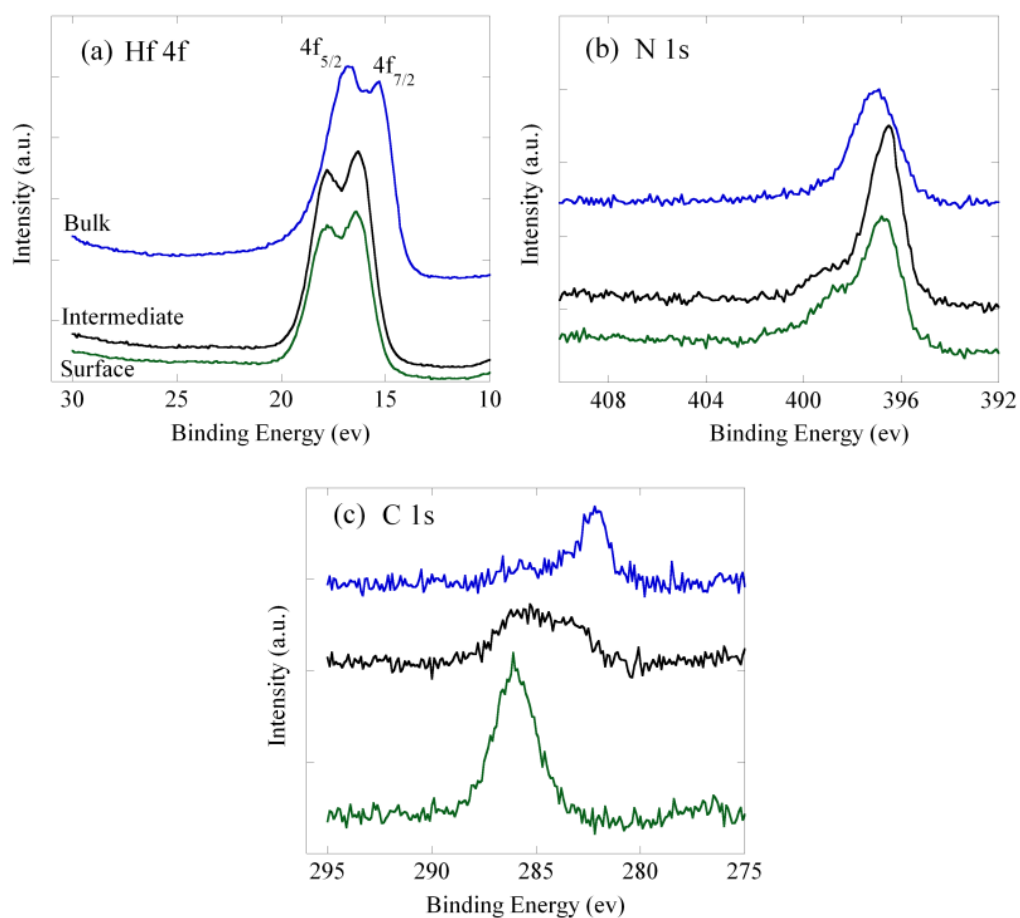


Fig. 34. XPS depth profile analysis of (a) Hf4f (b) N1s and (c) C1s in an as deposited HfN_xC_y thin film. Sample prepared at 250°C, 0.15 torr, 100W.

Table 3. Chemical composition change with depth of analysis.

	Atomic concentration (at%)			
	Hf	N	C	O
Surface	30.0	35.8	25.7	8.4
Intermediate	36.5	36.5	19.2	7.9
Bulk	49.3	31.7	14.3	4.6

In the spectra and table above, ‘surface’ means XPS analysis without any etching, ‘intermediate’ represents a very thin layer (2~3nm) measured immediately after surface etching and before the constant bulk properties, and ‘bulk’ means most of the thin film thickness where no (or very small) qualitative or quantitative chemical changes can be detected. Fig.34(c) shows a large C 1s peak from thin film surface analysis, which indicates more than 20 at% C. The position of this C 1s peak is at 286.1 eV, which is different from the C 1s signal of adventitious hydrocarbon (284.8eV). This result further rules out the possibility of air contamination. This carbon signal probably comes from the N-C bonds, which exist in complexes of TDMAH incomplete decomposition products. This assignment was supported by the existence of the left shoulder on N 1s peak in Fig.34(b), which represents N in an organic matrix. With Ar⁺ ion etching, the chemical state change of C 1s peak shows a clear trend from organic carbon (N-C, 286.1eV) to metal carbide (Hf-C, 282.3eV). Meanwhile, the peak shoulder on N 1s disappeared gradually. Although the existence of hafnium carbide phase was reported as a natural phase produced by PEALD reaction in the bulk, the possibility of chemical state change due to ion sputtering could not be ruled out. Apart from the disappearance of N-C groups due to ion etching, another obvious change is the shape and position of Hf 4f peak. The height ratio between the two spin orbit splitting peaks of Hf 4f_{5/2} and Hf4f_{7/2} increases with sputtering time until the bulk properties are obtained. It has been reported in certain XPS studies of hafnium nitride thin film that Hf4f_{5/2} has relatively stronger intensity than Hf4f_{7/2} due to the enhancement effect of N 2s.

[150,151] This is a unique feature for hafnium nitride considering that no such effect is observed in hafnium metal, hafnium carbide or hafnium oxide.[152,153] The peak shift of Hf4f_{7/2} from 16.4eV to 15.1eV also indicated the presence of hafnium nitride phase after removal of the top layers. Apparently this phase is hafnium rich due to the incorporation of C and O.

X-ray diffraction study shows that all the as deposited thin films on both Si(100) or SiO₂/Si are amorphous without any crystalline features. The only X-ray diffraction signals are from the single crystal silicon substrate. Cross sectional view by SEM and TEM and surface morphology by AFM for a multilayer sample of HfN_xC_y/SiO₂/Si prepared at 250°C and 100W are shown in Fig.35 (a), (b) and (c) respectively. The SEM image shows the clear layered structure and a dense HfN_xC_y film around 80 nm deposited on SiO₂/Si. The HRTEM image showed the interface between HfN_xC_y and that between Si and SiO₂. Clear lattice fringes from (100) planes of the Si single crystal can be observed. Selected area diffraction has proved that there is no crystalline feature for the SiO₂ and HfN_xC_y layers, as measured by XRD. The gradual contrast change in the interface indicates a gradual mass density change, which might be due to small amount of interdiffusion in a thickness range of 1~2 nm. The RMS surface roughness was measured to be 0.8nm for a scanning area of 1 μm².

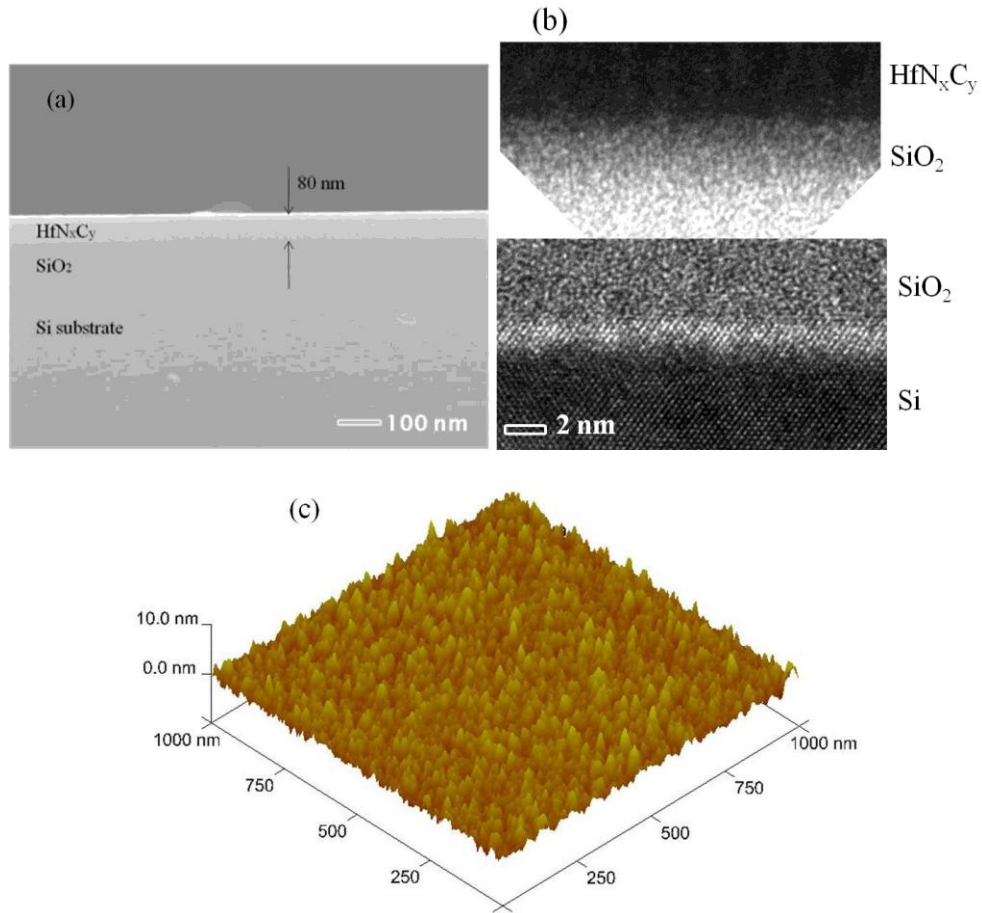


Fig. 35. (a) Cross sectional view of HfN_xC_y on SiO_2/Si (b) HRTEM images of the HfN_xC_y - SiO_2 and SiO_2 - Si interfaces (c) surface topography by AFM, RMS roughness is 0.8nm.

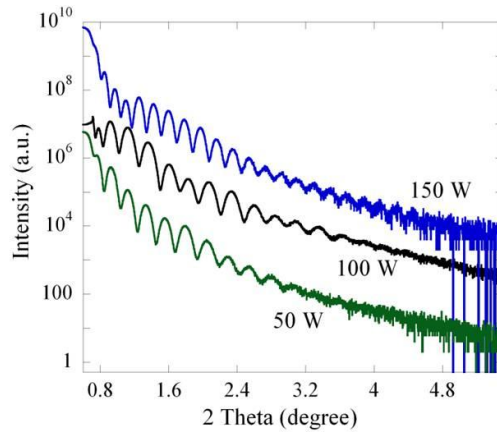


Fig. 36. X-ray reflectivity measurement of the as deposited HfN_xC_y films at different plasma powers. The ALD cycles of deposition are 200, 200, and 300 for 50W, 100W, and 150W, respectively.

X-ray reflectivity (XRR) results of the as deposited thin films under different plasma powers are showed in Fig.36. The thin film thickness is fitted by using the Philips WinGixa

software. The thickness results are very close to those obtained by cross sectional SEM measurement. Thin film roughness is in the range of few angstroms, which is indicated clearly by the long range interference patterns and coincides with the AFM measurement.

Fig.37 (a) shows the effect of plasma power on thin film growth rate and resistivity. Both the growth rate and resistivity decrease with increasing plasma power from 50W to 150W. Compared to the dramatic decrease of thin film resistivity, the growth rate change is much smoother. The growth rate around 0.18nm/cycle is reasonable for a practical ALD method, in which only a fraction of a monolayer (ML) is deposited for each cycle. The small decrease of growth rate might be explained by a plasma etching effect. Fig.37 (b) shows the effect of plasma power on the chemical states of surface Hf. The increased peak ratio of Hf 4f_{5/2} to Hf 4f_{7/2} at high plasma power indicates the formation of more hafnium nitride phase on the surface.[150,151] This result can be a good explanation of the decreased thin film resistivity at higher plasma powers.

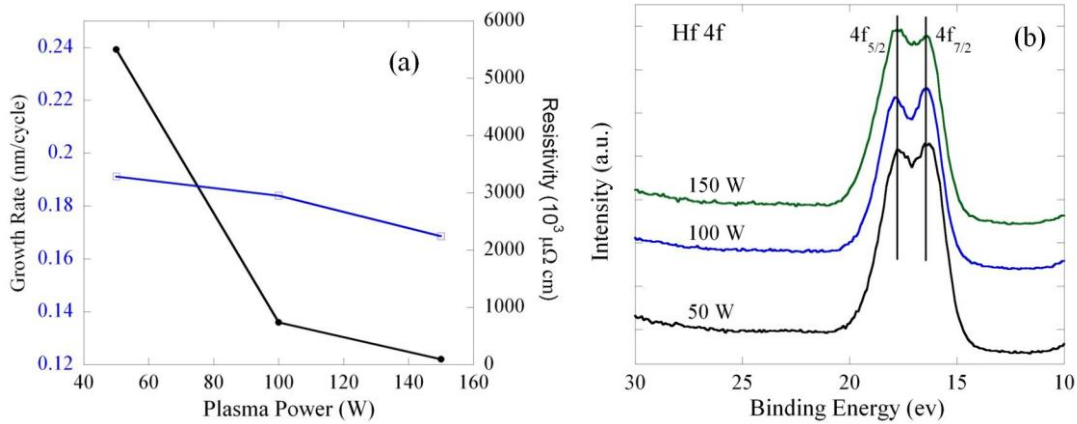


Fig. 37. (a) Plasma power effect on thin film growth rate and resistivity (b) Plasma power effect on chemical states of surface Hf.

3.4 Conclusion

In summary, TDMAH adsorption and reaction on hydrogenated Si(100) surface has been investigated by in-situ ATR-FTIR experiments. It has been found that for temperatures below 100°C, physisorption is the main mode of TDMAH adsorb onto the crystal surface and no obvious surface Si-H bonds breaking. These physisorbed TDMAH molecules can be pumped away easily. At temperatures between 100°C and 150°C, surface adsorbed TDMAH molecules start to decompose and newly emerging IR peaks at 1591 cm⁻¹ and 1639 cm⁻¹ were assigned to N=C and Hf-H vibrational mode respectively based on a β-hydride elimination mechanism. The decomposition species on the surface has been found hard to desorb at low temperatures, which can contaminate the thin film growth if the purging/pumping time is not long enough. The surface Si-H bonds subtraction has been found for adsorption above 150°C and it's closely related to the TDMAH decomposition behavior.

Hafnium nitride thin film deposition by PEALD using TDMAH and hydrogen plasma has been investigated. Uniform and moderately conductive HfN_xC_y thin films were deposited on Si(100) and SiO₂ substrates. A thin surface layer (2~3nm) containing both hafnium nitride and organic complexes of TDMAH decomposition has been found by in vacuo XPS analysis. Depth profile analysis by XPS indicated the existence of hafnium carbide phase in the bulk. Thin film resistivity is greatly affected by the level of hydrogen plasma power, in which higher plasma power results in lower thin film resistivity. In spite of this tunability of resistivity by plasma power, carbon incorporation is still a big issue for this PEALD method. Therefore, more appropriate reducing agent or nitrogen source is probably needed to get pure HfN thin film by CVD/ALD method.

CHAPTER 4. DIRECT LIQUID INJECTION CHEMICAL VAPOR DEPOSITION OF FERRIMAGNETIC NICKEL FERRITE AND LITHIUM FERRITE FILMS

4.1 Introduction

Nickel ferrite (NiFe_2O_4) and lithium ferrite (LiFe_5O_8) thin film growth by DLI-CVD technique is reported in this chapter. The achievement of both high quality and thick spinel ferrite thin film materials is particularly essential for the fundamental research of ME (magnetoelectric) effect in ferrite-ferroelectric bi-layer structures and practical application in dual tunable microwave devices.[40,41] DLI-CVD technique has the potential capability of fulfilling these requirements. To achieve these objectives, the main research work includes material selection (precursor, solvent, and substrate), processing condition optimization (vaporization and CVD process) and thin film characterization (structural, morphological, and magnetic properties). More results have been obtained for nickel ferrite thin film deposition. Effect of the CVD growth conditions on the thin film physical properties is studied. Possible reaction mechanisms and thin film growth modes have been proposed upon experimental results. Single crystal quality and thin film defects are characterized by various techniques, including XRD, polarized Raman and TEM. Great emphasis is focused on FMR properties of the as grown nickel ferrite films, which directly related to its microwave applications. Nickel ferrite thin film growth on various piezoelectric substrates are also investigated. For the lithium ferrite thin film growth, certain preliminary results have been obtained.

4.2 DLI-CVD Growth of NiFe₂O₄ Films

Nickel ferrite (NiFe₂O₄) is a well known insulating and high permeability magnetic material that is commonly used in transformer cores and microwave applications.[73] It possesses a spinel ($Fd\bar{3}m$) structure ($a = 0.834$ nm) with the tetrahedral *A* sites occupied by half of the Fe³⁺ cations, whereas the remaining Fe³⁺ and Ni²⁺ cations are distributed over the octahedral *B* sites (Fig.15). Recently, much attention has been attracted to the growth of epitaxial spinel ferrite thin films for magnetoelectric applications and monolithic microwave integrated circuits (MMIC).[43,77] For instance, the magnetoelectric effect in magnetic/ferroelectric heterostructures is promising for tunable microwave devices, such as filters and phase shifters, offering much faster tuning response and lower power consumption.[46]

As mentioned in chapter 2, a wide variety of thin film growth techniques have been developed and investigated in the past for nickel ferrite (and with divalent cation substitutions). However, the achievement of both high quality (structural, morphological, magnetic and microwave properties) and thick (1-10 micron range) epitaxial films for microwave device applications remains challenging.[73,78] Chemical Vapor Deposition (CVD) offers a number of advantages over other deposition methods, but its use for nickel ferrite film deposition has been limited by the low volatility and thermal stability of available chemical precursors. The direct liquid injection (DLI) technique, which can generate vapor from a liquid solution source at relatively low temperatures, has in recent years been successfully utilized for a number of metal-organic chemical vapor deposition processes.[110-112] DLI-CVD is a particularly useful method for multi-component systems as several precursors can be dissolved in the same solution and the relative delivery rates of precursors are defined by the solution composition. Thin film growth rate can be extremely high due to the possible high rate of precursor introduction into the thin

film growth region. The properties of the films are greatly influenced by the specific vaporization procedure, the selection of metal organic precursors, solvent and substrate material, and especially processing conditions (temperature, pressure, etc.). In this chapter, we report the epitaxial growth of relatively thick nickel ferrite films on various substrates using the DLI-CVD technique.

Various challenges for epitaxial growth of complex magnetic oxides (*e.g.*, ferrites) by CVD methods are to be expected. The first consideration is the reactivity of metal organic precursors, which has to be optimal for decomposition and film growth on the substrate surface but avoid gas phase reactions/nucleation. Moreover, the decomposition temperature ranges of the individual precursors should be sufficiently close to help retain the cation ratio of the solution source in the thin film. For growth on a lattice-matched substrate, the temperature has to be sufficiently high to provide adequate surface diffusion of the adsorbing species for epitaxial film growth and yet maintain a smooth surface morphology.

In this work, anhydrous $\text{Ni}(\text{acac})_2$ and $\text{Fe}(\text{acac})_3$ (acac is an abbreviation for acetylacetonate) in the molar ratio of 1:2 are dissolved in *N, N*-dimethyl formamide (DMF) to form the precursor solution. DMF acts as a solvent and can simultaneously minimize intermolecular association by coordinating with the metal ions.[154,155] A Brooks Instrument DLI 200 Vaporizer system is used, which vaporizes the liquids using a heated inert gas instead of a hot metallic surface. This approach enables more gentle vaporization of the solution source with minimal thermal decomposition of the precursors. MgAl_2O_4 (100) and MgO (100) substrates with cubic normal spinel ($a = 0.808$ nm) and fcc ($2a = 0.842$ nm) structure, respectively, are used for systematic study of film growth due to their close lattice match with nickel ferrite (lattice mismatch of 3% and 1%, respectively).[81,101,102] Deposition on other

substrates such as MgO(111), and piezoelectric SrTiO₃(100), PMN-PT (Pb(Mg_{1/3}Nb_{2/3})O₃-PbTiO₃) (100), and PZN-PT (Pb(Zn_{1/3}Nb_{2/3})O₃-PbTiO₃) (100) is also investigated under certain experimental conditions.

4.2.1 Experimental Details

Nickel ferrite films are deposited on MgAl₂O₄ (100) and MgO (100) substrates in a horizontal 1.5 inch diameter quartz tube furnace. The DLI-CVD experimental set-up is shown in Fig.38.

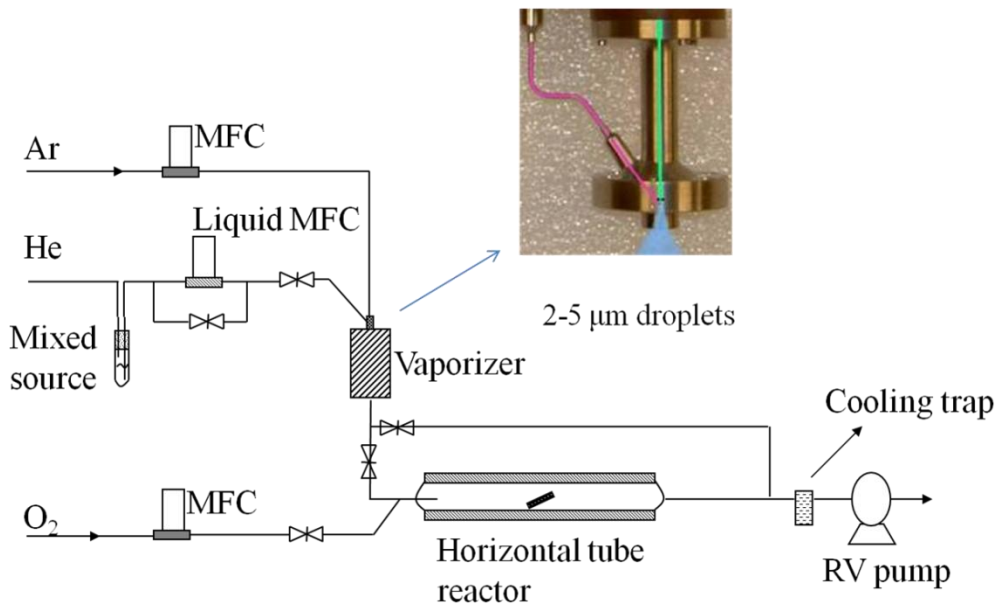


Fig. 38. Experimental set-up of DLI-CVD system for the growth of nickel ferrite films.

As shown in Fig.38, The CVD reactor is a three zone low pressure quartz tube furnace. The tube reactor, with a diameter of 1.5 in. and length of 50 in., was pumped down to the reaction pressure (12 Torr) by a rotary vane vacuum pump (Leybold, Trivac). Ni (acac)₂ (98%) and Fe(acac)₃ (99%), bought from Sigma-Aldrich, were used as metal organic precursors without any further purification. These precursors were dissolved in N, N-dimethyl formamide (DMF) in a molar ratio of 1:2 as the source for liquid injection. Ultrahigh purity He (20 psi) was used to pressurize the liquid flow from solution container to the vaporizer. The flow rate of the liquid

solution was accurately controlled by a Brooks Quantim liquid MFC (10 g/h, full range) connected to the DLI200 vaporizer system. Ultrahigh purity argon gas was used as the carrier gas, which served both as the vaporization medium and the delivery gas. The liquid vaporization process is accelerated by a sequential input of mechanical and thermal energy. At the vaporizer inlet, where the liquid and carrier gas flow intersect, is an atomizer, which breaks up the entering fluid into fine droplets (2~5 μ m) because of a large pressure drop. Efficient heat and mass transport between the fine droplets and the preheated carrier gas (Ar) results in the metal-organic precursors being homogeneously entrained in the solvent vapor and carried into the reactor without premature decomposition. Ultrahigh purity oxygen was used as the oxidant. Atomically polished single crystals such as MgAl₂O₄ (100) and MgO (100) of dimensions 5mm×5mm×0.5mm from CrysTec GmbH were used as substrates. Before loading into the reactor, the substrates were ultrasonically cleaned sequentially in acetone and isopropanol and then blow dried with N₂. The vaporizer system was cleaned with pure DMF solvent after each run. Typical processing conditions are summarized in Table 4.

Table 4. Typical processing conditions for DLI CVD of epitaxial NiFe₂O₄ films.

Substrate	MgAl ₂ O ₄ (100) / MgO (100)
Reaction pressure (Torr)	12
Growth temperature (°C)	500-800
Concentration of solution (Fe(acac) ₃ , mol/L)	0.067
Solution flow rate (g/hr)	6
Ar carrier gas flow rate (sccm)	300
Vaporizer temperature (°C)	175
Oxygen flow rate (sccm)	300

Prior to investigation of the CVD process conditions, we optimized the vaporizer operation parameters (including precursor solution injection rate, carrier gas (Argon) flow rate, vaporizer temperature, inlet and outlet pressures) by inspecting the surface morphology and

chemical composition of nickel ferrite film grown at 600°C. As a starting point, we chose the vaporizer temperature based on the thermal properties of the solvent and precursors (b.p. of DMF 153°C, m.p. of Ni(acac)₂ 230°C, m.p. of Fe(acac)₃ 184°C). Other physical properties of the solvent (*e.g.*, density, viscosity and heat of vaporization) are also important in choosing the carrier gas and liquid flow rates, and vaporizer pressure. All the vaporizer parameters have to be tuned for optimal flow of the precursors into the CVD reactor without decomposition. Deviations from the optimized parameters, such as in the vaporizer temperature or liquid flow rate, results in a rough film surface and/or changes in stoichiometry from the desired composition. This can be attributed to an inadequate vaporization process due to precursor(s) decomposition, condensation on tubing walls, or the presence of insufficiently vaporized droplets/clusters. In this paper, if not specified, all the vaporizer operations are fixed at these optimized values (Table 4).

The film morphology was characterized by both FE-SEM (JEOL-7000) and AFM (Veeco Nanoscope-IV). The JEOL-7000 FE-SEM system was also equipped with an EDX (Oxford Instruments) measurement system for chemical composition analysis. For the FE-SEM and EDX characterization, operating conditions were as follows: accelerating voltage 20 KV, beam spot size 8, and working distance 10 mm. All the samples were attached to the sample holder by carbon tape and no metallic coatings on the sample surfaces were deposited. For the AFM characterization, ultra sharp non-contact silicon cantilevers (MikroMasch, NSC15/AIBS) with a typical probe tip radius of ~10nm and resonant frequency of ~325 kHz were used in tapping mode. Transmission electron microscopy was used to characterize the crystal structure and defects. XRD (Philips X'pert Pro) was used to investigate crystallographic properties of the as-deposited films. Cu K α radiation was used as the X-ray source. All the samples were characterized under similar experimental conditions (with a nickel filter and 0.5° divergence slit

size). For the rocking curve analysis, 2θ was fixed at the NiFe_2O_4 (400) diffraction angle while scanning ω . The Raman spectra of NiFe_2O_4 single crystal and $\text{NiFe}_2\text{O}_4/\text{MAO}$ films were measured under nominally identical conditions using a T64000 (Jobin Yvon) spectrometer equipped with a microscope and a liquid nitrogen cooled CCD detector. The 633 nm laser line of a He-Ne laser was used for excitation. The magnetic properties were studied using an AGM (PMC, Micromag-2900) system with a magnetic field scan to 16 kOe. The four edges and backside of each sample were polished by sandpaper before the AGM measurements.

4.2.2 Results and Discussion

4.2.2.1 Thin Film Growth on MgAl_2O_4 (100) and MgO (100)

4.2.2.1.1 Oxygen Effect on Film Morphology

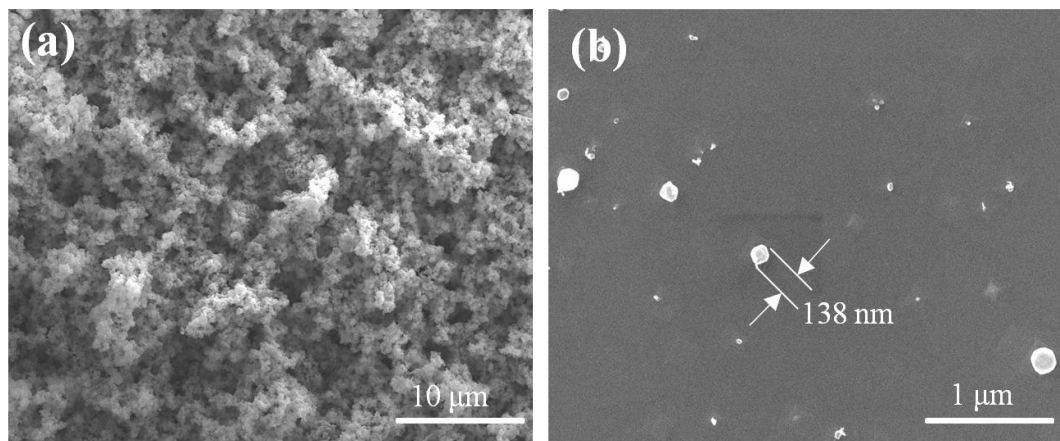


Fig. 39. The effect of oxygen flow rate on thin film surface morphology observed using field emission scanning electron microscopy. (a) Without oxygen flow, film of porous structure is formed; (b) particulates formation under high oxygen flow rate.

Unlike typical CVD reactions where metal-organic precursors are the only reactant species, DLI-CVD involves the combustion of a large concentration of organic solvent vapor. In our case, the consumption of oxygen by DMF (flash point 58°C) has to be considered. To investigate the effect of oxygen flow on the thin film growth, we carried out two control

experiments at a deposition temperature of 700°C on both MgAl₂O₄ (100) and MgO (100) substrates. The first experiment involves film growth without any oxygen flow (just the argon carrier gas). Film growth by thermal decomposition of the metal chelate precursors occurs in the absence of oxygen.[108] However, as can be seen from the SEM micrograph image in Fig.39 (a), the as-deposited film shows a very porous structure. EDX (Energy Dispersive X-ray Spectroscopy) analysis reveals the presence of a significant excess of Fe than in stoichiometric nickel ferrite, along with trace amounts of carbon (< 2%). The porous structure is likely related to incomplete decomposition together with the slow kinetics of the surface reaction and/or desorption of the by-products. Based on thermal stability studies of the precursors, the preferential incorporation of iron may be attributed to the lower thermal stability of Fe(acac)₃ than Ni(acac)₂. [156-158] The effect of high oxygen flow rate, double of what is needed for growth of smooth and stoichiometric films (Table 4), is studied in the second control experiment. As shown in Fig.39(b), a relatively smooth and dense film is obtained. The correct chemical composition (Ni:Fe = 1:2) is obtained under this condition. However, small particles (10-100 nm range) are observed on the film surface. The particulate formation can be attributed to gas phase nucleation, which is a common and undesirable feature in CVD reactions, especially at high reaction pressures. Particulates buried in the film during growth can result in crystalline defects and thus influence the physical properties. It is noteworthy that the film growth rate does not increase with the increased oxygen flow rate. Comparing the results of these two experiments, the oxygen flow influences the thin film growth kinetics and helps balance the deposition rates of Ni and Fe. It is likely that more of lower molecular weight volatile products, such as CO₂, are generated in the presence of oxygen and thus minimize the problem of blocked surface adsorption sites. Based on mass spectrometry studies Igumenov *et al.* [159] suggest that the

oxygen does not participate in the formation of the oxide phase during thermal decomposition of metal β -diketonates. Instead, its role is primarily to oxidize the organic fragments to form smaller molecular weight products and thus avoid carbon incorporation in the film. This is consistent with our observations from the above control experiments. Earlier mass spectrometry studies have shown that thermal decomposition of Ni(acac)₂ results in the formation of methane in addition to acetone and carbon dioxide formed with Fe(acac)₃. [156] In the presence of oxygen, the preferential consumption of methane can drive the reaction equilibrium towards thermal decomposition and thus increase the rate of Ni incorporation into the film. Moreover, enhanced surface reaction kinetics in the presence of oxygen can alter the film growth mode to a mass transfer limited process where the incorporation rate of Ni and Fe is actually dependent on their diffusion rates through the gas-phase boundary layer above the surface as discussed later.

4.2.2.1.2 Thin Film Growth Mode

Table 5. Characteristics of nickel ferrite films deposited at different substrate temperatures.

Substrate temperature (°C)	Growth rate (μm/hr)		RMS roughness (nm)		Ni:Fe atomic ratio	
	MgAl ₂ O ₄	MgO	MgAl ₂ O ₄	MgO	MgAl ₂ O ₄	MgO
500	0.65	1.10	0.17	30.0	1:2.02	1:2.06
600	0.75	0.64	0.23	0.14	1:2.09	1:2.10
700	0.62	0.56	0.34	0.16	1:2.08	1:2.09
800	0.68	0.80	18.8	22.0	1:2.01	1:1.99

We have grown nickel ferrite films on MgAl₂O₄ (100) and MgO (100) at temperatures ranging from 500°C to 800°C under optimized vaporization conditions and oxygen flow rate. The corresponding film growth rates, surface roughness (RMS), and chemical compositions are listed in Table 5. The film growth rate does not show a clear trend with increasing temperature.

However, there is sizeable run-to-run growth rate variation for films grown at a specific temperature, particularly at higher deposition temperatures (up to 8%). The growth rate is sensitive to the position of the substrate in the reaction zone. This is likely related to the temperature and precursor concentration distribution in our hot wall tube reactor, which can be approximated by a plug flow reactor (PFR). From the vaporizer gas outlet to the substrate surface, the tube temperature gradually increases to the reaction zone temperature due to thermal conductance while the precursor concentration decreases because of thermal decomposition and deposition on the surrounding tube wall. The highest growth rate can be achieved over a particular region of the reactor because of a favorable combination of temperature and precursor concentration. By inspecting the color of the tube walls after each experiment, we found that most of the deposition occurs in a small volume (tube length of ~2 inch) close to the entrance of the reaction zone.

To better understand the effect of precursor concentration in the solvent on the film growth rate, both half and double of the original concentration of the precursor solution (listed in Table 4) were employed for growth at a substrate temperature of 600°C, with all the other process conditions held constant. The film growth increases almost linearly with increasing concentration (0.39, 0.75, and 1.42 $\mu\text{m/hr}$ respectively). The film deposited with lower concentration of precursors does not show any obvious change in surface roughness and chemical composition. However, the enhanced growth rate obtained for deposition with the higher concentration is compromised by increased surface roughness and an Fe rich stoichiometry. From a mass-transfer limited assumption, it is possible that the increased concentrations of Ni and Fe species in the hydrodynamic boundary layer affect their relative diffusion rates,[85] however, mass transfer limitations are not easily determined in this set-up

because vapor velocity cannot be changed independent of pressure. Further insight is gained by the importance of substrate position and tilt on thickness uniformity, and the relatively weak temperature dependence of growth rate which suggest mass-transfer limited deposition. In either the mass transfer or reaction limited scenario, film growth rate is dominated by the precursor concentration distribution, and thus the consumption of precursors by deposition on the tube wall is a primary reason for the variability in film growth rate. In spite of these growth rate variations, the chemical composition and surface morphology are well reproduced from run-to-run for different deposition temperatures.

EDX analysis indicates chemically pure NiFe_2O_4 films without any detectable contamination. The ratio of nickel to iron, as shown in Table 5, is close to stoichiometric for different deposition temperatures. The film surface roughness has been characterized by cross-sectional Scanning Electron Microscopy (SEM) and Atomic Force Microscopy (AFM), and show different trends for depositions on MgAl_2O_4 and MgO substrates. These trends can be observed in Fig.40(a) and (b), which show the cross-sectional view of nickel ferrite films deposited at different temperatures on both substrates. At 600°C and 700°C , films grown on both MgAl_2O_4 and MgO exhibit an atomically smooth surface. Fig.40(c) shows the cross-section SEM view of a $0.78\ \mu\text{m}$ thick NiFe_2O_4 film on MgAl_2O_4 substrate deposited at 600°C . The inset is a $5\ \mu\text{m} \times 5\ \mu\text{m}$ AFM image of the surface of the same sample, exhibiting a RMS roughness of $\sim 0.3\ \text{nm}$. In our experiments, smooth ($\text{RMS} < 0.5\ \text{nm}$) and dense (without voids or detectable grain structure) films are formed for samples deposited between 600°C and 700°C on both MgAl_2O_4 and MgO substrates. However, films thicker than $0.5\ \mu\text{m}$ on MgO display surface cracks. This is probably due to the large interfacial tensile stress resulting from a combination of lattice mismatch ($2a_{\text{MgO}} = 0.842\ \text{nm}$, $a_{\text{NiFe}_2\text{O}_4} = 0.834\ \text{nm}$) and thermal expansion difference

($\alpha_{\text{MgO}} = 1.0 \times 10^{-5} \text{ K}^{-1}$, $\alpha_{\text{NiFe}_2\text{O}_4} = 1.34 \times 10^{-5} \text{ K}^{-1}$). A detailed analysis of stress development between nickel ferrite film and MgO substrate during CVD growth has been reported by Fitzgerald *et al.*[82] Careful examination of the surface cracks in our films with FE-SEM (Field Emission Scanning Electron Microscopy) interestingly reveals bent fractured rectangular lamina pointing out of the surface consisting of both the nickel ferrite film and a layer of the MgO substrate. The MgO layer thickness is about the same of that of the nickel ferrite film. It appears that the residual interfacial stress is sufficiently large to fracture the MgO crystal but not the interfacial bond between the film and MgO. Apart from the extremely large tensile stress build-up, it is speculated that the crystalline defects generated by the Mg diffusion into nickel ferrite films can also weaken the strength of MgO crystal. Surface cracks in nickel ferrite films on MgO (100) substrate have previously been observed in films grown using pulsed laser deposition,[101] but no details are provided regarding their formation mechanism.

As can be seen in Fig.40(a) and (b), films grown on both MgAl_2O_4 and MgO exhibit increased surface roughness of ~ 20 nm for the highest deposition temperature of 800°C . No surface cracks are observed on MgO substrate for this deposition temperature probably due to relaxation of the interfacial stress by the increased roughness. As for the low temperature deposition at 500°C , growth on the two substrates shows completely different morphology. Nickel ferrite films on MgAl_2O_4 display similar morphology as those deposited at 600 and 700°C , but films on MgO show voided columnar structure (Fig.40(d)), as expected for low temperature epitaxial growth due to limited surface diffusion. Apparently, for nickel ferrite growth at 500°C , the MgAl_2O_4 (100) surface provides larger surface diffusivity than the MgO (100) surface.

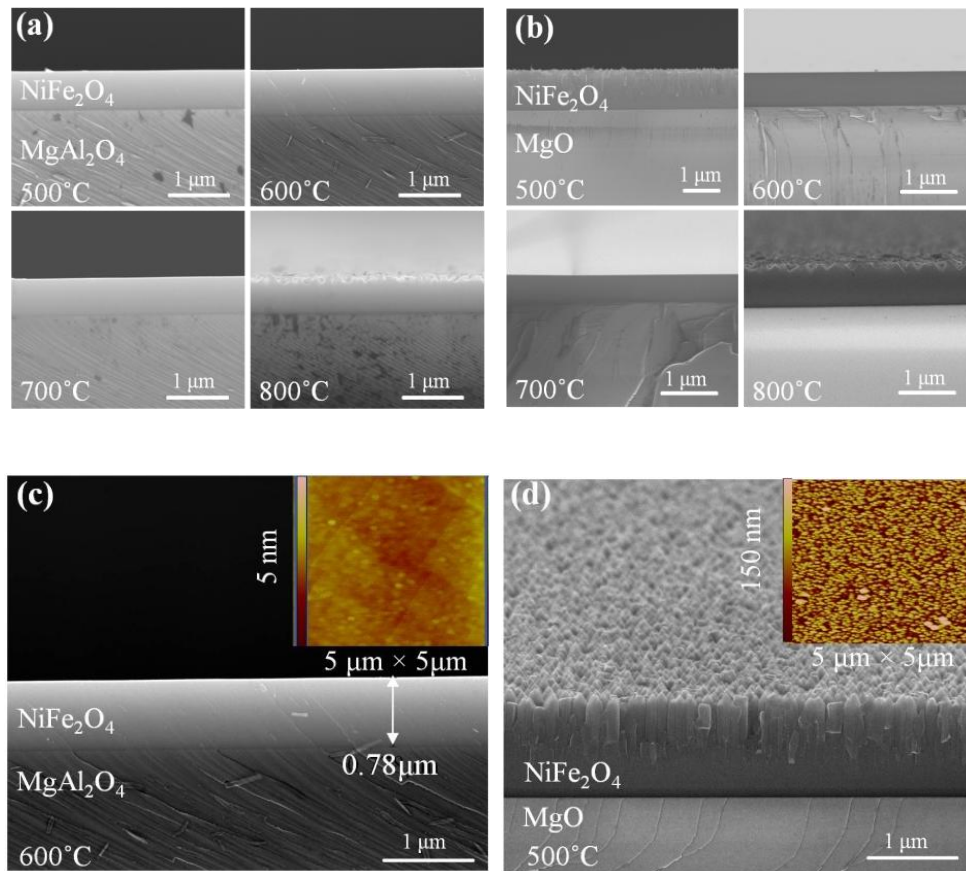


Fig. 40. Cross-sectional view by field emission scanning electron microscopy; (a) nickel ferrite on MgAl₂O₄(100) deposited at 500~800°C; (b) nickel ferrite on MgO(100) deposited at 500~800°C; (c) Magnified view of nickel ferrite on MgAl₂O₄ deposited at 600°C, the 5 × 5 μm² AFM image shows the film surface RMS roughness of ~0.3 nm; (d) Magnified and tilted (10°) view of nickel ferrite on MgO(100) deposited at 500°C with RMS roughness of ~30 nm.

4.2.2.1.3 Physical properties

Due to the formation of surface cracks in films on MgO (100) substrates that complicate analysis of film properties, we focus here on results for growth on MgAl₂O₄ (100) substrates. The crystalline structure of the as-deposited films has been analyzed using an X-ray diffractometer (Philips X'pert Pro, Cu Kα source). As shown in Fig.41, all the films deposited between 500°C to 800°C exhibit a pure spinel phase with the (*h*00) planes parallel to the film surface. The calculated out-of-plane lattice parameters are 0.833, 0.834, 0.834, and 0.831 nm for films grown at 500, 600, 700 and 800°C, respectively. The films grown at 500-700°C have lattice

parameters close to that of the bulk (0.834 nm). This is not surprising considering that the films are relatively thick ($> 0.5 \mu\text{m}$) and completely relaxed, despite the lattice mismatch with the substrate ($\sim 3\%$). However, the out-of-plane lattice parameter of the film grown at 800°C is lower than that in the bulk, which indicates the presence of a tensile stress. A stress model for heteroepitaxial magnetic oxide films has been proposed by Besser *et al.*[160] Depending on the film thickness, the lattice mismatch between the overgrowing film and substrate at the growth temperature cannot withstand the elastic deformation and the stress will be relieved by formation of misfit dislocations at the interface. In this case, assuming elastic behavior for the film, the residual stress after cooling the sample to room temperature is proportional to the difference in the thermal expansion coefficient between the film and substrate and is not related to the bulk lattice parameters. The residual tensile stress of films deposited at 800°C can be explained well by this model considering that NiFe_2O_4 has a larger thermal expansion coefficient than MgAl_2O_4 ($\alpha_{\text{MgAl}_2\text{O}_4} = 9.5 \times 10^{-6} \text{ K}^{-1}$).

Rocking curve (ω -scan) analysis of NiFe_2O_4 (400) diffraction is used to characterize the degree of film texture (Fig.42(a)). The measured FWHM (Full Width at Half Maximum) decreases from 0.47° to 0.23° with increasing growth temperature (FWHM value of MgAl_2O_4 substrate is $\sim 0.02^\circ$). A similar trend in the FWHM has been observed in PLD grown NiFe_2O_4 films on MgAl_2O_4 substrates.[102] For films grown on MgO substrates, the FWHM is significantly lower (*e.g.*, 0.03° for film grown at 600°C), likely because of the closer lattice match than MgAl_2O_4 . We have examined the in-plane texture from ϕ scans of the NiFe_2O_4 {220} planes. Fig. 42(b) shows the ϕ scan results of both the NiFe_2O_4 film and MgAl_2O_4 substrate (deposited at 600°C). The four 90° spaced diffraction peaks clearly illustrate the four-fold symmetry of the spinel structure. The coincidence of these four peaks with the {220} peaks from

the MgAl_2O_4 substrate confirms cube-on-cube epitaxial growth. The ϕ scan FWHM values are 0.99° and 0.06° for the NiFe_2O_4 film and the MgAl_2O_4 substrate, respectively.

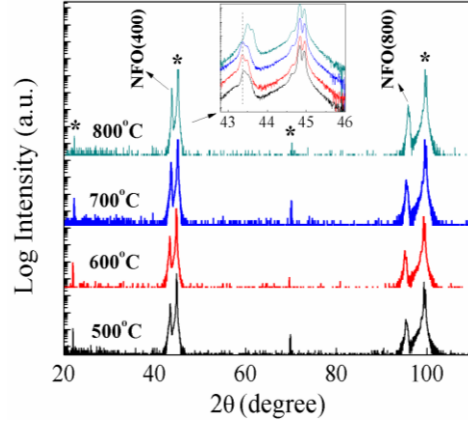


Fig. 41. XRD patterns for NiFe_2O_4 films deposited on MgAl_2O_4 (100) at 500, 600, 700 and 800°C. Peaks with (*) symbol are from MgAl_2O_4 ($h00$).

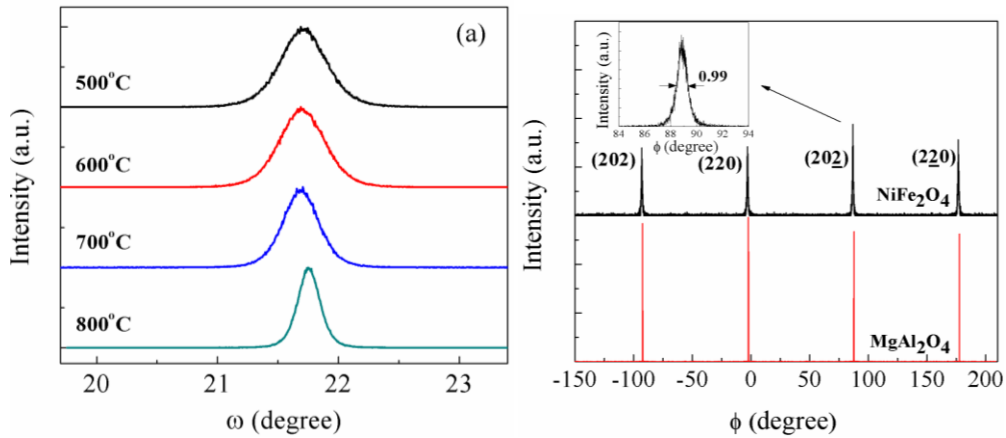


Fig. 42. (a) Rocking curves of NiFe_2O_4 (400) diffraction from films deposited at different temperatures. The FWHM are 0.47, 0.46, 0.36 and 0.23 for the 500, 600, 700 and 800°C deposited samples, respectively. (b) ϕ scan for the $\{220\}$ diffractions of both NiFe_2O_4 film and MgAl_2O_4 (100) substrate (deposited at 600°C).

Epitaxial film growth has been further confirmed using polarized Raman spectroscopy measurements. The comparison of the polarized Raman spectra of NiFe_2O_4 films growth at three different temperatures on MgAl_2O_4 substrate with those of a bulk NiFe_2O_4 single crystal is shown in Fig.43. The first and second letters in the notations XX, XY, X'X', and X'Y' indicate the polarization of the incident and scattered light, respectively, along the pseudo cubic X \parallel [100],

Y \parallel [010], X' \parallel [110], or Y'' \parallel [-110] directions. These spectra provide further evidence that the films are epitaxial and of single crystal quality. Indeed, except for negligible differences in the peak positions and relative intensities, the corresponding spectra of the films and the crystal are practically identical. It is worth mentioning here that the number of Raman lines and their polarization properties differs significantly from what is expected for the $Fd\bar{3}m$ structure. According to recent reports,[161,162] this is explained by the fact that at a microscopic level Ni $^{2+}$ and Fe $^{3+}$ are not randomly distributed, but ordered at the octahedral sites.

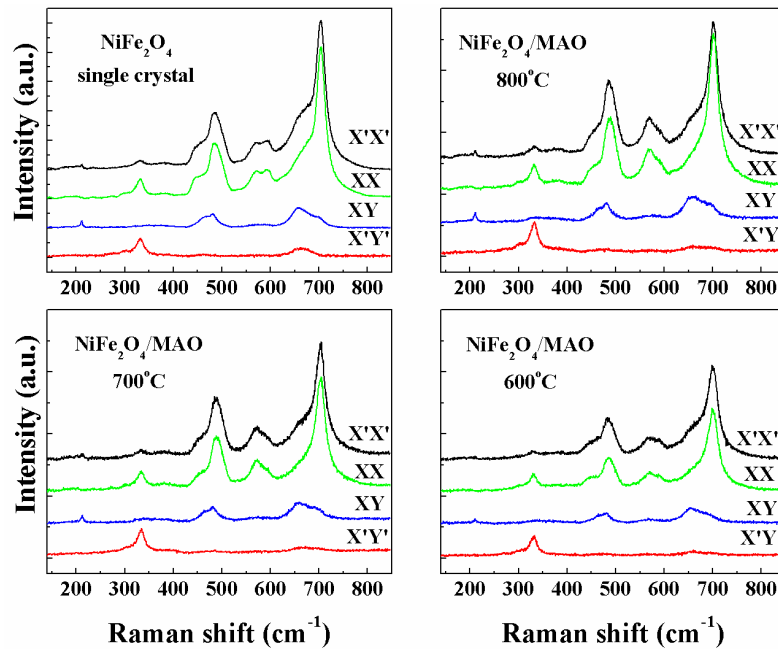
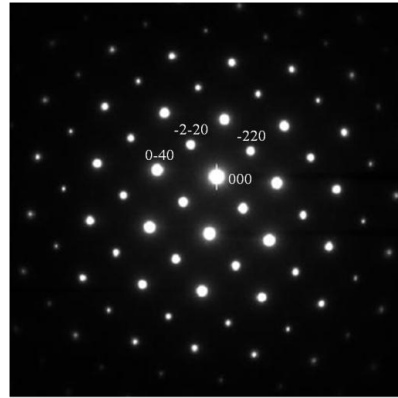


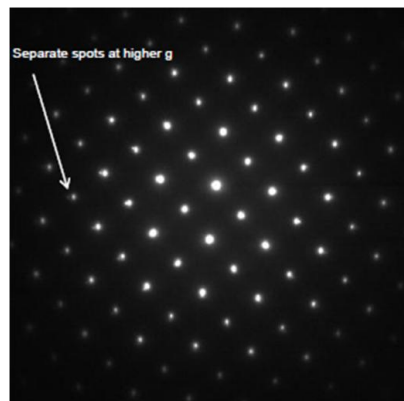
Fig. 43. Polarized Raman spectra of NiFe $_2$ O $_4$ single crystal and NiFe $_2$ O $_4$ films on MgAl $_2$ O $_4$ substrate obtained at room temperature with 633 nm excitation with various exact scattering configurations. Courtesy of Dr. M. N. Iliev from University of Houston for taking the Raman data.

Transmission electron microscopy is used to analyze the as deposited nickel ferrite films on MgAl $_2$ O $_4$ (100) substrate. Electron diffraction patterns for the films deposited at 600°C is showed in Fig.44. The diffraction pattern is taken along the zone axis $\langle 001 \rangle$ and spots from various lattice planes of spinel nickel ferrite film have been indexed in Fig.44(a). The four fold symmetry single crystal structure has been clearly demonstrated by the as shown diffraction

pattern. Fig.44(b) has diffraction spots from both the film and the MgAl_2O_4 substrate. For lattice planes with small miller indices the spots from the film and the substrate overlap with each other, while for those with larger indices the separation of two spots can be observed.



(a)



(b)

Fig. 44. Electron diffraction pattern of nickel ferrite film grown on MgAl_2O_4 substrate at 600°C . (a) diffraction pattern from the nickel ferrite film only; (b) diffraction pattern from both the film and the substrate. Zone axis of $\langle 001 \rangle$ was selected for both diffraction patterns. Courtesy of Dr. R Datta for taking the electron diffraction data.

Diffraction contrast TEM images of the sample mentioned above under two beam conditions have been obtained and are showed in Fig.45. The sample was tilted to make $(-1-10)$ the strongest diffraction spot. In this bright field TEM image, certain threading dislocations can be clearly observed. These defects are probably from the strain relaxation process with thin film growth. As we have found in the XRD measurement that the nickel ferrite films are fully relaxed under these experimental conditions. HRTEM image of the interface between nickel ferrite and

MgAl₂O₄ substrate is showed in Fig.46. Lattice fringes could be clearly seen from both {220} and {040} planes. The dark area might be from antiphase boundaries as has been reported by R. Datta, et. al..[163] The area in the red box of Fig.46(a) is Fourier filtered to exhibit the diffraction information only from the {040} planes. Break of periodicities has been found and marked with red circles in Fig.46(b). The lattice mismatch and difference of thermal expansion coefficients could both contribute to the presence of irregular lattice planes at the interface of thin film growth.

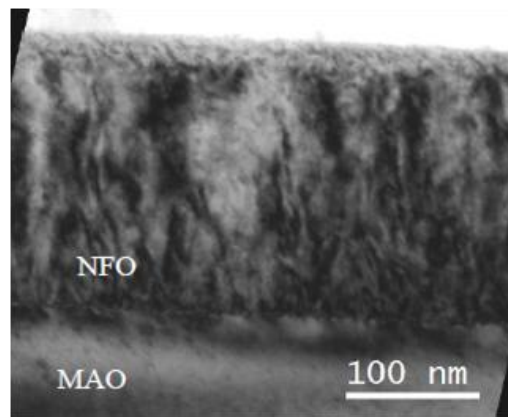


Fig. 45. Bright field TEM image of nickel ferrite on MgAl₂O₄ deposited under 600°C. The image is taken under two beam conditions with $g = \langle -1-10 \rangle$. Courtesy of Dr. R Datta for taking the TEM image.

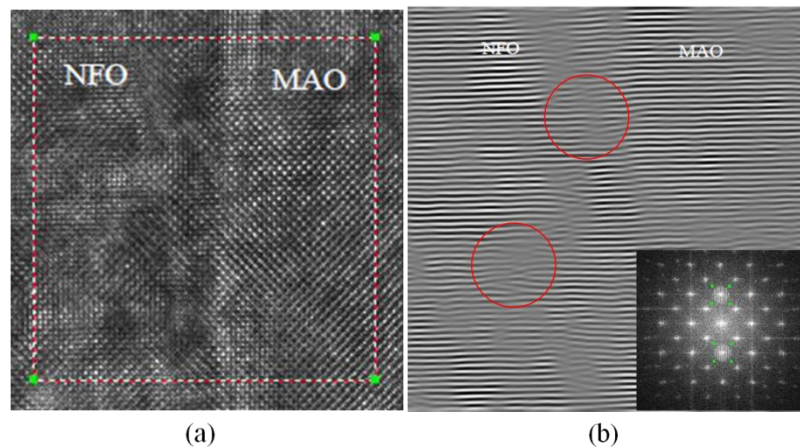


Fig. 46. (a) HRTEM image of the interface between nickel ferrite film and MgAl₂O₄ substrate; (b) Fourier transform of the area in the red box of the HRTEM image, the as left lattice fringes are from {040} planes. Courtesy of Dr. R Datta for taking the HRTEM images.

We have used an AGM (Alternating Gradient Magnetometer) to measure the room temperature magnetic properties of the as-deposited films on MgAl_2O_4 substrate. The saturation magnetization values are 257, 261, 284 and 299 emu/cm^3 for films grown at 500, 600, 700 and 800°C, respectively. In spite of the increased surface roughness of the sample grown at 800°C, its saturation magnetization value is very close to the bulk value of 300 emu/cm^3 . This may be attributed to the increased degree of texture with increasing deposition temperature, as indicated by the results of the ω scan. Fig.47 shows the hysteresis loops of samples deposited at 500°C and 800°C, with an increase in saturation moment observed for the film grown at the higher temperature.

Variations in the values of the saturation magnetization and coercivity versus deposition temperature are plotted as insets in Fig.47. While the saturation moment increases steadily with increasing deposition temperature to approach the bulk value, the film coercivity initially increases and then decreases with increasing deposition temperature. Various factors can contribute to the change of coercivity, such as stoichiometry deviation, cation ordering, strain and grain size. Among these, grain boundaries can act as pinning sites for magnetic domain

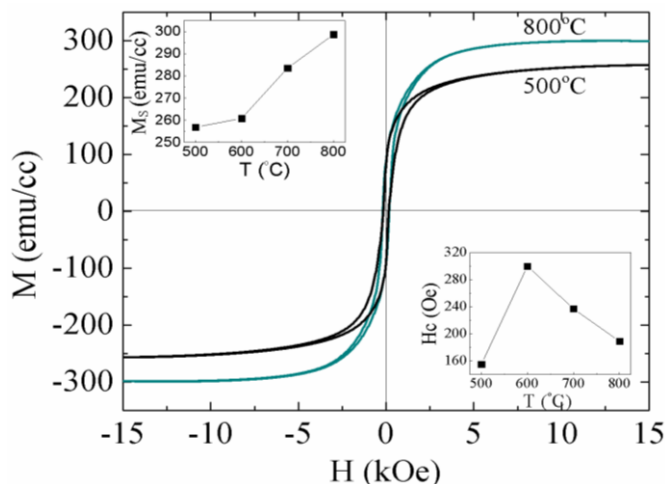


Fig. 47. AGM hysteresis loops for nickel ferrite films deposited at 500°C and 800°C. The upper-left inset shows the dependence of the saturation magnetization on deposition temperature; the lower-right inset shows the dependence of the coercivity on deposition temperature.

walls. In the multi-domain regime, small grain size and large wall density can result in large coercivity.[164,165] It is likely that the increase in grain size with increased deposition temperature from 600°C and 800°C results in films of decreasing coercivity. However, the decreased coercivity for the 500°C sample may have a different origin, including possible changes in cation ordering at low deposition temperatures.[101]

The as deposited nickel ferrite films on MgAl₂O₄ (100) under different temperatures are characterized by a coplanar waveguide (CPW) FMR system (400 MHz~40 GHz). The FMR resonance conditions under different microwave frequencies and crystal orientations (to the static magnetic field) are measured first. The results for the 600°C deposited sample is showed in Fig.48. As one can see, the linear dependence of the resonance frequency on resonance field for different crystal orientations, which indicates the excitation of the uniform FMR mode.[166] The shift between lines is due to the change of effective internal field, which can be contributed by demagnetizing field, magnetocrystalline anisotropy or strain effect. The theoretical modeling of resonance conditions for spinel ferrite in thin film format have been proposed by using the equation of motion of magnetization (eq.1.14) and assuming effective demagnetizing fields. The

as derived equations for different crystal orientations (to the static magnetic field) are showed below.[167] In these equations, ω is the microwave frequency in rad/s, γ is the gyromagnetic ratio, H is the static magnetic field, K_1 is the first order magnetocrystalline anisotropy coefficient, M_s is the saturation magnetization, and T_1 is a term representing strain effect. Noteworthy, the demagnetizing factors in the film plane are assumed to be zero and the strain in the film plane is assumed to be isotropic here. Based on these equations, the FMR experimental data for thin film deposited at different temperatures are fitted using multi-linear regression method.

$$\left(\frac{\omega_{100}}{\gamma}\right)^2 = \left(H_{100} + \frac{2K_1}{M_s}\right) \left(H_{100} + \frac{2K_1}{M_s} + 4\pi M_s + T_1\right), \quad (4.1)$$

$$\left(\frac{\omega_{110}}{\gamma}\right)^2 = \left(H_{110} - \frac{2K_1}{M_s}\right) \left(H_{110} + \frac{K_1}{M_s} + 4\pi M_s + T_1\right), \quad (4.2)$$

$$\frac{\omega_{001}}{\gamma} = H_{001} + \frac{2K_1}{M_s} - 4\pi M_s - T_1. \quad (4.3)$$

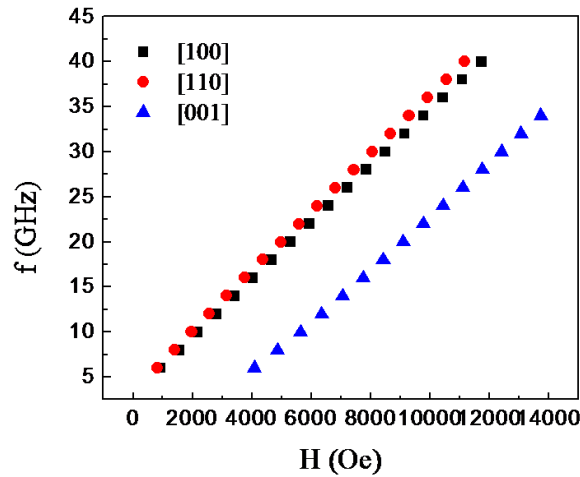


Fig. 48. FMR resonance field under different microwave frequencies and crystal orientations as measured for the nickel ferrite sample deposited at 600°C. (sample size 5 mm × 5 mm, thickness ~780 nm).

The FMR fitting results are showed in table 6. Also showed in this table are the in plane and out-of-plane lattice parameters calculated from the Cohen's method (eq.1.13) and the M_s values measured by AGM. As can be seen in the table, the change of in plane and out-of-plane lattice constants for the 800°C sample is the largest and make the crystal unit cell a slightly

tetragonal shape, which indicates the existence of large tensile stress thin the film. This apparent strain phenomenon will affect the internal magnetic field and thus change the resonance field. The much smaller T_1 term of 800 °C than those of other temperatures coincides with this strain effect very well. Another behavior is the increasing magnetocrystalline anisotropy field ($\frac{2K_1}{M_s}$) with increasing deposition temperature, which might be attributed to the increased single crystal quality of the as deposited thin films. The as listed spectroscopic splitting g factor (also known as Landé g factor) has a relationship with the gyromagnetic ratio: $\gamma = \frac{g\mu_B}{\hbar}$, in which μ_B and \hbar are Bohr magneton and reduced Planck constant, respectively. The values of as calculated g factor are slightly greater than 2, which has been also reported for experimental measurement of other ferrite materials.[168]

Table 6. Structural and magnetic properties of nickel ferrite films deposited at different temperatures.

Structural and magnetic parameters	Growth temperature (°C)			
	500	600	700	800
In-plane lattice parameter a (Å)	8.354±0.002	8.346±0.002	8.348±0.003	8.366±0.001
Out-of-plane lattice parameter c (Å)	8.338±0.001	8.343±0.001	8.342±0.001	8.318±0.001
Saturation magnetization $4\pi M_s$ (G)	3230	3280	3569	3757
g factor	2.24±0.003	2.27±0.01	2.28±0.009	2.28±0.03
$2K_1/M_s$ (G)	-75±15	-228±46	-272±38	-328±111
$4\pi M_{\text{eff}}$ (G)	2348±14	2560±46	2883±38	889±108

The line width of FMR resonance curve represents the degree of microwave loss which is an important concern for practical microwave device application. Nickel ferrite films deposited on MgAl_2O_4 at different temperatures were characterized by in plane FMR (static magnetic field pointing at [100] direction) at microwave frequency of 9.5 GHz. The as measured thin film thickness is in the range of (650~780 nm). As one can see in Fig.49, the FMR line width of film

deposited at 600°C is the lowest. One important factor contributing to single crystal thin film FMR line width is the surface roughness. This is probably the reason why films deposited at higher temperatures show larger FMR linewidth. Another possible reason is interface diffusion of Mg element from the substrate to the film at higher temperatures. Effect of chemical impurities on FMR line width of ferrite materials has been widely investigated.[169,170] It's noteworthy that the increased single crystal quality at higher temperatures is compromised by the decreased FMR performance. Thin film deposited at 500°C also shows larger FMR line width than that of 600°C. This might be attributed to the low single crystal quality and different ion distribution in nickel ferrite lattice structure resulted from limited surface diffusion behavior at low temperatures.

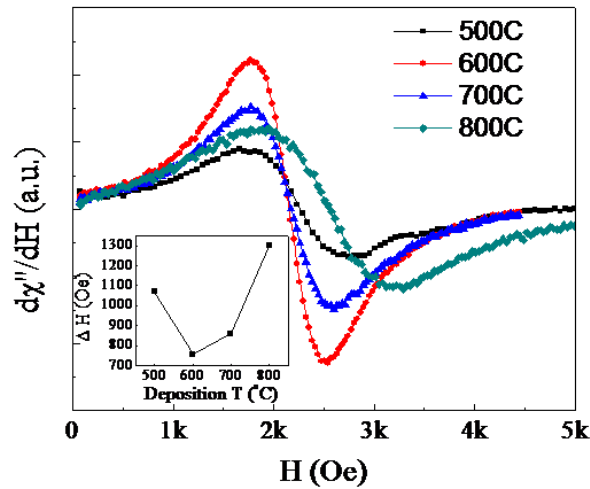


Fig. 49. Ferromagnetic resonance curve of nickel ferrite films deposited on $MgAl_2O_4$ substrate at different growth temperatures. (Sample size 5 mm × 5 mm, thickness 650~780 nm) The inset shows the profile of FMR line width with thin film growth temperature.

Due to the smallest FMR line width of films deposited at 600°C, angle and frequency dependence FMR behavior of film deposited at this temperature is characterized. The angle dependence of in plane FMR line width measured at 9.5 GHz shows four-fold symmetry (Fig.50), which coincides with the cubic structure of nickel ferrite as measured by XRD ϕ scan. In this

measurement, 0 degree represents the static magnetic field pointing at the [100] direction of the single crystal. The in-plane cubic anisotropy can be clearly observed by the shift of the resonance field at different orientations with the easier axis pointing at [110] direction. This is reasonable considering that the easy axis is in the [111] direction in a bulk nickel ferrite single crystal.

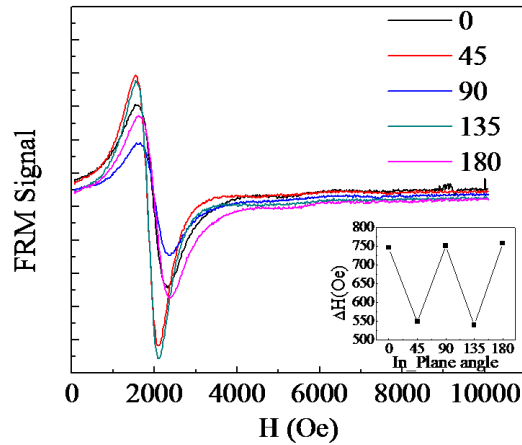


Fig. 50. In plane FMR curves measured at different angles of the sample to the static magnetic field. The inset shows the line width value vs. in plane angle.

The in plane and out-of-plane FMR curves are showed in Fig.51. As can be seen, both the resonance field and the FMR line width have a big difference between the in plane and out-of-plane measurement. The shift of the resonance field to a much higher position for the out-of-plane measurement indicates the presence of a large magnetic anisotropy with easy axis parallel to the thin film surface. The decreasing FMR line width from 752 to 160 Oe can be attributed to the decreased two magnon scattering effect for the out-of-plane measurement.[171] It has been proved that the coupling effect between the uniform FMR mode and degenerate spin waves is angle dependent for thin film materials. More specifically, when the magnetic field is parallel to the thin film surface, there are a large number of spin wave states which are degenerate with the uniform mode and a significant contribution to the two magnon scattering line width is possible. When the magnetic field is perpendicular to the thin film surface, there are essentially no spin

wave states degenerate with the FMR frequency and there should be almost no two magnon scattering contribution to the line width. This out-of-plane value of FMR line width for nickel ferrite film is the lowest compared to those have been reported previously. The best value has been reported so far is for annealed nickel ferrite film deposited by PLD method, which is ~330 Oe.[101] However, this line width is still larger than the bulk value (40~80 Oe).[170] Possible reasons include valence exchange effect and slowly relaxing mechanism, both of which are related to chemical impurities. The valence exchange effect results from the existence of small amount of Fe^{2+} cations in the lattice structure, which can induce channel for electron hopping between Fe^{2+} and Fe^{3+} sites. Slowly relaxing impurities could be from trace amount of metal cations from the precursors.[30]

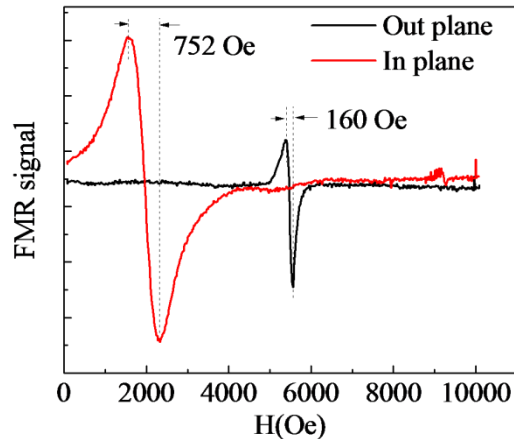


Fig. 51. In-plane and out-of-plane FMR curves of nickel ferrite film deposited on MgAl_2O_4 at 600°C .

4.2.2.2 Thin Film Growth on $\text{MgO}(111)$, $\text{STO}(100)$, $\text{PMN-PT}(100)$ and $\text{PZN-PT}(100)$

Nickel ferrite thin film growth on various other substrates than MgAl_2O_4 (100) and $\text{MgO}(100)$ are also investigated. Epitaxial growth of nickel ferrite on $\text{MgO}(111)$ has been found in the temperature range of 500°C to 800°C , as shown in Fig.52. Only diffraction peaks from (111) orientation can be observed and the diffraction intensity increase with increasing

deposition temperature. High resolution XRD measurement has showed that the as deposited thin films have out-of-plane lattice parameters slightly smaller than the bulk value, which indicates the existence of tensile stress in the thin films. This tensile stress is much smaller than those from films grown on MgO (100) substrates and therefore no surface cracking has been observed for films as thick as 1 micron. ω -scan and ϕ -scan have been carried out to characterize the out-of-plane and in plane texture of the as deposited thin films. The FWHM values of the ω -scan of thin films deposited at different temperatures are in the range of 0.6 to 0.7 and show decreasing trend with increasing deposition temperature. Fig.53 shows the ϕ -scan result of nickel ferrite thin film deposited on MgO(111) at 700°C. The {400} and {200} planes of the nickel ferrite film and the MgO substrate were scanned in plane. The three 120° separated peaks indicate the three-fold symmetry of the (111) orientation and the match between those from film and substrate represents the epitaxial growth.

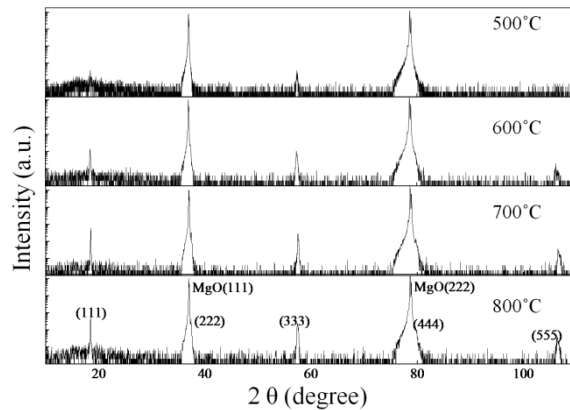


Fig. 52. X-ray diffraction θ - 2θ scan of nickel ferrite films grown on MgO(111) substrate at different temperatures.

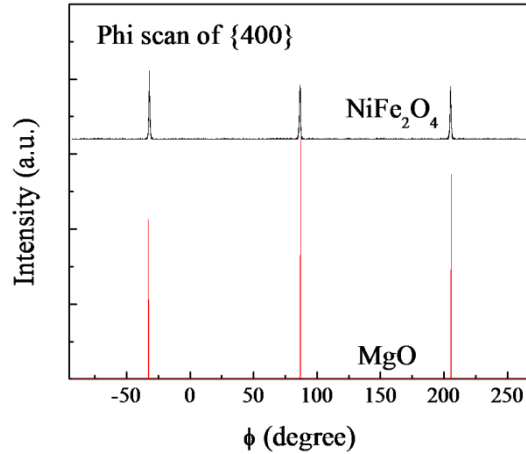


Fig. 53. ϕ -scan of nickel ferrite film grown on MgO(111) at 700°C. {400} and {200} planes from the film and substrate were scanned respectively.

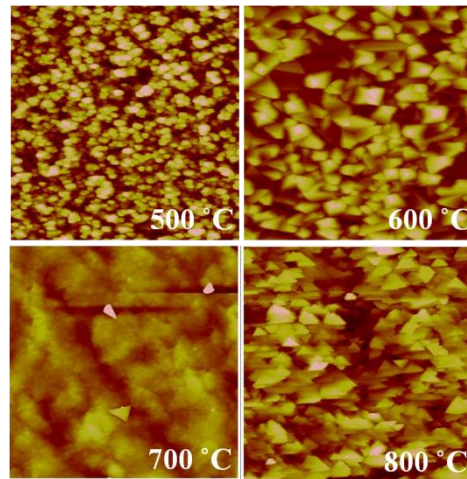


Fig. 54. Atomic force microscopy images of nickel ferrite films grown on MgO(111) substrate at different temperatures. All the images were scanned in a range of 5 μm by 5 μm . The RMS roughness for films deposited at 500°C, 600°C, 700°C and 800°C are 27 nm, 89 nm, 2.7 nm and 3.5 nm respectively.

Fig.54 showed the surface topography of nickel ferrite films deposited on MgO(111) at different temperatures by AFM. As can be seen, the best surface roughness is achieved at the temperature of 700°C, which is different from the results of deposition on MgAl₂O₄ (100) and MgO(100). This can be attributed to the difference of both surface energy and surface diffusion behavior of different substrates. Magnetic and microwave properties of the as deposited thin films are also measured by VSM and FMR respectively. The saturation magnetization (M_s) values of these films are in the range of 250~300 emu/cc. Different from those deposited on

MgAl₂O₄, the M_s value decrease with increasing deposition temperature, which might result from interface diffusion of Mg elements at high temperatures. The in plane FMR line width of these films range from 900 to 1100 Oe showing decreasing trend with increasing temperature. The improved surface roughness at high temperatures might contribute to the smaller FMR line width. Annealing of these as deposited films at 1000°C in air for certain time range (2 and 4 hrs) has also been carried out to monitor the FMR line width change. All the films after annealing show increased FMR line width, which is different from those reported results of PLD deposited nickel ferrite films on MgO(111) substrate.[101]

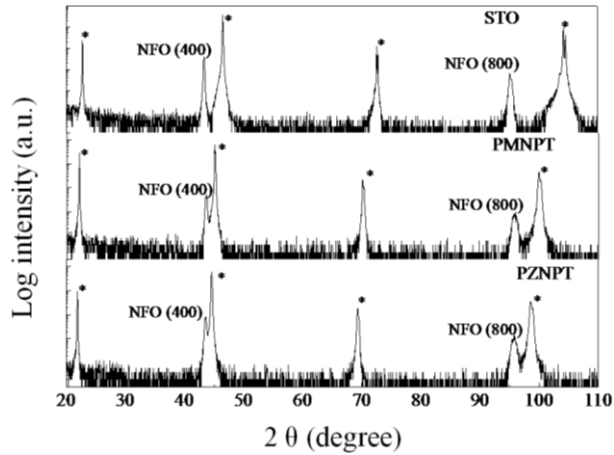


Fig. 55. Epitaxial growth of nickel ferrite films on SrTiO₃ (100), PMN-PT (100) and PZN-PT(100) substrates at 600°C measured by XRD θ -2 θ scan. Peaks with * are from (*h*00) reflections of the underlying substrates.

Nickel ferrite thin film growth on piezoelectric (ferroelectric) substrates SrTiO₃ (100), PMN-PT (100) and PZN-PT (100) are also investigated. All of these materials have a perovskite structure with lattice constants of 3.905, 4.023, and 4.06 (for ideal cubic phase). The corresponding lattice mismatch of nickel ferrite to these substrates are 6.4%, 3.5% and 2.5%, respectively. DLICVD of nickel ferrite on these substrates have been carried out at 600°C. Epitaxial growth of nickel ferrite films has been observed, as shown in Fig.55. Film growth rate around 700 nm/hr is achieved by using the same vaporizer conditions as deposition on MgAl₂O₄.

Surface roughness characterized by AFM showed much smoother growth on SrTiO₃ (~1 nm) than those on PMN-PT and PZNPT (~20 nm). Considering the similar atomic flat substrate surface and film thickness, these difference of film surface roughness should be attributed to different thin film growth mode due to different substrate surface energies. In-plane FMR measurement (9.5 GHz) of nickel ferrite films deposited on these piezoelectric substrates show FMR line width in the range of 800 to 1000 Oe. While the out-of-plane FMR curves are greatly distorted, which indicates more defects/inhomogeneities in the as deposited thin films.

4.3 DLI-CVD Growth of LiFe₅O₈ Films

Lithium ferrite has the same inverse spinel structure as nickel ferrite, but it possesses a much narrower FMR line width, which indicates very small microwave loss behavior. So far, most of the reported lithium ferrite thin film deposition are based on physical vapor deposition methods or liquid phase epitaxy.[89,93] No reports has been found by using metal organic chemical vapor deposition technique. Our research on DLI-CVD of lithium ferrite films is novel and can contribute to the understanding of thin film growth mechanism and proper processing conditions.

In our research, Li(acac) and Fe(acac)₃ are used as the metal organic precursors, both of which are dissolved in DMF solvent in a molar ratio of 1:5. Typical vaporization and processing conditions are listed in table 7. Most of the conditions are the same as those used for deposition of nickel ferrite except for the concentration of the precursor solution. Thin film deposition on MgAl₂O₄ (100) and MgO (100) are investigated in the temperature range of 500°C to 800°C. The results of XRD characterization of as deposited films are showed in Fig.56. The results indicate that epitaxial growth of lithium ferrite on MgO (100) can be obtained at all of the four temperatures. Only (*h00*) reflections from lithium ferrite have been observed. As showed in

Fig.56(a), the (400) reflection peaks from lithium ferrite show doublet due to nonmonochromatic X-ray (Cu $K_{\alpha 1}$ and Cu $K_{\alpha 2}$). With increasing deposition temperature, the peak shifts to lower 2θ angles, which indicates an increasing out-of-plane lattice constant. The dashed line in the plot marks where the bulk crystal value is. These results illustrate that with increasing deposition temperature the stress in the as deposited films changes from tensile to compressive. This phenomenon is resulted from both the effect of lattice mismatch and difference of thermal expansion coefficient. Different from growth on MgO, films grown on $MgAl_2O_4$ do not show any crystalline features at 500°C and 600°C as shown in Fig.56 (b). This is probably because of the larger lattice mismatch between lithium ferrite and $MgAl_2O_4$. At higher temperatures, 700°C and 800°C, weak diffraction peaks can be observed. However, peaks other than the epitaxial orientation ($h00$) are also found in the deposition at 800°C.

Table 7. Typical vaporization and processing conditions for DLI CVD of epitaxial $LiFe_5O_8$ films.

Substrate	$MgAl_2O_4$ (100) / MgO (100)
Reaction pressure (Torr)	10
Growth temperature (°C)	500-800
Concentration (Fe(acac) ₃ , mol/L)	0.084
Concentration (Li(acac), mol/L)	0.0168
Solution flow rate (g/hr)	6
Ar carrier gas flow rate (sccm)	300
Vaporizer temperature (°C)	175
Oxygen flow rate (sccm)	300

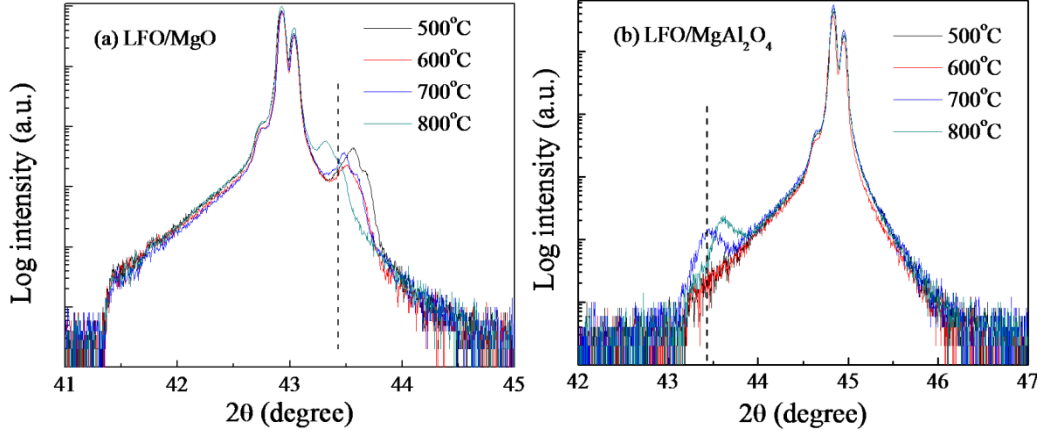


Fig. 56. X-ray diffraction θ - 2θ characterization of lithium ferrite films deposited on (a) MgO (100) and (b) MgAl₂O₄ (100) substrate at different temperatures.

Surface morphology of the as deposited films on both substrates at different temperatures are characterized by AFM. Films grown on MgO(100) show smooth surface with RMS values around 1~2 nm. However, slight surface cracking is found for the films deposited at 500°C, which possess a relatively large tensile stress. It has been reported that CVD grown complex oxide films likely exhibit surface cracking/crazing phenomenon when grown with a tensile stress.[160] Films grown on MgAl₂O₄(100) show much larger surface roughness (~30 nm) and there is no obvious temperature dependence. This result is quite different from the nickel ferrite thin film growth, which is not so sensitive to the under lying substrate.

Due to the poor crystallinity and surface roughness, films grown on MgAl₂O₄ show extremely low magnetic moment and wide and weak FMR curves. While films grown on MgO(100) exhibit much better magnetic and microwave properties of lithium ferrite and are introduced below. FMR measurement is sensitive to surface and bulk defects/inhomogeneities of the thin film as introduced previously. In our work, only films deposited at 600°C show symmetric FMR curves and give the narrowest line width, as shown in Fig.57. As one can see in this figure, the in plane FMR line width at 9.5 GHz is 368 Oe, which is much smaller than the

value of nickel ferrite films we have achieved. However, this value is still much larger than that of the bulk crystal of lithium ferrite (< 10 Oe). Crystal defects and chemical inhomogeneities can be the main reason for this large line width. Out-of-plane FMR measurement at the same microwave frequency instead show very weak FMR signal and greatly distorted FMR curve, which also indicates the presence of crystal defects or chemical inhomogeneities.

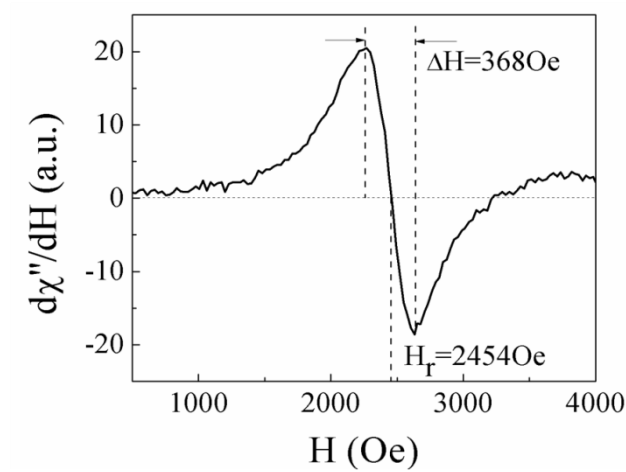


Fig. 57. In plane FMR measurement of lithium ferrite film grown on MgO(100) substrate at 600°C . (The microwave frequency is 9.5 GHz, the sample size is 5 mm by 5 mm and film thickness is ~ 550 nm).

The saturation magnetization (M_s) of lithium ferrite films deposited on MgO(100) shows increasing trend with increasing deposition temperature. This can be attributed to the increased crystal quality of the films grown at higher temperatures. Similar to nickel ferrite films, FWHM of the ω -scan decrease with increasing deposition temperature, which illustrates the increasing single crystal quality. The M_s value for films deposited at 600°C is around 200 emu/cc, which is much lower than the bulk value (350 emu/cc). The achievement of high M_s value has to be compromised by a wider FMR line width.

4.4 Conclusion

In summary, we have used direct liquid injection-chemical vapor deposition (DLI-CVD) for the growth of high quality epitaxial NiFe_2O_4 films on MgAl_2O_4 (100), MgO (100) and few piezoelectric substrates. Anhydrous $\text{Ni}(\text{acac})_2$ and $\text{Fe}(\text{acac})_3$ precursor sources are dissolved in DMF and vaporized under optimum conditions to generate stoichiometric concentration of the cations in the gas phase for the CVD reaction. Appropriate oxygen flow with the precursors is important both for improving the film morphology and also to obtain stoichiometric deposition. Under our experimental conditions, film growth rate has been found in the range of 0.6-1.1 $\mu\text{m/hr}$ and can be further increased by increasing the solution concentration or liquid flow rate. However, the vaporizer process condition and the oxygen flow rate also need to be adjusted to maintain the desired film morphology and stoichiometry. Under optimized vaporization conditions, the film morphology is dependent on the deposition temperature because of changes in the surface diffusion behavior. In the temperature range of 600°C to 700°C , relatively thick epitaxial NiFe_2O_4 films, which are extremely smooth and exhibit excellent magnetic properties, have been deposited on both MgAl_2O_4 (100) and MgO (100) substrates. However, macroscopic cracks develop on MgO after deposition and cool down, likely because of high residual tensile stress. The increased saturation magnetization with increasing deposition temperature can be attributed to improved crystalline quality, which is verified from X-ray diffraction and polarized Raman measurements. The difference between in plane and out-of-plane FMR line width measured at 9.5 GHz indicates the presence of two magnon scattering effect which is related to crystal defects or chemical inhomogeneities in the films. FMR line width as low as ~ 160 Oe has been achieved for out-of-plane measurement of nickel ferrite films deposited at 600°C , which is quite close to the value of bulk crystal.

DLI-CVD growth of lithium ferrite is investigated by using Li(acac) and Fe(acac)₃ as the metal organic precursors. Different from the deposition of nickel ferrite, lithium ferrite films grown on MgAl₂O₄(100) are much rougher and do not show any crystalline features for deposition at 500°C and 600°C. Spinel crystalline phases have been found for the deposition at 700°C and 800°C. However, more than one orientation are present for deposition at 800°C. Comparatively, lithium ferrite films deposited on MgO(100) exhibits single crystal quality and much smoother surface for the deposition temperature range of 500°C to 800°C. The smaller lattice mismatch between MgO and Nickel ferrite can be the principal reason. The narrowest in plane FMR line width ~368 Oe has been found for the films deposited at 600°C. With suitable optimization of the vaporization and film deposition conditions, excellent quality ferrite films can be grown at a relatively high rate using DLI-CVD.

CHAPTER 5. DIRECT LIQUID INJECTION CHEMICAL VAPOR DEPOSITION OF FERROELECTRIC BARIUM TITANATE FILMS

5.1 Introduction

As previously introduced, barium titanate (BaTiO_3) possesses excellent properties (high dielectric constants, ferroelectric, optoelectronic, etc.) for application in certain advanced electronic devices, and great efforts have been dedicated to the deposition of high quality single crystal barium titanate thin films in the past decades.[113-115] Among these studies, chemical vapor deposition is uniquely preferred due to its capability of large area and conformal deposition. One challenge for CVD growth of barium titanate thin film is the availability of volatile and thermally stable barium precursor. The use of metal organic β -diketonate barium precursor $\text{Ba}(\text{thd})_2$ {bis(2,2,6,6-tetramethyl-3,5-heptanedionato) barium (II)} has been widely studied in CVD method, but the high temperature ($\sim 250^\circ\text{C}$) needed to vaporize the solid precursor would result in precursor degradation (sintering effect) and thus affect run to run repeatability.[135,138,139] Besides, the precise control of rate of introduction of barium precursor into the reaction chamber is almost impossible. In this chapter, DLICVD technique as used in the deposition of nickel ferrite is used for deposition of barium titanate films. For this technique, by dissolving metal organic precursors into an appropriate solvent, few advantages can be achieved over direct vaporization of the solid phase precursors. For example, low vaporization temperature, accurate control of liquid flow rate, and minimization of precursor oligomerization effect, etc.. In our work, $\text{Ba}(\text{hfa})_2 \cdot \text{tetraglyme}$ $\{\text{Ba}(\text{C}_5\text{HF}_6\text{O}_2) \cdot (\text{C}_{10}\text{H}_{22}\text{O}_5)\}$ and $\text{Ti}(\text{thd})_2(\text{OPr}^i)_2$ $\{\text{Ti}(\text{C}_{11}\text{H}_{19}\text{O}_2)_2(\text{C}_3\text{H}_7\text{O})_2\}$ are dissolved in toluene as the precursor source. The

vaporization and CVD processing conditions are both studied to examine their effects on the as grown thin film quality. Chemical composition, surface and bulk morphology and crystallographic information of the as grown thin films are characterized to monitor the thin film quality. Preliminary results of epitaxial growth of barium titanate thin film on MgO (100) substrate have been achieved and are reported in this chapter.

5.2 Experimental Details

In this work, the same DLI-CVD system as used for the deposition of nickel ferrite is used for the deposition of barium titanate, as shown in Fig.38. Ba(hfa)₂•tetraglyme (m.p. 153°C) and Ti(thd)₂(OPrⁱ)₂ (m.p. ~180°C) are used as metal organic precursors. The Ba precursor is synthesized from Ba(OH)₂•8H₂O following the method reported by Malandrino, et. al., [172] and the Ti precursor is bought from Sigma-Aldrich and used without any further purification. Both precursors are dissolved in Toluene (C₆H₅CH₃, b.p. 110.6°C) in a molar ratio of 1:1. Atomically polished MgO (100) single crystal (a=4.21Å, 5mm×5mm×0.5mm) from CrysTec GmbH is used as the substrate and ultrasonically cleaned sequentially by acetone and isopropanol before loaded into the CVD reactor. Processing conditions for a typical reaction are substrate temperature 750 °C, precursor concentration 0.1 M, precursor flow rate 6 g/hr, vaporizer temperature 150 °C, reaction pressure 10 torr, carrier gas (Ar) flow rate 250 sccm and oxygen flow rate 300 sccm. It is important that the oxygen flow is bubbled through water in this case to eliminate formation of a BaF₂ phase (F eliminated by forming HF). The connection tubing from the vaporizer to the CVD reaction chamber is wrapped by heating tapes and heated to ~10 °C above the vaporizer temperature to avoid vapor condensation on the tubing walls. The oxygen (research grade) gas is preheated to a temperature close to the vaporizer temperature before it's delivered into the reaction chamber to minimize its effect on the vapor quality (gas phase condensation). The

reaction zone of the tube furnace is heated to the reaction temperature in a heating rate of ~ 15 °C/min and stabilized at the deposition temperature for ~ 30 min before CVD reaction. The vaporizer is preheated to the designated temperature with carrier gas flow and stabilize for ~ 30 min. When the liquid precursor source is introduced into the vaporizer, it is first directed into the exhaust by passing through the by-pass line, as shown in Fig.38. The vaporization process is stabilized for ~ 15 min before the valve to the reaction chamber is opened, from when the CVD reaction is started. A cooling trap with liquid nitrogen is used to trap the organic solvent or reaction by products to minimize contamination of pump oil (rotary vane vacuum pump). The as deposited thin film characterization by various techniques are introduced below.

Chemical composition of the as deposited films are characterized by both XPS and EDX. For the XPS (PHI/APEX) measurement, non-monochromatic Al K_{α} (1486.6 eV) X-ray is used to irradiate the sample surface. Analysis area around 2 mm by 2 mm is selected by setting the appropriate electron entrance and exit slit size of the hemispherical electron spectrometer. For a typical XPS measurement, the X-ray beam power is set to 100W, the electron pass energy is set to 100 eV for a survey measurement and 25 eV for a high resolution measurement, and the electron take off angle is set to 45° . The EDX detector is installed in a SEM system (JEOL/7000). A typical EDX measurement has electron beam energy of 20 KV, spot size of 8 and working distance of 10 mm. Measurements from few areas are averaged to get the final composition results. XRD (Philips X'pert Pro) is used to investigate crystallographic properties of the as-deposited films. Cu K_{α} (1.5418 Å) radiation is used as the X-ray source. All the samples are characterized under similar experimental conditions (with a nickel filter and 0.5° divergence slit size). For the rocking curve analysis, 2θ was fixed at the NiFe_2O_4 (200) diffraction angle of barium titanate while scanning ω . For the SEM characterization, electron beam conditions are

the same as those mentioned for EDX measurement. All the samples are attached to the sample holder by carbon tape and no metallic coatings on the sample surfaces are deposited. For the AFM (Digital instruments/ Nanoscope IV) characterization, ultra sharp non-contact silicon cantilevers (MikroMasch, NSC15/AIBS) with a typical probe tip radius of ~10nm and resonant frequency of ~325 kHz are used in tapping mode.

5.3 Results and Discussion

The vaporization conditions of our DLI vaporizer for the specific precursor solution, Ba(hfa)₂•tetraglyme and Ti(thd)₂(OPr)ⁱ₂ in toluene, are optimized by checking the as deposited thin film quality. It has been found that the liquid flow rate, carrier gas flow rate, and vaporizer pressure and temperature work together to give high quality vapor phase. When the precursor source solution is not properly vaporized, large deviation of thin film stoichiometry or surface morphology could be observed. An optimized combination of vaporization conditions has been listed in the experimental details (5.2) and preliminary results of epitaxial barium titanate thin film growth under these vaporization conditions are showed below.

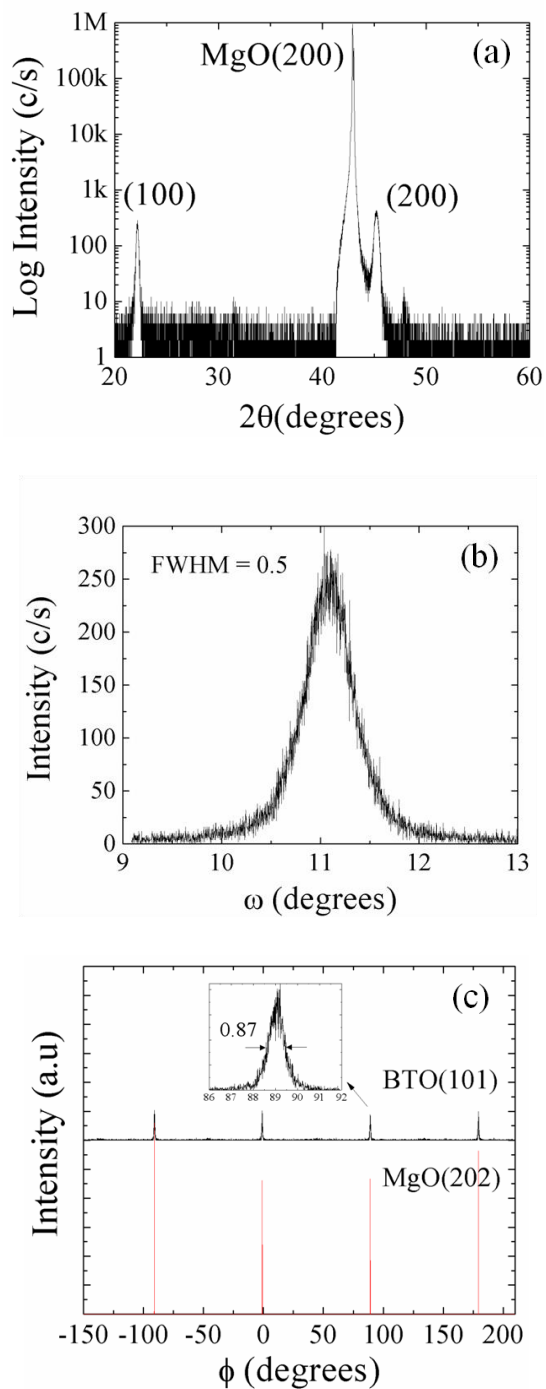


Fig. 58. X-ray diffraction characterization of as deposited nickel ferrite film under 750 °C. (a) θ - 2θ scan of as deposited BTO film on MgO(100) (b) ω -scan of BTO(200) (c) ϕ -scan of {101} and {202} planes of film and substrate respectively.

Fig. 58 shows the XRD characterization results of a barium titanate film deposited on MgO (100) substrate at 750°C. The θ - 2θ X-ray diffraction pattern is shown in Fig. 58(a). As can

be seen, the film grows with single orientation in the normal direction, since X-ray spectrum of BTO film shows only reflections from ($h00$) crystallographic planes the same as those of MgO substrate. According to this X-ray data, the out-of-plane lattice constant of BTO film is found to be 4.007\AA , which is a value between a and c lattice constants ($a = 3.992\text{\AA}$, $c = 4.032\text{\AA}$) of BTO crystal at room temperature.[111] It's impossible to identify the thin film growth in a or c orientation based on this result. Moreover, the peak shift can be also attributed to the interfacial stress. Out-of-plane and in plane texture of this sample are examined by ω and ϕ scan as shown in Fig.58 (b) and (c). The measured FWHM (full-width-at-half-maximum) value of ω -scan of BTO(200) is 0.5° , which is about in the middle of those have been reported ($0.23\sim 0.9$). [117,130,138,139] The ϕ -scan of $\{101\}$ planes of both BTO film and MgO substrate shows the four coincidentally 90° separated peaks. This result illustrated the four fold symmetry of both the BTO and MgO lattice. Meanwhile, the coincidence of peaks positions indicate a cube on cube epitaxial relationship.

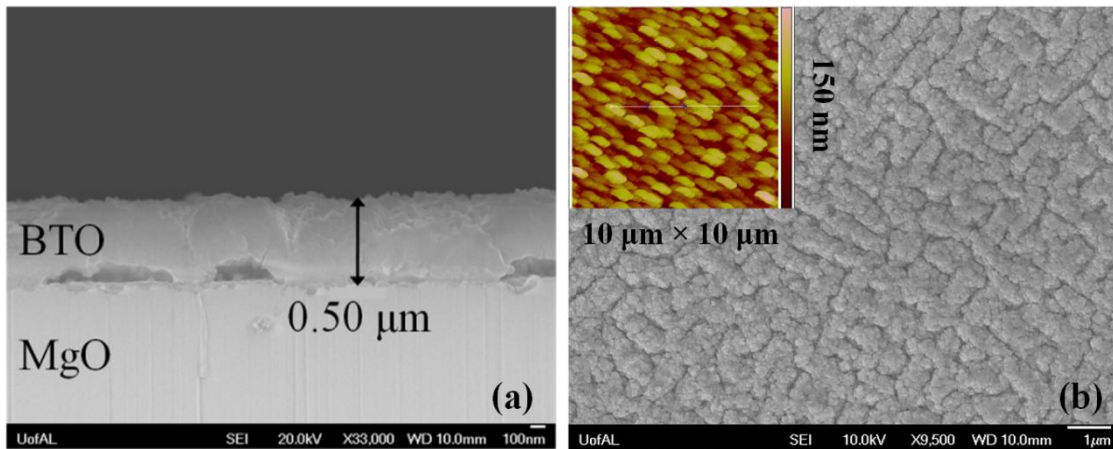


Fig. 59. (a) Cross sectional view of BaTiO₃ on MgO by SEM (b) Surface view of BaTiO₃ film on MgO; inset shows a $10\ \mu\text{m}$ by $10\ \mu\text{m}$ AFM image of the same surface with RMS roughness around $20\ \text{nm}$.

Cross sectional and surface morphology of the as deposited BaTiO₃ film on MgO has been characterized by SEM and AFM. As seen in Fig. 59(a), the cross section of a $\sim 0.5\ \mu\text{m}$ thick (1 hour deposition) BaTiO₃ film on MgO substrate presents certain defects, especially at the

interface. This phenomenon probably results from island mode film growth at a high deposition temperature. Chemical composition of this film is characterized by the Energy Dispersive X-ray spectroscopy (EDX) equipped in the SEM system. The ratio of Ba to Ti is quite close to 1:1 as expected. No F or C element has been detected by this technique. The oxygen concentration is not considered due to external signals from the MgO substrate. The surface morphology of BaTiO₃ films are both studied by SEM and AFM, as shown in Fig. 59(b). The AFM measured grain size is around ~1 μm and RMS roughness is ~20nm.

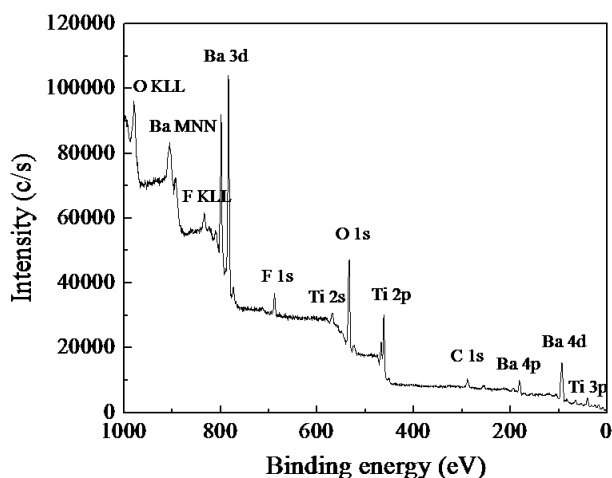


Fig. 60. Fluorine peak is present in the XPS spectrum of as deposited barium titanate thin film surface.

The thin film surface is also characterized by XPS, as shown in Fig.60. Except for the Ba, Ti, and O elements, F (~4 at%) is also detected. The C peak is from adventitious carbon of air contamination (284.8 eV). Different from EDX, which has a detection thickness around 1~2 μm, XPS is a surface sensitive technique (few nm detection thickness) and much more sensitive to small elements like F. High resolution scan of the F peak has showed the peak position is at ~684.7 eV, which indicates the existence of metal fluoride bond. In this case, it's probably Ba-F bond.[129] Besides, this value is a little higher than the reported value of 684.3 eV for F 1s in pure BaF₂, which can be attributed to the different chemical environment.[173] Although the

XRD characterization has showed pure BaTiO₃ phase, F elements can still exist in the film in amorphous phase and affect thin film physical property.

5.4 Conclusion

Epitaxial growth of BaTiO₃ films on MgO (100) substrate has been obtained by DLI-CVD technique. Good single crystal quality has been illustrated by the results of ω and ϕ -scan. Thin film growth rate of ~ 0.5 $\mu\text{m/hr}$ is achieved under our experimental conditions. Surface and cross sectional morphology characterization shows large surface roughness and interface voids, which can be contributed to the island mode thin film growth. Incorporation of small amount of F elements in the thin film has been verified by XPS analysis. Instead of forming crystalline BaF₂ phase, the F elements bonds to the Ba ions in amorphous state.

Although we have obtained epitaxial growth of BTO films, few issues related to thin film quality still need to be improved, such as the film morphology, growth rate, and chemical contamination. Either optimizing CVD processing conditions or selecting more appropriate Ba precursor is believed to be capable of improving these issues in certain degree.

CHAPTER 6. CONCLUSION AND FUTURE WORK

6.1 Conclusion

Chemical vapor deposition (CVD) of thin film materials with excellent electronic or magnetic properties has been investigated in this dissertation. Specific CVD techniques including plasma enhanced atomic layer deposition (PEALD) and direct liquid injection CVD (DLI-CVD) have been employed based on the requirements of practical thin film application. The essential work consists of chemical precursor selection and characterization, CVD processing, and thin film characterization. The results of thin film characterization could provide important information for the optimization of CVD processing conditions and thus in turn to improve the thin film quality. The results of PEALD of hafnium nitride (HfN), DLI-CVD of nickel ferrite (NiFe_2O_4), lithium ferrite (LiFe_5O_8), and barium titanate (BaTiO_3) are summarized below.

6.1.1 PEALD of HfN thin films

Tetrakis (dimethylamido) hafnium (IV) (TDMAH) is used as the metal organic precursor for PEALD of HfN thin film. Its adsorption and reaction on hydrogenated Si(100) surface has been investigated by in-situ ATR-FTIR. It has been found that for temperatures below 100°C , physisorption is the main mode of TDMAH adsorbing onto the crystal surface and no obvious surface Si-H bonds breaking. These physisorbed TDMAH molecules have weak bonding energy to the surface and easy to desorb. At temperatures between 100°C and 150°C , surface adsorbed TDMAH molecules start to decompose and newly emerging IR peaks at 1591 cm^{-1} and 1639 cm^{-1} are assigned to N=C and Hf-H vibrational mode respectively based on a β -hydride elimination mechanism. The decomposition species on the surface has been found hard to desorb at 150°C ,

which can contaminate the thin film growth if the purging/pumping time is not long enough. The surface Si-H bonds subtraction has been found for adsorption above 150°C and it is closely related to the TDMAH decomposition behavior.

Hafnium nitride thin film deposition by PEALD using TDMAH and hydrogen plasma has been investigated. Uniform and moderately conductive HfN_xC_y thin films were deposited on Si(100) and SiO_2 substrates. A thin surface layer (2~3 nm) containing both hafnium nitride and organic complexes of TDMAH decomposition has been found by in vacuo XPS analysis. Depth profile analysis by XPS indicated the existence of hafnium carbide phase in the bulk. Thin film resistivity is greatly affected by the level of hydrogen plasma power, in which higher plasma power results in lower thin film resistivity. In spite of this tunability of resistivity by plasma power, carbon incorporation is still an issue for this PEALD method.

6.1.2 DLI-CVD of nickel ferrite and lithium ferrite films

We have used DLI-CVD technique for the growth of high quality epitaxial NiFe_2O_4 films on MgAl_2O_4 (100), MgO (100), MgO (111) and few piezoelectric substrates. Anhydrous $\text{Ni}(\text{acac})_2$ and $\text{Fe}(\text{acac})_3$ precursor sources are dissolved in DMF and vaporized under optimum conditions to generate stoichiometric concentration of the cations in the gas phase for the CVD reaction. Appropriate oxygen flow with the precursors is important both for improving the film morphology and also to obtain stoichiometric deposition. Under our experimental conditions, film growth rate has been found in the range of 0.6-1.1 $\mu\text{m/hr}$ and can be further increased by increasing the solution concentration or liquid flow rate. However, the vaporizer process condition and the oxygen flow rate also need to be adjusted to maintain the desired film morphology and stoichiometry. Under optimized vaporization conditions, the film morphology is dependent on the deposition temperature because of changes in the surface diffusion behavior. In

the temperature range of 600°C to 700°C, relatively thick epitaxial NiFe₂O₄ films, which are extremely smooth and exhibit excellent magnetic properties, have been deposited on both MgAl₂O₄ (100) and MgO (100) substrates. However, macroscopic cracks develop on MgO after deposition and cool down, likely because of high residual tensile stress. The increased saturation magnetization with increasing deposition temperature can be attributed to improved crystalline quality, which is verified from X-ray diffraction and polarized Raman measurements. The difference between in plane and out-of-plane FMR line width measured at 9.5 GHz indicates the presence of two magnon scattering effect which is related to crystal defects or chemical inhomogeneities in the films. FMR line width as low as ~160 Oe has been achieved for out-of-plane measurement of nickel ferrite films deposited at 600°C, which is quite close to the value of bulk crystal.

DLI-CVD growth of lithium ferrite is investigated by using Li(acac) and Fe(acac)₃ as the metal organic precursors. Different from the deposition of nickel ferrite, lithium ferrite films grown on MgAl₂O₄(100) are much rougher and do not show any crystalline features for deposition at 500°C and 600°C. Spinel crystalline phases have been found for the deposition at 700°C and 800°C. However, more than one orientation are present for deposition at 800°C. Comparatively, lithium ferrite films deposited on MgO(100) exhibits single crystal quality and much smoother surface for the deposition temperature range of 500°C to 800°C. The smaller lattice mismatch between MgO and Nickel ferrite can be the principal reason. The narrowest in plane FMR line width ~368 Oe has been found for the films deposited at 600°C. With suitable optimization of the vaporization and film deposition conditions, excellent quality ferrite films can be grown at a relatively high rate using DLI-CVD.

6.1.3 DLI-CVD of barium titanate films

Epitaxial growth of BaTiO₃ films on MgO (100) substrate has been obtained by DLI-CVD technique. Good single crystal quality has been illustrated by the results of ω and ϕ -scan. Thin film growth rate of ~ 0.5 $\mu\text{m/hr}$ is achieved under our experimental conditions. Surface and cross sectional morphology characterization shows large surface roughness and interface voids, which can be contributed to the island mode thin film growth. Incorporation of small amount of F elements in the thin film has been verified by XPS analysis. Instead of forming crystalline BaF₂ phase, the F elements bonds to the Ba ions in amorphous state.

6.2 Future work

PEALD of HfN by using TDMAH and hydrogen plasma has been limited by thin film contamination from incorporation of C. In spite of the increased conductivity of thin films deposited at high plasma powers, the C concentration is not affected much by the plasma power. This is directly related to the chemical reaction mechanisms between TDMAH and hydrogen plasma. To improve the as deposited thin film quality, substrates with smaller lattice mismatch can be selected, such as MgO(100) (7%). To improve the thin film purity, more appropriate reducing agent than hydrogen plasma should be selected. Dimethyl hydrazine (H₂NN(CH₃)₂), which has been successfully used in thermal CVD of HfN thin films, might be a good candidate for this PEALD experiment to replace hydrogen.[70] Potential advantages include: low plasma power is needed to break the weak N=N bond and the -NH₂ group is more readily to react with the central Hf atom and work as an external N source.[174]

Single crystalline spinel ferrite films, including nickel ferrite and lithium ferrite, have been successfully deposited on certain small lattice match substrates by DLI-CVD method. For nickel ferrite deposition, more work can be focused on the deposition on piezoelectric substrates,

such as PMN-PT and PZN-PT. CVD processing conditions can be tuned to optimize the physical properties of as deposited films and thus provide high quality films for the fundamental research in ferrite-ferroelectric layered heterostructures. A MgO buffer layer can be grown on these piezoelectric substrates to minimize the lattice mismatch and improve thin film morphology. For lithium ferrite thin film growth, substrate with spinel structure and smaller lattice mismatch, such as MgGa_2O_4 ($a=8.28 \text{ \AA}$, 0.6%)[175] and CoGa_2O_4 ($a=8.32 \text{ \AA}$, 0.1%)[176] can be tried for thin film growth. The goal is to achieve both high saturation magnetization and narrow FMR line width.

For the deposition of barium titanate by DLI-CVD technique, incorporation of F in the thin film from the fluorinated Ba precursor has been found. One way to improve is to use stronger oxidizing agent such as ozone (O_3) or hydrogen peroxide (H_2O_2). The other way is to employ new Ba precursors without F elements in the molecule. For example, $\text{Ba}(\text{thd})_2$ {bis(2,2,6,6-tetramethyl-3,5-heptanedionato) barium (II)} or its polyether adduct can be tried. However, due to its low volatility, the vaporizer conditions have to be tuned accordingly.

REFERENCES

- [1]. M. Leong, B. Doris, J. Kedzierski, K. Rim, M. Yang, *Science* **2004**, *306*, 2057.
- [2]. M. N. Baibich, J. M. Broto, A. Fert, F. Nguyen Van Dau, F. Petroff, P. Eitenne, G. Creuzet, A. Friederich, J. Chazelas, *Phys. Rev. Lett.* **1988**, *61*, 2472.
- [3]. J. S. Moodera, G. X. Miao, T. S. Santos, *Physics Today* **2010**, *63*, 46.
- [4]. W. Eerenstein, N. D. Mathur, J. F. Scott, *Nature* **2006**, *442*, 759.
- [5]. F. Zaera, *J. Mater. Chem.* **2008**, *18*, 3521.
- [6]. D. Beaulieu, Y. Ding, Z. L. Wang, W. J. Lackey, *J. Vac. Sci. Technol. B* **2005**, *23*, 2151.
- [7]. K. F. Jensen, *Annu. Rev. Fluid Mech.* **1991**, *23*, 197.
- [8]. S. M. George, *Chem. Rev.* **2010**, *110*, 111.
- [9]. Z. Li, R. G. Gordon, V. Pallem, H. Li, D. V. Shenai, *Chem. Mater.* **2010**, *22*, 3060.
- [10]. M.-K. Song, S.-W. Kang, S.-W. Rhee, *Thin Solid Films* **2004**, *450*, 272.
- [11]. *Thin Film Deposition: Principles and Practice* (D. L. Smith), McGraw-Hill, Inc., New York **1995**.
- [12]. *Chemical Vapor Deposition: Principles and Applications* (M.-L. Hitchman, K.-F. Jensen), Academic Press, London **1993**.
- [13]. M. Leskelä, M. Ritala, *Thin Solid Films* **2002**, *409*, 138.
- [14]. K. R. Bray, G. N. Parsons, *Phys. Rev. B* **2001**, *65*, 035311.
- [15]. B. Daudin, F. Widmann, G. Feuillet, Y. Samson, M. Arlery, J. L. Rouvière, *Phys. Rev. B* **1997**, *56*, R7069.
- [16]. M. T. Currie, S. B. Samavedam, T. A. Langdo, C. W. Leitz, E. A. Fitzgerald, *Appl. Phys. Lett.* **1998**, *72*, 1718.
- [17]. R. N. Jacobs, J. Markunas, J. Pellegrino, L. A. Almeida, M. Groenert, M. Jaime-Vasquez, N. Mahadik, C. Andrews, S. B. Qadri, *J. Cryst. Growth* **2008**, *310*, 2960.

- [18]. L. S.-J. Peng, X. X. Xi, B. H. Moeckly, S. P. Alpay, *Appl. Phys. Lett.* **2003**, 83, 4592.
- [19]. *Introduction to Infrared and Raman Spectroscopy* (N. B. Colthup, L. H. Daly, S. E. Wiberley), Academic Press, New York **1990**.
- [20]. *Infrared Characterization for Microelectronics* (W. S. Lau), World Scientific, New Jersey **1999**.
- [21]. *Internal Reflection Spectroscopy* (N. J. Harrick), John Wiley & Sons, New York **1967**.
- [22]. P. J. Cumpson, *J. Electron Spectrosc. Relat. Phenom.* **1995**, 73, 25.
- [23]. *Handbook of X-ray Photoelectron Spectroscopy* (J. F. Moulder, W. F. Stickle, P. E. Sobol, K. D. Bomben), Physical Electronics **1995**.
- [24]. *Thin Film Analysis by X-ray Scattering* (Mario Berkholtz), WILEY-VCH Verlag GmbH & Co. KGaA, Weinheim **2006**.
- [25]. M. U. Cohen, *Rev. Sci. Instrum.* **1935**, 6, 68.
- [26]. S. Okamoto, O. Kitakami, Y. Shimada, *J. Magn. Magn. Mater.* **2000**, 208, 102.
- [27]. G. Binnig, C. F. Quate, C. Gerber, *Phys. Rev. Lett.* **1986**, 56, 930.
- [28]. *Spin Waves: Theory and Applications* (D. D. Stancil, A. Prabhakar), Springer, New York **2009**.
- [29]. M. P.-Horvath, *J. Magn. Magn. Mater.* **2000**, 215-216, 171.
- [30]. *Ferromagnetic-Relaxation Theory* (Marshall Sparks), McGraw-Hill, New York **1964**.
- [31]. B. K. Kuanr, R. E. Camley, Z. Celinski, *J. Appl. Phys.* **2004**, 95, 6610.
- [32]. S. J. Yuan, L. Wang, R. Shan, S. M. Zhou, *Appl. Phys. A* **2004**, 79, 701.
- [33]. *CMOS: Circuit Design, Layout, and Simulation* (R. J. Baker), Wiley & Sons Inc., Hoboken, New Jersey **2010**.
- [34]. J. Aarik, A. Aidla, H. Mändar, T. Uustare, K. Kukli, M. Schuisky, *Appl. Surf. Sci.* **2001**, 173, 15.
- [35]. H. Kato, T. Nango, T. Miyagawa, T. Katagiri, K. S. Seol, Y. Ohki, *J. Appl. Phys.* **2002**, 92, 1106.
- [36]. M.-H. Cho, Y. S. Roh, C. N. Whang, K. Jeong, S. W. Nahm, D. -H. Ko, J. H. Lee, N. I. Lee, K. Fujihara, *Appl. Phys. Lett.* **2002**, 81, 472.

- [37]. F. Fillot, T. Morel, S. Minoret, I. Matko, S. Maîtrejean, B. Guillaumot, B. Chenevier, T. Billon, *Microelectron. Eng.* **2005**, *82*, 248.
- [38]. J. K. Schaeffer, S. B. Samavedam, D. C. Gilmer, V. Dhandapani, P. J. Tobin, J. Mogab, B. - Y. Nguyen, B. E. White, Jr., S. Dakshina-Murthy, R. S. Rai, Z. -X. Jiang, R. Martin, M. V. Raymond, M. Zavala, L. B. La, J. A. Smith, R. Garcia, D. Roan, M. Kottke, R. B. Gregory, *J. Vac. Sci. Technol. B* **2003**, *21*, 11.
- [39]. Y. T. Hou, F. Y. Yen, P. F. Hsu, V. S. Chang, P. S. Lim, C. L. Hung, L. G. Yao, J. C. Jiang, H. J. Lin, Y. Jin, S. M. Jang, H. J. Tao, S. C. Chen, M. S. Liang, *Electron Device Meeting, IEDM Technical Digest. IEEE international* **2005**, 5-5, 31.
- [40]. Q. X. Jia, J. R. Groves, P. Arendt, Y. Fan, A. T. Findikoglu, S. R. Foltyn, H. Jiang, F. A. Miranda, *Appl. Phys. Lett.* **1999**, *74*, 1564.
- [41]. W. J. Kim, W. Chang, S. B. Qadri, H. D. Wu, J. M. Pond, S. W. Kirchoefer, H. S. Newman, D. B. Chrisey, J. S. Horwitz, *Appl. Phys. A* **2000**, *71*, 7.
- [42]. V. E. Demidov, B. A. Kalinikos, P. Edenhofer, *J. Appl. Phys.* **2002**, *91*, 10007.
- [43]. A. A. Semenov, S. F. Karmanenko, V. E. Demidov, B. A. Kalinikos, *Appl. Phys. Lett.* **2006**, *88*, 033503.
- [44]. A. A. Semenov, S. F. Karmanenko, B. A. Kalinikos, A. N. Slavin, G. Srinivasan, J. V. Mantese, *Integr. Ferroelectr.* **2005**, *75*, 199.
- [45]. A. S. Tatarenko, A. B. Ustinov, G. Srinivasan, V. M. Petrov, M. I. Bichurin, *J. Appl. Phys.* **2010**, *108*, 063923.
- [46]. Y. -Y. Song, J. Das, P. Krivosik, N. Mo, C. E. Patton, *Appl. Phys. Lett.* **2009**, *94*, 182505.
- [47]. S. Shinkai, K. Sasaki, *Jpn. J. Appl. Phys.* **1999**, *38*, 2097.
- [48]. Y. Gotoh, M. Liao, H. Tsuji, J. Ishikawa, *Jpn. J. Appl. Phys.* **2003**, *42*, L778.
- [49]. R. Fujii, Y. Gotoh, M. Y. Liao, H. Tsuji, J. Ishikawa, *Vacuum* 2006, *80*, 832.
- [50]. M. H. Staia, D. G. Bhat, E. S. Puchi-Cabrera, J. Bost, *Wear* **2006** *261*, 540.
- [51]. J. J. Oakes, *Thin Solid Films* 107 (1983) 159.
- [52]. H. Y. Yu, J. F. Kang, C. Ren, J. D. Chen, Y. T. Hou, C. Shen, M. F. Li, D. S. H. Chan, K. L. Bera, C. H. Tung, D.-L. Kwong, *IEEE Elec. Dev. Lett.* **2004**, *25*, 70.
- [53]. R. Nowak, C.L. Li, *Thin Solid Films* **1997**, *305*, 297.

- [54]. B. O. Johansson, J. –E. Sundgren, U. Helmersson, M.K. Hibbs, *Appl. Phys. Lett.* **1984**, *44*, 670.
- [55]. P. R. Aron, A. Grill, *Thin Solid Films* **1982**, *96*, 87.
- [56]. M. Y. Liao, Y. Gotoh, H. Tsuji, J. Ishikawa, *J. Vac. Sci. Technol. A* **2004**, *22*, 214.
- [57]. L. Yuan, G. Fang, C. Li, M. Wang, N. Liu, L. Ai, Y. Cheng, H. Gao, X. Zhao, *Appl. Surf. Sci.* **2007**, *253*, 8538.
- [58]. Y. Gotoh, M.Y. Liao, H. Tsuji, J. Ishikawa, *Jpn. J. Appl. Phys.* **2003**, *42*, L778.
- [59]. R. A. Araujo, X. Zhang, H. Wang, *J. Electron. Mater.* **2008**, *37*, 1828.
- [60]. A. Arranz, *Surf. Sci.* **2004**, *563*, 1.
- [61]. K. Volz, M. Kiuchi, W. Ensinger, *Surf. Coat. Technol.* **1999**, *120-121*, 353.
- [62]. R. Fix, R.G. Gordon, D.M. Hoffman, *Chem. Mater.* **1991**, *3*, 1138.
- [63]. D. M. Hausmann, E. Kim, J. Becker, R. G. Gordon, *Chem. Mater.* **2002**, *14*, 4350.
- [64]. H. Itoh, K. Kato, K. Sugiyama, *J. Mater. Sci.* **1986**, *21*, 751.
- [65]. D. M. Hoffman, *Polyhedron* **1994**, *13*, 1169.
- [66]. J. H. Jang, T. J. Park, J. H. Kim, K. D. Na, W. Y. Park, M. Kim, C. S. Hwang, *J. Electrochem. Soc.* **2009**, *156*, H76.
- [67]. J. S. Becker, E. Kim, R. G. Gordon, *Chem. Mater.* **2004**, *16*, 3497.
- [68]. W. Wang, T. Nabatame, Y. Shimogaki, *Microelectron. Eng.* **2008**, *85*, 320.
- [69]. W. Wang, T. Nabatame, Y. Shimogaki, *Jpn. J. Appl. Phys.* **2004**, *43*, L1445.
- [70]. Y. Kim, A. Baunemann, H. Parala, A. Devi, R.A. Fischer, *Chem. Vap. Deposition* **2005**, *11*, 294.
- [71]. E. J. Kim, D. H. Kim, *Electrochem. Solid State Lett.* **2006**, *9*, C123.
- [72]. S. Consiglio, W. Zeng, N. Berliner, E.T. Eisenbraun, *J. Electrochem. Soc.* **2008**, *155*, H196.
- [73]. V. G. Harris, A. Geiler, Y. Chen, S. D. Yoon, M. Wu, A. Yang, Z. Chen, P. He, P. V. Parimi, X. Zuo, C. E. Patton, M. Abe, O. Acher, C. Vittoria, *J. Magn. Magn. Mater.* **2009**, *321*, 2035.
- [74]. C. N. Chinnasamy, A. Narayanasamy, N. Ponpandian, K. Chattopadhyay, K. Shinoda, B.

- Jeyadevan, K. Tohji, K. Nakatsuka, I. Nakatani, *Phys. Rev. B* **2001**, 63, 184108.
- [75]. E. Rezlesku, L. Sachelarie, P. D. Popa, N. Rezlesku, *IEEE Trans. Magn.* **2000**, 36, 3962.
- [76]. W. G. Nilsen, R. L. Comstock, J. P. Remeika, *J. Appl. Phys.* **1966**, 37, 1224.
- [77]. M. I. Bichurin, V. M. Petrov, G. Srinivasan, *Phys. Rev. B.* **2003**, 68, 054402.
- [78]. M. Pardavi-Horvath, *J. Magn. Magn. Mater.* **2000**, 215-216, 171.
- [79]. P. Gibart, M. Robbins, A. B. Kane, *J. Cryst. Growth* **1974**, 24, 166.
- [80]. J. ŠIMŠOVÁ, *Czech. J. Phys. B.* **1970**, 20, 727.
- [81]. J. E. Mee, G. R. Pulliam, J. L. Archer, P. J. Besser, *IEEE Trans. Magn.* **1969**, 5, 717.
- [82]. A. G. Fitzgerald, R. Engin, *Thin Solid Films* **1974**, 20, 317.
- [83]. P. A. Lane, P. J. Wright, M. J. Crosbie, A. D. Pitt, C. L. Reeves, B. Cockayne, A. C. Jones, T. J. Leedham, *J. Cryst. Growth* **1998**, 192, 423.
- [84]. A. G. Fitzgerald, *J. Mat. Sci.* **1987**, 22, 1887.
- [85]. J. F. Roeder, S. M. Bilodeau, R. J. Carl, T. H. Baum, P. C. Vanbuskirk, R. R. Woolcott, A. I. Kingon, *Mat. Res. Soc. Symp. Proc.* **1997**, 474, 21.
- [86]. E. J. Donahue, D. M. Schleich, *J. Appl. Phys.* **1992**, 71, 6013.
- [87]. S. Pignard, H. Vincent, J. P. Sénateur, *Thin Solid Films* **1999**, 350, 119.
- [88]. J. Lee, B. Lee, S. Joo, *IEEE Trans. Magn.* **1999**, 35, 3415.
- [89]. P. Samarasekara, F. J. Cadieu, *Chin. J. Phys.* **2001**, 39, 635.
- [90]. E. Suzuki, Y. Hoshi, M. Naoe, *J. Appl. Phys.* **1998**, 83, 6250.
- [91]. S. Capraro, J. P. Chatelon, H. Joisten, M. Le Berre, B. Bayard, D. Barbier, J. J. Rousseau, *J. Appl. Phys.* **2003**, 93, 9898.
- [92]. J. M. Robertson, M. Jansen, B. Hoekstra, P. F. Bongers, *J. Cryst. Growth* **1977**, 41, 29.
- [93]. H. L. Glass, J. H. W. Liaw, *Mat. Res. Bul.* **1978**, 13, 353.
- [94]. S. D. Yoon, C. Vittoria, *J. Appl. Phys.* **2003**, 93, 8597.
- [95]. S. D. Yoon, C. Vittoria, *J. Magn. Magn. Mater.* **2004**, 272-276, e1833.

- [96]. J. D. Adam, S. V. Krishnaswamy, S. H. Talisa, K. C. Yoo, *J. Magn. Magn. Mater.* **1990**, 83, 419.
- [97]. J. L. Deschanvres, M. Langlet, J. C. Joubert, *J. Magn. Magn. Mater.* **1990**, 83, 437.
- [98]. J. M. Phillips, R. B. Vandover, E. M. Gyorgy, J. H. Marshall, *Mat. Res. Soc. Symp. Proc.* **1994**, 317, 589.
- [99]. P. Samarasekara, R. Rani, F. J. Cadieu, S. A. Shaheen, *J. Appl. Phys.* **1996**, 79, 5425.
- [100]. M. T. Johnson, P. G. Kotula, C. B. Carter, *J. Cryst. Growth* **1999**, 206, 299.
- [101]. C. N. Chinnasamy, S. D. Yoon, A. Yang, A. Baraskar, C. Vitorria, V. G. Harris, *J. Appl. Phys.* **2007**, 101, 09M517.
- [102]. J. X. Ma, D. Mazumdar, G. Kim, H. Sato, N. Z. Bao, A. Gupta, *J. Appl. Phys.* **2010**, 108, 063917.
- [103]. Y. -Y. Song, M. S. Grinolds, P. Krivosik, C. E. Patton, *J. Appl. Phys.* **2005**, 97, 103516.
- [104]. Z. Chen, A. Yang, A. Gieler, V. G. Harris, C. Vittoria, P. R. Ohodnicki, K. Y. Goh, M. E. McHenry, Z. Cai, T. L. Goodrich, K. S. Ziemer, *Appl. Phys. Lett.* **2007**, 91, 182505.
- [105]. V. G. Harris, A. Geiler, Y. Chen, S. D. Yoon, M. Wu, A. Yang, Z. Chen, P. He, P. V. Parimi, X. Zuo, C. E. Patton, M. Abe, O. Acher, C. Vittoria, *J. Magn. Magn. Mater.* **2009**, 321, 2035.
- [106]. M. P.-Horvath, *J. Magn. Magn. Mater.* **2000**, 215-216, 171.
- [107]. J. M. Robertson, J. P. M. Damen, H. A. Algra, *IEEE Trans. Magn.* **1979**, 15, 1870.
- [108]. H. Itoh, T. Takeda, S. Naka, *J. Mater. Sci.* **1986**, 21, 3677.
- [109]. L. B.-Dor, R. Druilhe, P. Gibart, *J. Cryst. Growth*, **1974**, 24/25, 172.
- [110]. M. K. Song, S. W. Kang, S. W. Rhee, *Thin Solid Films* **2004**, 450, 272.
- [111]. J. Zhao, V. Fuflyigin, P. E. Norris, L. Bouthilette, C. Woods, *J. Mater. Chem.* **1997**, 7, 933.
- [112]. Z. Li, R. G. Gordon, V. Pallem, H. Li, D. V. Shenai, *Chem. Mater.* **2010**, 22, 3060.
- [113]. A. F. Devonshire, *Phil. Mag.* **1949**, 40, 1040.
- [114]. J. F. Roeder, S. M. Bilodeau, R. J. Carl, T. H. Baum, P. C. Vanbuskirk, R. R. Woolcott, A. I. Kingon, *Mat. Res. Soc. Symp. Proc.* **1997**, 474, 21.
- [115]. L. A. Wills, B. W. Wessels, D. S. Richeson, T. J. Marks, *Appl. Phys. Lett.* **1992**, 60, 41.

- [116]. M. Matsuoka, K. Hoshino, K. Ono, *J. Appl. Phys.* **1994**, 76, 1768.
- [117]. S. Kim, S. Hishita, Y. M. Kang, S. Baik, *J. Appl. Phys.* **1995**, 78, 5604.
- [118]. S. Kim, S. Hishita, *J. Mater. Res.* **1997**, 12, 1152.
- [119]. T. Pencheva, M. Nenkov, *Vacuum*, **1997**, 48, 43.
- [120]. K. Iijima, T. Terashima, K. Yamamoto, K. Hirata, Y. Bando, *Appl. Phys. Lett.* **1990**, 56, 527.
- [121]. R. E. Avila, J. V. Caballero, V. M. Fuenzalida, I. Eisele, *Thin Solid Films*, **1999**, 348, 44.
- [122]. M. G. Norton, C. Scarfone, J. Li, C. B. Carter, J. W. Mayer, *J. Mater. Res.* **1991**, 6, 2022.
- [123]. M. B. Lee, M. Kawasaki, M. Yoshimoto, B. K. Moon, H. Ishiwara, H. Koinuma, *Jpn. J. Appl. Phys.* **1995**, 34, 808.
- [124]. G. M. Davis, M. C. Gower, *Appl. Phys. Lett.* **1989**, 55, 112.
- [125]. D. Y. Kim, S. G. Lee, Y. K. Park, S. J. Park, *Mater. Lett.* **1999**, 40, 146.
- [126]. T. L. Goodrich, Z. Cai, M. D. Losego, J. -P. Maria, L. F. Kourkoutis, D. A. Muller, K. S. Ziemer, *J. Vac. Sci. Technol. B* **2008**, 26, 1110.
- [127]. H. Kumazawa, K. Masuda, *Thin Solid Films* **1999**, 353, 144.
- [128]. B. S. Kwak, K. Zhang, E. P. Boyd, A. Erbil, B. J. Wilkens, *J. Appl. Phys.* **1991**, 69, 767.
- [129]. E. J. Donahue, D. M. Schleich, *Mat. Res. Bull.* **1991**, 26, 1119.
- [130]. H. Nakazawa, H. Yamane, T. Hirai, *Jpn. J. Appl. Phys.* **1991**, 30, 2200.
- [131]. C. S. Chern, J. Zhao, L. Luo, P. Lu, Y. Q. Li, P. Norris, B. Kear, F. Cosandey, C. J. Maggiore, B. Gallois, B. J. Wilkens, *Appl. Phys. Lett.* **1992**, 60, 1144.
- [132]. P. C. Van Buskirk, R. Gardiner, P. S. Kirilin, S. Nutt, *J. Mater. Res.* **1992**, 7, 542.
- [133]. T. W. Kim, M. Jung, Y. S. Yoon, W. N. Kang, H. S. Shin, S. S. Yom, J. Y. Lee, *Solid State Commun.* **1993**, 86, 565.
- [134]. D. L. Kaiser, M. D. Vaudin, G. Gillen, C. -S. Hwang, L. H. Robins, L. D. Rotter, *J. Cryst. Growth*, **1994**, 137, 136.
- [135]. D. L. Kaiser, M. D. Vaudin, L. D. Rotter, Z. L. Wang, J. P. Cline, C. S. Hwang, R. B. Marinenko, J. G. Gillen, *Appl. Phys. Lett.* **1995**, 66, 2801.

- [136]. J. Zhao, V. Fuflyigin, F. Wang, P. E. Norris, C. Woods, *J. Mater. Chem.* **1997**, 7, 933.
- [137]. J. Zeng, H. Wang, M. Wang, S. Shang, Z. Wang, C. Lin, *Thin Solid Films* **1998**, 322, 104.
- [138]. A. R. Teren, J. A. Belot, T. J. Marks, B. W. Wessels, *Chem. Vap. Deposition* **2000**, 6, 175.
- [139]. A. M. Dhote, A. L. Meier, D. J. Towner, B. W. Wessels, J. Ni, T. J. Marks, *J. Vac. Sci. Technol. B* **2005**, 23, 1674.
- [140]. A. R. Meier, F. Niu, B. W. Wessels, *J. Cryst. Growth* **2006**, 294, 401.
- [141]. J. -H. Lee, S. -W. Rhee, *J. Electrochem. Soc.* **1999**, 146, 3783.
- [142]. M. I. Bichurin, V. M. Petrov, G. Srinivasan, *Phys. Rev. B.* **2003**, 68, 054402.
- [143]. K. Li, S. Li, N. Li, D. A. Dixon, T. M. Klein, *J. Phys. Chem. C* **2010**, 114, 14061.
- [144]. C. L. Platt, N. Li, K. Li, T. M. Klein, *Thin Solid Films* **2010**, 518, 4081.
- [145]. J. P. A. M. Driessen, J. Schoonman, K. F. Jensen, *J. Electrochem. Soc.* **2001**, 148, G178.
- [146]. L. H. Dubois, B. R. Zegarski, G. S. Girolami, *J. Electrochem. Soc.* **1992**, 139, 3603.
- [147]. H. D. Thomas, K. Chen, N. L. Allinger, *J. Am. Chem. Soc.* **1994**, 116, 5887.
- [148]. J. N. Musher, R. G. Gordon, *J. Mater. Res.* **1996**, 11, 989.
- [149]. M. J. Kelly, J. H. Han, C. B. Musgrave, G. N. Parsons, *Chem. Mater.* **2005**, 17, 5305.
- [150]. A. J. Perry, L. Schlapbach, *Solid State Commun.* **1985**, 56, 837.
- [151]. A. J. Perry, L. Schlapbach, W. D. Sproul, *Solid State Commun.* **1987**, 62, 23.
- [152]. G. R. Gruzalski, D. M. Zehner, *Phys. Rev. B* **1990**, 42, 2768.
- [153]. B. H. Lee, L. Kang, R. Nieh, W. -J. Qi, J. C. Lee, *Appl. Phys. Lett.* **2000**, 76, 1926.
- [154]. M. Devillers, O. Dupuis, A. Janosi, J. P. Soumillion, *Appl. Surf. Sci.* **1994**, 81, 83.
- [155]. P. A. Williams, A. C. Jones, J. F. Bickley, A. Steiner, H. O. Davies, T. J. Leedham, S. A. Impey, J. Garcia, S. Allen, A. Rougier, A. Blyr, *J. Mater. Chem.* **2001**, 11, 2329.
- [156]. J. V. Hoene, R. G. Charles, W. M. Hickam, *J. Phys. Chem.* **1958**, 62, 1098.
- [157]. B. Pal, M. Sharon, *Thin Solid Films* **2000**, 379, 83.

- [158]. R. Molina, G. Poncelet, *J. Phys. Chem. B* **1999**, *103*, 11290.
- [159]. I. K. Igumenov, A. E. Turgambaeva, P. P. Semyannikov, *J. Phys. IV* **2001**, *11*, Pr3-505.
- [160]. P. J. Besser, J. E. Mee, P. E. Elkins, D. M. Heinz, *Mat. Res. Bull.* **1971**, *6*, 1111.
- [161]. V. G. Ivanov, M. V. Abrashev, M. N. Iliev, M. I. Aroyo, *Phys. Rev. B* **2010**, *82*, 024104.
- [162]. M. N. Iliev, D. Mazumdar, J. X. Ma, A. Gupta, F. Rigato and J. Fontcuberta, *Phys. Rev. B*, **2011**, *83*, 014108.
- [163]. R. Datta, S. Kanuri, S. V. Karthik, D. Mazumdar, J. X. Ma, A. Gupta, *Appl. Phys. Lett.* **2010**, *97*, 071907.
- [164]. D. Gangaware, R. Woolcott, A. I. Kingon, J. F. Roeder, T. H. Baum, *Mat. Res. Soc. Symp. Proc.* **1999**, *574*, 169.
- [165]. M. Desai, S. Prasad, N. Venkataramani, I. Samajdar, A. K. Nigam, N. Keller, R. Krishnan, E. M. B.-Saitovitch, B. R. Pujada, A. Rossi, *J. Appl. Phys.* **2002**, *91*, 7592.
- [166]. C. Kittel, *Phys. Rev.* **1948**, *73*, 155.
- [167]. J. MACHÁČKOVÁ, *Phys. Stat. Sol.* **1968**, *26*, 435.
- [168]. C. Kittel, *J. Phys. Radium* **1951**, *12*, 291.
- [169]. P. E. Seiden, *Phys. Rev.* **1964**, *133*, A728.
- [170]. L. Torres, M. Zazo, J. Iñiguez, J. M. Munoz, *IEEE Trans. Magn.* **1993**, *29*, 3434.
- [171]. M. J. Hurben, C. E. Patton, *J. Appl. Phys.* **1998**, *83*, 4344.
- [172]. G. Malandrino, F. Castelli, I. L. Fragalà, *Inorg. Chim. Acta* **1994**, *224*, 203.
- [173]. Y. Wu, J. T. Mayer, E. Garfunkel, T. E. Madey, *Langmuir* **1994**, *10*, 1482.
- [174]. Y. Xu, C. B. Musgrave, *Chem. Phys. Lett.* **2005**, *407*, 272.
- [175]. G. Katz, R. Roy, *J. Cryst. Growth* **1970**, *6*, 221.
- [176]. W. E. Kramer, A. M. Stewart, R. H. Hopkins, *J. Cryst. Growth* **1985**, *73*, 329.

APPENDIX A: LabVIEW PROGRAM FOR PEALD AUTOMATIC PROCESS

APPENDIX B: TDMAH MOLECULAR STRUCTUR OPTIMIZATION AND IR
FREQUENCY CALCULATION

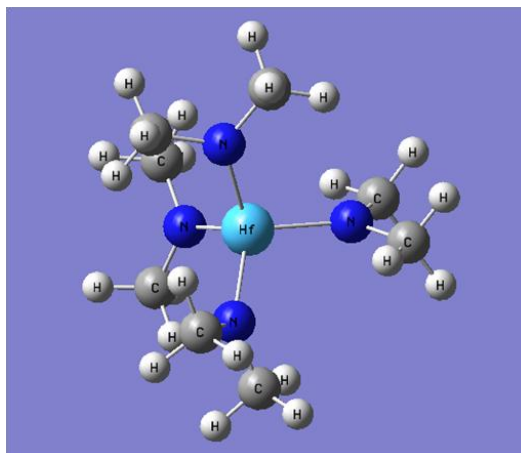


Fig. 62. 3D view of TDMAH molecular structure optimized by DFT method.

The input file (Gaussian03) for TDMAH structure optimization and IR frequency calculation is showed below.

```
%chk=TDMAHRE.chk
%mem=60MW
%nprocshared=4
# opt freq b3lyp/genecp geom=connectivity nosymm
```

TDMAH structure optimization and IR frequency calculation

```
0 1
Hf
N      1      B1
N      1      B2  2      A1
N      1      B3  2      A2  3      D1
N      1      B4  2      A3  3      D2
C      5      B5  1      A4  2      D3
H      6      B6  5      A5  1      D4
H      6      B7  5      A6  1      D5
H      6      B8  5      A7  1      D6
C      5      B9  1      A8  2      D7
H      10     B10 5      A9  1      D8
H      10     B11 5      A10 1      D9
H      10     B12 5      A11 1      D10
C      2      B13 1      A12 3      D11
H      14     B14 2      A13 1      D12
H      14     B15 2      A14 1      D13
H      14     B16 2      A15 1      D14
C      2      B17 1      A16 3      D15
H      18     B18 2      A17 1      D16
```

H	18	B19	2	A18	1	D17
H	18	B20	2	A19	1	D18
C	4	B21	1	A20	2	D19
H	22	B22	4	A21	1	D20
H	22	B23	4	A22	1	D21
H	22	B24	4	A23	1	D22
C	4	B25	1	A24	2	D23
H	26	B26	4	A25	1	D24
H	26	B27	4	A26	1	D25
H	26	B28	4	A27	1	D26
C	3	B29	1	A28	2	D27
H	30	B30	3	A29	1	D28
H	30	B31	3	A30	1	D29
H	30	B32	3	A31	1	D30
C	3	B33	1	A32	2	D31
H	34	B34	3	A33	1	D32
H	34	B35	3	A34	1	D33
H	34	B36	3	A35	1	D34

B1	2.14000000	A11	109.47123134
B2	2.14000000	A12	109.47120255
B3	2.14000000	A13	109.47120255
B4	2.14000000	A14	109.47120255
B5	1.47000000	A15	109.47123134
B6	1.07000000	A16	109.47120255
B7	1.07000000	A17	109.47120255
B8	1.07000000	A18	109.47120255
B9	1.47000000	A19	109.47123134
B10	1.07000000	A20	109.47120255
B11	1.07000000	A21	109.47120255
B12	1.07000000	A22	109.47120255
B13	1.47000000	A23	109.47123134
B14	1.07000000	A24	109.47120255
B15	1.07000000	A25	109.47120255
B16	1.07000000	A26	109.47120255
B17	1.47000000	A27	109.47123134
B18	1.07000000	A28	109.47120255
B19	1.07000000	A29	109.47120255
B20	1.07000000	A30	109.47120255
B21	1.47000000	A31	109.47123134
B22	1.07000000	A32	109.47120255
B23	1.07000000	A33	109.47120255
B24	1.07000000	A34	109.47120255
B25	1.47000000	A35	109.47123134
B26	1.07000000	D1	119.99998297
B27	1.07000000	D2	-120.00003407

B28	1.07000000	D3	-59.67581539
B29	1.47000000	D4	179.42741141
B30	1.07000000	D5	-60.57257380
B31	1.07000000	D6	59.42741881
B32	1.07000000	D7	60.32419940
B33	1.47000000	D8	59.78081838
B34	1.07000000	D9	179.78083317
B35	1.07000000	D10	-60.21917422
B36	1.07000000	D11	59.88892443
A1	109.47121829	D12	69.90242347
A2	109.47123134	D13	-170.09756173
A3	109.47121829	D14	-50.09756913
A4	109.47120255	D15	-60.11109036
A5	109.47120255	D16	-179.68318452
A6	109.47120255	D17	-59.68316972
A7	109.47123134	D18	60.31682288
A8	109.47120255	D19	173.51146610
A9	109.47120255	D20	177.63965870
A10	109.47120255	D21	-62.36032651
D22	57.63966610		
D23	53.51145130		
D24	66.14384390		
D25	-173.85614130		
D26	-53.85614870		
D27	-119.99798461		
D28	67.09960684		
D29	-172.90037837		
D30	-52.90038577		
D31	120.00200060		
D32	65.84469999		
D33	-174.15528521		
D34	-54.15529261		

Hf 0
LANL2DZ

H C N 0
6-31+G(d,p)

Hf 0
LANL2DZ